UNIVERSITAT POLITÈCNICA DE CATALUNYA BARCELONATECH

Sentinel-1 data exploitation for terrain deformation monitoring

Vrinda Krishnakumar

Sentinel-1 data exploitation for terrain deformation monitoring

Vrinda Krishnakumar

Advisor:
Dr. Oriol Monserrat
Divisió de Geomàtica
Centre Tecnològic de Telecomunicacions de Catalunya (CTTC)

Tutor:
Prof. Josep Gili Ripoll
Dep. d'Enginyeria del Terreny
Universitat Politècnica de Catalunya

PhD. Dissertation
Title: Sentinel-1 data exploitation for terrain deformation monitoring
Author: Vrinda Krishnakumar
Advisor: Dr. Oriol Monserrat
Tutor: Prof. Josep Gili Ripoll
Centre: Centre Tecnològic de Telecomunicacions de Catalunya (CTTC)
PhD program: Aerospace Science and Technology - UPC
Castelldefels, 15th November 2021

To Oriol Monserrat and Marina Roca

ABSTRACT

Persistent Scatterer Interferometry (PSI) is a group of advanced differential interferometric Synthetic Aperture Radar (SAR) techniques used to measure and monitor terrain deformation. Sentinel-1 has improved the data acquisition throughout and, compared to previous sensors has considerably increased the Differential Interferometric SAR (DInSAR) and PSI deformation monitoring potential. The effect of the refractive atmosphere on the interferometric phase and the phase unwrapping ambiguity are two of the most critical issues of InSAR. The low density of Persistent Scatterer (PS) in non-urban areas, another critical issue, has inspired the development of alternative approaches and refinement of the PS chains in DInSAR. Along with the efforts to develop methods to mitigate the three problems mentioned above, the work presented in this thesis also deals with the presence of a new signal in multilooked interferograms which cannot be explained by noise, atmospheric or earth surface topography changes. This first part of the thesis describes a method for atmospheric phase screen estimation using rain station weather data and later three different data driven procedures to obtain terrain deformation maps. These approaches aim to exploit the highly coherent interferograms from Sentinel-1 and their short revisit time. The first method called the spectrum splitting makes use of the power spectrum of the interferograms to split the signals into high and low frequency and following a mutually exclusive consecutive processing chain for the two sets. This approach has resulted in a greater density of PSs with decreased phase unwrapping errors. The second approach, called Direct Integration (DI), aims at providing a very fast and straightforward method to screen wide areas and easily detect active areas. This approach fully exploits the coherent interferograms from the consecutive SAR images provided by Sentinel-1 resulting in a very high sampling density. However, it lacks robustness and its usability lays on the operator experience. The third method, called PSIG (Persistent Scatterer Interferometry Geomatics) short temporal baseline, provides a constrained application of the PSIG chain of our research centre CTTC. It uses short temporal baseline interferograms and do not assume any deformation model for point selection. It is also a straightforward approach and a perfect complement to the direct integration approach. It improves the performances of the standard PSIG approach by increasing the PS density and providing robust measurements. The effectiveness of the approaches are illustrated through analysis performed on different test sites.

Keywords: Sentinel-1; interferometry; deformation; DInSAR

RESUMEN

La técnica Persistent Scatterer Interferometry (PSI) es un grupo de técnicas avanzadas de radar de apertura sintética interferométrica diferencial (SAR) que se utiliza para medir y monitorear losmovimientos del terreno. Sentinel-1 ha mejorado sensiblemente la adquisición de datos y, en comparación con los sensores SAR anteriores, ha aumentado considerablemente el potencial uso de la interferometría diferencial SAR y del PSI para medir y monitorizar desplazamientos del terreno. El efecto de la atmósfera sobre la fase interferométrica y la naturaleza ambigua de esta son dos cuestiones críticas de InSAR. Además, la baja densidad de Persistent Scatterer (PSs) en áreas no urbanas, es otro tema crítico que ha inspirado el desarrollo de enfoques alternativos y el refinamiento de las cadenas PS existentes. Junto con los esfuerzos por desarrollar métodos para mitigar los tres problemas antes mencionados, el trabajo presentado en esta tesis también aborda la presencia de una nueva señal en interferogramas multilooked que no puede explicarse por cambios de ruido, atmosféricos o topográficos de la superficie terrestre. Esta tesis describe un método para la estimación de la fase atmosférica utilizando datos meteorológicos adquiridos in-situ y tres aproximaciones diferentes basadas en datos Sentinel-1 para obtener mapas de deformación del terreno. Estos enfoques tienen como objetivo explotar los interferogramas altamente coherentes proporcionados por Sentinel-1 gracias a su corto tiempo de revisita. El primer método llamado división hace uso de filtros en el dominico frecuencial de los interferogramas para dividir las señales en alta y baja frecuencia, y siguiendo una cadena de procesamiento consecutiva independiente para cada clase. Este enfoque ha dado como resultado una mejora substancial de PS minimizando los errores debidos al desenrollado de fase. El segundo enfoque, llamado Integración Directa (DI), tiene como objetivo proporcionar un enfoque muy rápido y sencillo para examinar áreas amplias y detectar fácilmente áreas activas. Este enfoque aprovecha al máximo los interferogramas coherentes de las imágenes consecutivas proporcionadas por Sentinel-1, lo que da como resultado una densidad de muestreo muy alta. Sin embargo, carece de robustez y su usabilidad depende de la experiencia del operador. El tercer método, llamado PSIG (Persistent Scatterer Interferometry Geomatics) de línea de base temporal corta, proporciona una aplicación restringida de la cadena PSIG, el enfoque CTTC para el PSI. Utiliza interferogramas de línea base temporales cortos y no asume ningún modelo de deformación para la selección de puntos. Su uso es complementario al enfoque de integración directa proporcionando robustez en las zonas. Mejora el rendimiento del enfoque estándar de PSIG, aumentando la densidad de PS y proporcionando mediciones robustas. La efectividad de los enfoques se ilustra a través de análisis realizados en diferentes sitios de prueba.

TABLE OF CONTENTS

LIST OF FIGURES

LIST OF TABLES

Chapter 1
Introduction

SAR is an extensive tool used to measure the topography of the surface, its changes over time and other changes in the surface [1]. It is regarded as a very powerful technique in earth observation because of its all-weather and day-and-night imaging capability, wide spatial coverage, fine resolution and competitive accuracy [2]. SAR can measure different aspects of the illuminated surface such as topography [3, 4] changes over time [5] soil moisture [6] and surface displacements associated with, for example, earthquakes [7, 8, 9], tectonic contraction [10], landslides [11], mining activities [12, 13], underground water pumping [14, 15], oil extraction [16], subsidence [17] etc. Interferometry is the technique of comparing the phase of two SAR images to understand the changes happening in the area depicted in the images. Differential SAR interferometry is essentially the comparison of the interferometric phase of two SAR images acquired over the same area on different time. In the last 25 years, the Differential SAR interferometry technique (DInSAR) has been widely used as a tool to map and measure ground displacements. Since the first results in 1989 [18], the technique has experienced a continuous growth. Over these years, the development of processing tools and the increasing availability of data have turned the DInSAR techniques into an operative and reliable tool for mapping and monitoring geohazards. In particular, the Advanced DInSAR techniques (A-DInSAR), are a set of techniques that make use of stacks of SAR images, exploited to obtain very high precision (mm order) displacement measurements while covering extensive areas of terrain [19]. These unique capabilities have motivated the setup of several monitoring programs at regional [20, 21], national [22] and even European level [23] and an intensive research effort to improve their reliability and provide key inputs for geohazard risk managers [24, 25, 26].

The growth of the DInSAR technique is mainly due to two main contributing components. The first one is the important research and development effort made in this period, which has generated a wide number of data processing and analysis tools and methods. They include the classical single-interferogram DInSAR methods, e.g., see [2, 27], the DInSAR stacking techniques [28, 29, 30] and several implementations of the so-called Persistent Scatterer Interferometry (PSI) methods [19, 31, 32, 33].

Persistent or permanent scatterers (PS) are those objects whose backscatter is strong and dominant in the radar image and is constant over time. Persistent Scatterer interferometry (PSI) is a specific branch of advanced differential interferometric Synthetic Aperture Radar (A-DInSAR) techniques used to measure and monitor terrain deformation. The first PSI technique was proposed by Ferretti et al., 2000, followed by the Small Baseline Subset (SBAS) technique [34] which is one of the most extensively used. Crosetto et al., provided an extensive and complete review of persistent scatterer interferometry [19], including the main PSI algorithms, several technical aspects of the PSI techniques, the validation of the PSI results, the main PSI applications, and main open PSI problems. PSI techniques have several advantages among which the important ones are the wide area coverage and high sensitivity to deformations of smaller magnitudes.

The second component is satellite data availability, which has increased in terms of the number of satellites with different spatial and temporal resolutions. Most of the DInSAR and PSI developments have been based on C-band data from the sensors on-board the satellites ERS-1/2, Envisat and Radarsat. The data acquired by these satellites cover long periods of time, a key aspect to guarantee long-term deformation monitoring. DInSAR and PSI have experienced a major step forward since 2007, with the advent of very high-resolution X-band data, e.g., see [1]. This includes the capability to generate a dense sampling of Persistent Scatterers [35], a high sensitivity to small displacements [33, 36, and 37] and a remarkable quality improvement of the time series with respect to the C-band [1]. The latest advancement in image acquisition is the launch of the Sentinel-1 (S-1) A and B satellites, launched in 2014 and 2016 respectively by ESA. With the new C-band sensor on-board S-1 has improved the data acquisition throughout and, compared to previous sensors, increases considerably the DInSAR and PSI deformation monitoring potential [38, 39, 40]. This is confirmed by the high number of papers produced in the first four years of the whole constellation addressing different monitoring applications such as landslides [38, 41], volcanoes [42, 43], subsidence [44, 45] or mining [46, 47]. Moreover, the large proportion of available data has resulted in the development of advanced products aiming at early warning support [26] or risk management [24]. From the processing point of view, a significant improvement is the availability of 6-day C-Band interferograms that provide high coherent signal in places where it was not possible with the previous sensors, e.g., low vegetation fields, dry but non-solid areas, areas with relatively fast displacements, etc. This has improved the A-DInSAR performances in

general, mitigating the effects of the phase unwrapping error in many cases, allowing the improvement of the monitoring capabilities in non-urban areas and promoting a better understanding of the measured phenomena. However, S-1 has also brought in challenging issues such as the management of a huge volume of data [48], the processing of these data and the analysis of the results [49]. These challenging issues have in turn brought in strong efforts in research. A part of the research has been devoted to the development of tools at the processing level addressing two main issues: data ingestion and automation [50, 51]. There has also been significant effort at the post processing level with the development of tools and procedures to provide semi-automatic data analysis and to transform standard A-DInSAR results into more understandable products for end-users [47]. Moreover, the capability of monitoring areas once inaccessible with previous sensors has brought in new signal components. It can be observed that S-1 interferograms also unfold a systematic signal in highly coherent points, especially in short temporal baseline interferograms, which cannot be explained by the topographic or atmospheric phase contributions and can significantly affect the deformation measurements. The understanding of the source of this signal and its modelling is also a current research topic [52]. Finally, although the strong potentials of the high coherent interferograms provided by Sentinel-1 constellation, there has not been a strong development on the automatic exploitation of them.

As the roots of SAR interferometry spread widely all over the scientific world, a deeper understanding of its limitations arose. The effect of the atmosphere on the interferometric phase and phase unwrapping ambiguity are two critical issues of InSAR that affect the deformation measurements. Atmospherically induced distortion has been observed in almost all SAR interferometry applications [54-57] but has typically been treated as noise. Propagation delays are caused due to air refractivity gradients of the troposphere [56, 58]. Also, the atmospheric contribution to phase differences cannot be easily distinguished from surface displacements and thus has an impact on altitude and surface deformation measurements [59]. Great efforts have been made to understand the properties of the atmospheric effects on InSAR and to develop methods to mitigate the same. The DInSAR stacking techniques [27, 60] include different approaches to reduce the atmospheric effects by averaging various interferograms. Many works have been done on the crucial step in interferogram processing which is called phase unwrapping. Each of the two SAR images gives only a measure of the phase of the received electromagnetic radiation

modulo 2π. The phase difference modulo 2π can be calculated from the two images, while it is necessary to determine the whole phase difference of the signals in the two images to determine the 3-D position of the corresponding points in the scene [61]. Therefore, it is important to unwrap the available phase difference, that is, to reconstruct the whole phase difference in the corresponding pixel of the two images from the knowledge of that difference modulo 2π. The total phase difference obtained between two points in an interferogram measures many multiples of 2π [62]. This phase difference needs to be determined by counting the number of phase cycles, also known as fringes, between the points. The phase unwrapping errors, which are typically integer multiples of 2π, can be caused by different factors such as phase noise, high local deformation gradients, strong atmospheric phase component, use of the wrong estimation model for phase unwrapping etc.

Along with an attempt to address the above-mentioned issues, the low density of Persistent Scatterers (PS) in non-urban areas is another issue to be addressed while developing PS processing chains. These three problems have inspired the development of alternative approaches and refinement of the standard PS processing chains. Thus, this thesis is aimed to address the above-mentioned problems in DInSAR and fulfil the following specific objectives.

1) Deformation monitoring using Sentinel-1 data.

   Develop tools and semi-automatic approaches to exploit the wide area covering and the high coherence and temporal sampling (revisit time of 6 days) provided by the Sentinel-1 satellites to allow mid and long-term monitoring of the deformations and understand the role of the new temporal sampling to improve deformation estimations.

2) Quantification of atmospheric phase delay.

   Analysis of the existing models to separate atmospheric phase contribution from the interferometric phase. The feasibility of the DInSAR deformation and atmospheric phase evaluation depends on the topography and the land coverage of the studied area.

3) Improve phase unwrapping.

   By removing the atmospheric phase from the interferometric phase before phase unwrapping can help mitigate the errors due to atmosphere in phase unwrapping and improve the quality of the deformation measurements. A combination of

spatial and temporal based tools was used to reduce the number of phase unwrapping errors.

4) Validation and analysis with different case studies.

This thesis has been carried out at the Remote Sensing Department of the Geomatics Division of the CTTC. The starting point of this work was an already complete Persistent Scatterer Interferometry chain (PSIG) that had been successfully tested with C-band and X-band SAR data [1], to process wide areas while maintaining PS density in urban areas and obtaining a sufficient density in rural areas [2]. My work started with the understanding and analysis of the existing PSIG chain to exploit the latest Sentinel-1 C band SAR data satellites. The wide area coverage of 250 x 250 km in a single image scene, the high coherence from the high temporal sampling of 6 days etc. are some of the highlights of the Sentinel-1 data. Then the work was focused on the analysis on the separation phase contribution of different components from the interferometric phase. The feasibility of the DInSAR deformation and atmospheric phase evaluation depends on the topography and the land coverage of the studied area. The main goal was to propose semi-automatic standard methods to be included in the processing chain modifying the standard PSIG chain with improving the induced phase errors, thus improving accuracy of the deformation measurements. Hence, this work analyses the competency of three such methods that can be incorporated into the standard PSIG chain.

This dissertation is organized in four main chapters, in addition to the introduction (Chapter 1) and the conclusions (Chapter 6). Chapter 2 is devoted to the basic principles of Persistent Scatterer Interferometry and a review of the standard PSIG chain, which forms the basis of deformation monitoring and analysis. Chapter 3 the principles of Atmospheric Phase Screen (APS) estimation and a method developed using auxiliary data for APS estimation. The key steps of the procedure applied to a study area are presented and the pros and cons of the method is discussed. Chapter 4 discusses a data driven procedure to obtain terrain deformation maps, by splitting the phase of the interferograms into low frequency and high frequency interferograms. These approaches aim to exploit Sentinel-1 highly coherent interferograms and their short revisit time to obtain high density of PSs. The effectiveness and limitations of the approach is illustrated through analyses performed on different test sites. Chapter 5 depicts another two data driven methods called Direct Integration (DI) and PSIG-STB (Persistent Scatterer Interferometry Geomatics short temporal baseline). The DI approach aims at providing a

very fast and straightforward approach to screen wide areas and easily detect active areas. However, it lacks robustness and its usability lies on the operator experience. The second method, called, provides a constrained application of the PSIG chain, the CTTC approach to the PSI. It uses short temporal baseline interferograms and does not assume any deformation model for point selection. It is also quite a straightforward approach and a perfect complement to the direct integration approach

Chapter 2

Persistent Scatterer Interferometry

2.1 SAR systems

Radar (radio detection and ranging) is an electronic tool used to detect objects, its position and/or its movement direction. Synthetic Aperture Radar (SAR) is an image system which consists of a radar sensor mounted in a platform that transmits and receives microwave signals while it moves along a given trajectory. It is a complex system that provides high resolution images of the Earth by exploiting the movement of the radar sensor along the trajectory of the platform where it is mounted. SAR systems can be ground based, when the platform is located at the ground, airborne or satellite based. In this thesis, data acquired by satellite SAR systems is exploited.

Satellite SAR is an active system that provides continuous all weather, day-and-night imagery. The radar sensor travels at constant altitude and velocity along the satellite orbit, i.e., the azimuth direction or the flight direction, and emits the electromagnetic beam as pulses, perpendicular to the azimuth direction, i.e., the line-of-sight direction or the range direction as shown in figure 2.1.The slant range is measured between the radar and the scatterer, and the ground range refers to the range between the position directly underneath the radar and the scatterer.

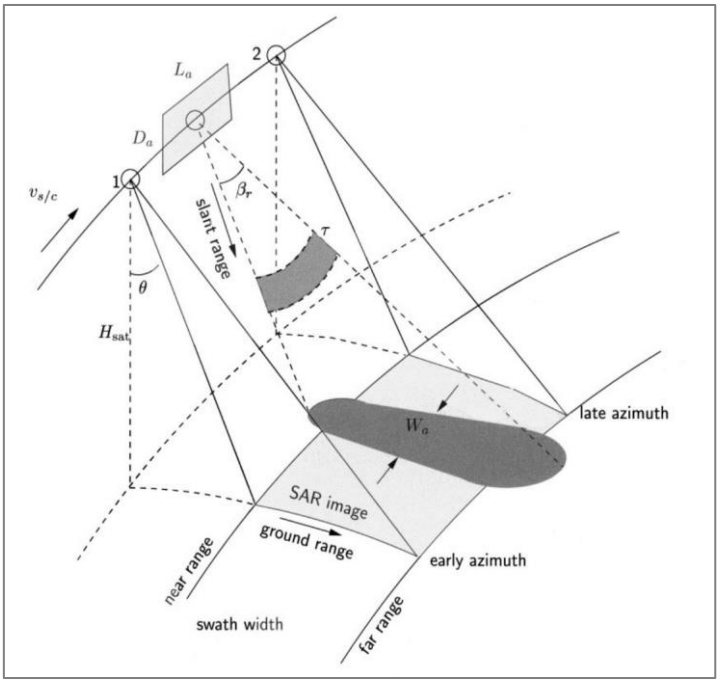

Figure 2.1. Side-looking image geometry of a space borne SAR acquisition.

Satellite SAR systems have side looking imaging geometry, as shown in figure 2.1, that can acquire in ascending and descending trajectories, i.e., the satellite travelling from south to north or from north to south, respectively. Side looking is a technical requirement in order to avoid ambiguous echoes from targets located at the same distance but at different sides with respect to the zenith of the satellite. However, the side looking geometry, which captures the three-dimensional geometry of the Earth into a side looking planimetric image, often leads to geometric distortions such as foreshortening and shadows [62] in the radar images, which must be properly analysed.

SEASAT was the first satellite platform with a SAR sensor on board, launched in 1978 [57]. Since then, the number of available SAR satellites has grown significantly as shown in Figure 2.2 providing a wide range of possibilities in terms of resolution and wavelength. The latest in this category, the ESA SENTINEL-1 satellites, was the first constellation with systematic acquisition policy with worldwide coverage each 6-12 day.

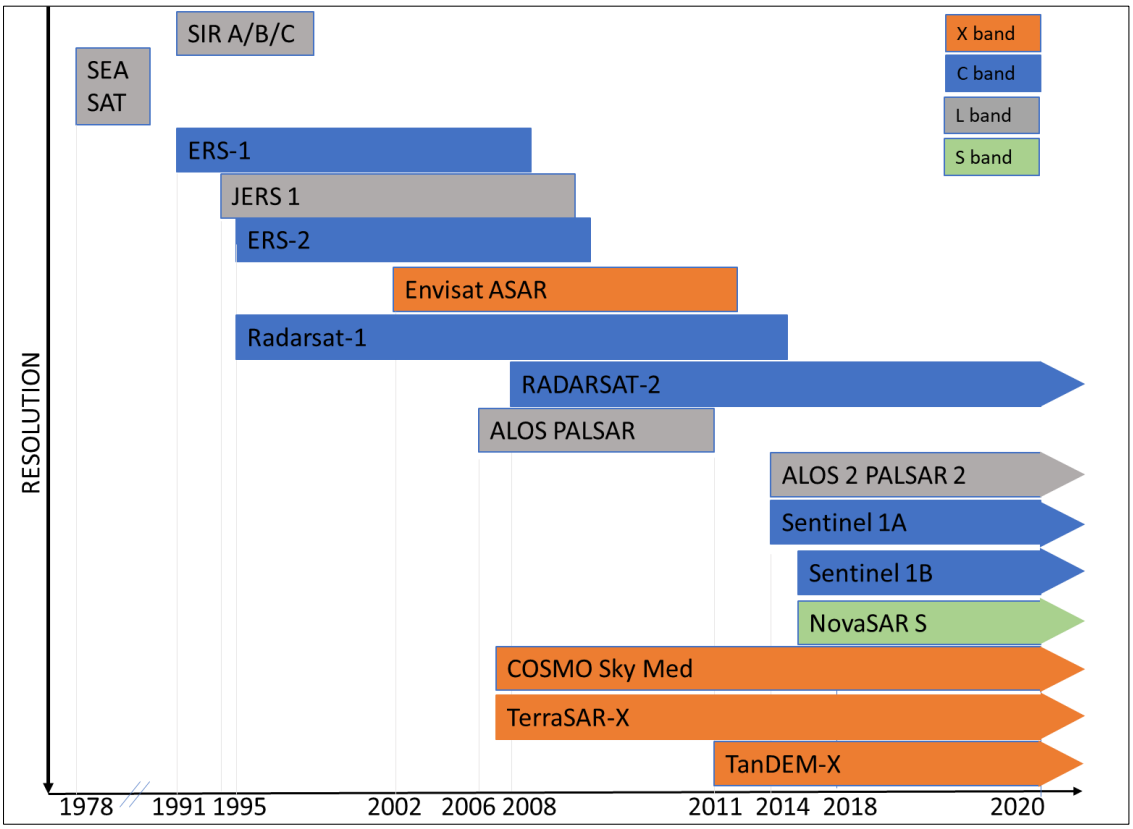

Figure 2.2 Important historical, ongoing and future SAR missions

2.2. SAR image

A SAR system transmits electromagnetic pulses and receives the echoes of the backscattered signal. When a signal is sent by the sensor's transmitter, broadcasted at a specific energy level, it interacts with the different objects within the illuminated beam and a portion is reflected back to the sensor. SAR sensors record both phase and amplitude of the backscattered signal. The cumulative strength of the backscattered signal is represented by amplitude and the phase is the number of cycles of oscillation that the wave executes between the radar and the surface and back again. The backscatter measurements are influenced by the terrain structure, surface roughness and the dielectric constant of the scatterers. SAR system characteristics such as radar wavelength and incidence angle also govern the interaction of the signal with the scatterers [62].

A SAR image can be seen as a raster, a two-dimensional matrix formed by rows and columns of pixels, related to the azimuth and range positions of the scatterers respectively. Each pixel is associated with a small area of the Earth's surface called a resolution cell and contains the in-phase (I) and quadrature (Q)components of the radar signal, from which the amplitude (A) and the phase (ϕ) can be derived as [62]

$$A = \sqrt{I^2 + Q^2} \tag{2.1}$$

$$\varphi = arctan\left(\frac{Q}{I}\right) \tag{2.2}$$

Each pixel in a SAR image is the sum of vectors of signals from scatterers placed in the corresponding resolution cell. If the scattering properties of these individual scatterers within a resolution cell changes, or if the viewing geometry between acquisitions changes, the vector summation changes as well. This introduces noise into the phase of the signal, known as decorrelation [63]. The phase noise can be caused by temporal decorrelation of the scatterers, different look angles, etc.

2.3. SAR Interferometry

SAR interferometry exploits the phase differences between two images acquired over the same site at different times or from slightly different positions. By using Interferometric SAR (InSAR), we may derive very accurate information about topography and ground displacements.

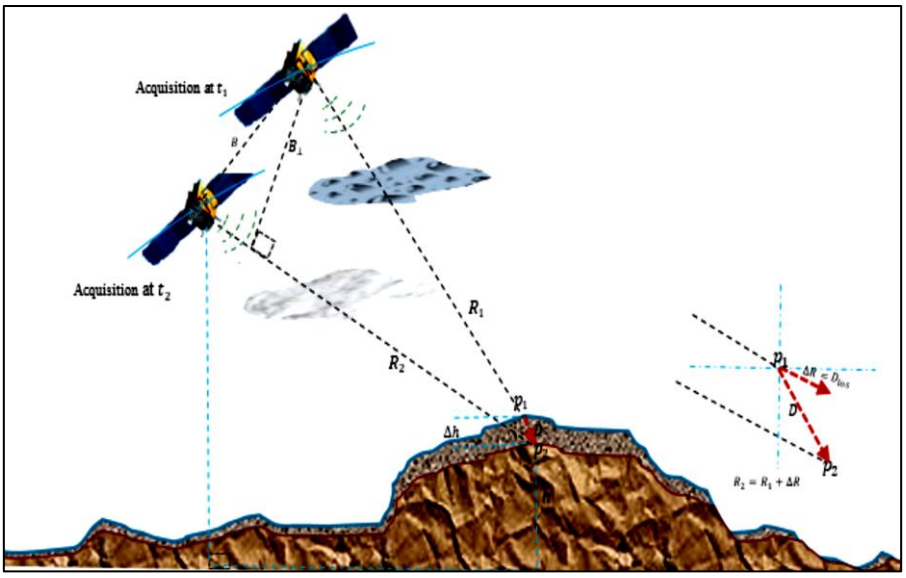

Figure 2.3. Deformation measurement using repeat pass interferometry [62]

InSAR adds a third dimension (either in space or time) to the otherwise planimetric SAR image. This can be achieved in three ways:

- Across-track interferometry- sensors capture images at the same time from different positions, i.e., the antennas are separated in the across-track direction.
- Along-track interferometry- sensors capture images at different times from the same position. Usually deployed with stationary cameras and quite impractical in space borne systems.
- Repeat-pass across-track interferometry- The sensors capture images at different times from slightly different orbital positions. This is the mode used to detect and monitor ground displacements.

Figure 2.3 shows a sketch of the geometry for repeat pass across track interferometric acquisition. The interferometric phase is related with the differences between R_2 and R_1 as follows:

$$\varphi_{Int} = \varphi_S - \varphi_M = (R_2 - R_1) \cdot \frac{4 \cdot \pi}{\lambda} \tag{2.3}$$

Where λ is the wavelength and $4 \cdot \pi$ is related to the path radar-target-radar. The vector between the two orbital positions of the satellite at times t_0 and t_1, respectively, is called the baseline (B). If B is 0, i.e. the satellite position is the same at the two acquisition times, then (R_2 - R_1) is related only to the displacement of the point p_1:

$$\varphi_{Int} = \varphi_S - \varphi_M = \varphi_{disp} \quad (2.4)$$

Otherwise, assuming the same flight altitude, the larger the B the higher the sensitivity to the acquisition geometry that indeed is modulated by the surface height changes (topography) along the scene:

$$\varphi_{Int} = \varphi_S - \varphi_M = \varphi_{topo} + \varphi_{disp} \quad (2.5)$$

Where $\varphi_{topo}$is a function of B and φ_{disp} depends only on the movement of the point p_1. The φ_{topo} is useful to reproduce the surface of the terrain which is one of the main applications of InSAR techniques.

2.4. Differential SAR interferometry

The SAR interferogram is generated by cross-multiplying, pixel by pixel, the first SAR image with the complex conjugate of the second [65, 2]. Thus, the interferogram amplitude is the amplitude of the first image multiplied by that of the second one, whereas its phase (the interferometric phase) is the phase difference between the images. As shown in Equation 2.3 the baseline and the displacement of the measured point influence the interferometric phase.

If the surface topography is known, i.e., a digital elevation model is available, then $\Delta\varphi_{topo}$can be removed from the equation 2.5 yielding to an interferometric phase related only to the displacement of the point p_1 between the two acquisition times. This interferogram is named Differential Interferogram.

$$\Delta\varphi_{dint} = \Delta\varphi_{int} - \Delta\varphi_{topo_{simulated}} = \Delta\varphi_{disp} \quad (2.6)$$

However, the phase of a SAR signal is influenced by many more components than just the ground motion and the topography. A more accurate model for the differential interferometric phase can be described as follows [62]:

$$\Delta\varphi_{int} = \Delta\varphi_{master} - \Delta\varphi_{slave} = \Delta\varphi_{disp} + \Delta\varphi_{rte} + \Delta\varphi_{Atmo} + \Delta\varphi_{noise} \quad (2.7)$$

Where,

Displacement term ($\Delta\varphi_{disp}$) is the component related to the displacement of the point between two acquisitions. Topographic term ($\Delta\varphi_{rte}$) is the geometric residual contribution to the interferometric phase. It is related to the disparities between the real topographic component and the simulated one, which are often caused by the used DEM

which usually does not exactly reproduce the real ground surface. The RTE component is related with the DEM errors through the following equation:

$$\Delta\varphi_{rte} = \frac{4\pi}{\lambda}\frac{B_{\perp}}{R_M sin\theta}H \tag{2.8}$$

where, H is the altitude of the scatterer with respect to the reference DEM, $R_M$is the range of the reference image, and θ is the look angle and $B_{\perp}$is the projection of B along the line of sight of the reference image. Note that the sensitivity to topography increases with the perpendicular baseline $B_{\perp}$.

1) Atmospheric term ($\Delta\varphi_{atmo}$) is the component related to the change in propagation time through the atmosphere between the two acquisitions.
2) Noise term ($\Delta\varphi_{noise}$) that arises due to changes in the electromagnetic scattering properties within a resolution cell over time, e.g., due to changes in soil moisture and from thermal noise processes in the SAR instrument. Also, other noise terms arise later during processing due to inaccurate compensation of the various non-deformation terms.

Moreover, the above equation is known at a wavelength level, i.e., all is wrapped in the interval [0, 2π]. Thus, we have to add a component to the equation 2.7 that is related to the reconstruction of the whole value from the wrapped value.

$$\Delta\varphi_{int} = \Delta\varphi_{master} - \Delta\varphi_{slave} = \Delta\varphi_{disp} + \Delta\varphi_{rte} + \Delta\varphi_{Atmo} + \Delta\varphi_{noise} + 2k\pi \tag{2.9}$$

where κ is the unwrapping constant of the measured point.

In order to isolate the ground displacements, the other phase components must be removed or mitigated. This implies a set of methods that includes models, statistical estimations, and filtering. There are several approaches in the literature to solve it [59].

Classic DInSAR analysis exploits single interferogram to qualitatively infer ground displacement measurements. However, it is only possible when such displacements are comparatively higher to the other components, such as in the case of seismic events. Therefore, in other events the $\Delta\varphi_{disp}$ has to be separated from other differential phase contributions for accurate measurements. In these cases, the discrimination of $\Delta\varphi_{disp}$requires of advanced procedures known as Multi-temporal or A-DInSAR based

methods. Among them, Persistent Scatterer Interferometry (PSI) is one of the most used worldwide. In the following section, a brief overview of the PSI methods evolution and a description of the main steps of the PSI approach used in this work, i.e., the PSIG chain, is provided.

2.5. Evolution of A-DInSAR techniques

In the last 25 years, the DInSAR technique has contributed significantly to ground displacement mapping and monitoring. Since the first results in 1989 [25], the technique has experienced a continuous growth. The availability of large stacks of SAR data provided the opportunity to exploit these images and promoted the development of advanced methods to improve deformation estimates. This evolution has accelerated even more in the last years with the advent of the Sentinel-1 constellation. The Sentinel-1 unprecedent systematic acquisition policy provides full coverage of the Earth globe every 6-12 days and it is made available free of charge. An overall goal of this thesis is focused on providing semi-automatic methods to fully exploit the capabilities of Sentinel-1 interferometric data to derive ground displacement measurements.

Among the multitude of DInSAR based methods for ground displacement measurement, PSI represents a specific category, which exploits multiple SAR images acquired over time to provide very accurate ground displacement measurements. PSI is based on a network of scatterers (PSs) that are characterized by a relative low noise component along the monitored period. The term PSI can be used to represent a number of techniques including the Permanent Scatterers approach (the first PSI technique proposed by Ferretti et al. [65]), other techniques based on PSs or Distributed Scatterers (DS), and other hybrid methods. Hereafter, the term PS will refer to both PSs and DSs.

The main products of a standard PSI analysis are the deformation time series and the deformation velocity estimated over the analysed network of PSs. Another product of a PSI analysis is the so-called residual topographic error (RTE), which is a key parameter in order to achieve an accurate PS geocoding.

During the last two decades, a large variety of PSI methods has been published. Several algorithms can be found in the literature: Coherent Pixels Technique (CPT) [66]; Delft Persistent Scatterer Interferometry (DePSI) [67, 68]; Interferometric Point Target Analysis (IPTA) [69]; Permanent Scatterer InSAR (PSInSAR^{TM}) [40, 65]; Persistent Scatterer Interferometry Geomatics (PSIG) [70]; Persistent Scatterer Pairs (PSP) [71];

Quasi Persistent Scatterers (QPS) [72]; Small Baseline Subset (SBAS) [44,73]; Stable Points Network (SPN) [74,75]; SqueeSAR™ [31,76]; and Stanford Method for Persistent Scatterers (StaMPS) [77, 78].All these methods may employ different approaches for achieving the estimation of ground displacements, but they all generate ground motion estimates, which can be compared. The phase quality of the results can also be estimated in a variety of ways such as using temporal coherence, statistical quality indicators, etc [79, 80]. However, each of the methods inherently possess unique strengths and weaknesses, and no method can provide optimal results for all case studies. This means that, for a generic case study, it is foreseen that a set of complementary methods will need to be applied. The PSIG chain is the foundation on which all other methods in this study are developed. The following section provides an overview of the PSIG main steps.

One of the major common constraints of PSI approaches is that the PS quality is limited to scatterers that exhibit sufficiently high coherence in time which typically leads to low PS density. The PS density is usually low in vegetated, forested and low-reflectivity areas (e.g., very smooth surfaces), and in steep terrains facing the radar sensors. Snow coverage, constructions work, street re-pavement, etc. can cause the complete or partial loss of PSs. By contrast, PSs are usually abundant on buildings, monuments, antennas, poles, conducts, exposed rocks or outcrops, among others.

Different PSs approaches have faced this problem. The SBAS technique represents an approach based on using small temporal and geometric baselines to limit phase decorrelation, and multi-looked data to reduce phase noise. This results in an increased spatial sampling with respect to the classical PSI approaches. However, it leads to a loss of resolution of the measured points. In this thesis we propose approaches that combine principles of the PSI and SBAS methods to improve the density of the measurements while keeping the maximum spatial resolution.

2.6. PSIG chain

The main steps of the PSIG chain, illustrated in Figure 2.4., are described in this section. The main objective of the PSIG chain is to extend the interferometric processing to wider areas using a unique, redundant and connected network of points for any type of interferometric SAR data. A description of the main steps of the PSIG chain and their relation to the developments achieved in this work are described in the following sections.

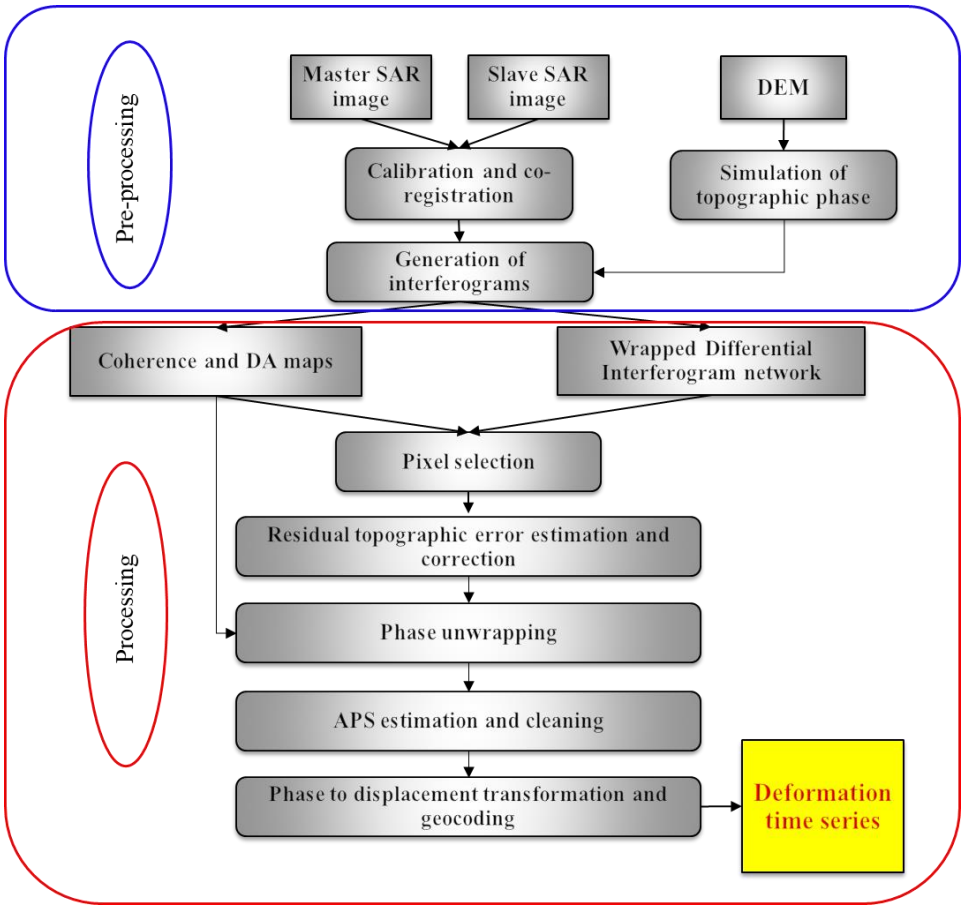

Figure 2.4. PSIG workflow

2.6.1. Pre-processing: the main objective of this step is interferogram generation which includes the standard interferogram processing steps: geometric calibration, image co-registration and differential interferogram calculation. The input is a stack of N co-registered SAR images and M wrapped interferograms, with M>>N. One important aspect is the interferogram network generation. In this work, all the possible interferograms below a temporal baseline threshold are generated. This threshold is fixed considering the available temporal sampling density. With the Sentinel-1 temporal revisit time, the threshold ranges between 30 and 108 days.

2.6.2. Ground displacement estimation: The estimation of a deformation time-series map from a stack of interferograms is the main challenge addressed in this study. Different types of data driven approaches are developed, customized and selected depending upon the test area size (regional or detailed), topography (urban, vegetated, and inundated), type of deformation (fast, slow), etc. Some of the methods used in this study are based in the PSIG chain. These steps have been customized according to the

study area and the accuracy demands of the deformation analysis. Here below I focus on the main steps addressed in this work.

2.6.2.1. Pixel selection: The pixel selection addresses the $\Delta\varphi_{noise}$ component of Eq. 2.7. As discussed before, PS nature relies on the behaviour of the noise component along time. Even if a single Sentinel-1 frame contains millions of pixels, only a small portion of them is exploitable for deformation purposes. The general objective of this step is to find a good compromise between the quality of the selected points (barely affected by noise) and a good spatial coverage. The most common methods available for potential PS and DS identification are [40]:

1) Signal-to-Clutter Ratio (SCR) - SCR is based on the assumption that an amplitude return is a deterministic signal disturbed by randomly Gaussian distributed clutter. The clutter reflects the distributed scatterers in the surroundings of the potential PS. A point scatterer with a high SCR through time is a potential PS.

2) Amplitude dispersion (DA) - The amplitude dispersion method [1] performs an amplitude time series analysis on a pixel-by-pixel basis. It calculates the scatterer stability by means of the analysis of the amplitude along the stack of N images. Each pixel is quantified by the ratio between the standard deviation (σ_A) and the mean (μ_A) of the amplitudes through time:

$$\mathrm{DA} = \frac{\sigma_A}{\mu_A} \tag{2.10}$$

   Point scatterers with a low amplitude dispersion can be selected as potential PS. The DA is a pixel-wise selection method that works at full resolution, also enabling the selection of isolated points. Sometimes the threshold is fixed as a trade-off between phase quality and spatial coverage.

3) Coherence - The complex spatial correlation coefficient of two SAR images is known as coherence. A high coherence implies a consistent phase relationship between the neighbor points. Phase stability is analysed on the assumption that phase is spatially correlated, which leads to the averaging of the phases of neighbouring potential scatterers and selecting the point targets with the lowest residual noise. The complex coherence γ of a given interferogram is a statistical index that measures the degree of correlation between the pair of complex SAR images that constitute the interferogram:

$$\gamma = \frac{E[M.S^*]}{\sqrt{E[|M|^2]E[|S|^2]}} \quad (2.11)$$

where M and S are the master and slave complex SAR images, E is the expected value and * is the complex conjugate. The coherence is usually calculated over windows of neighbouring pixels and, for this reason, the coherence image has lower resolution than the original full resolution SAR image. Hence coherence criteria cannot be used for full resolution analysis. However, it can be a good indicator to detect noisier images to be skipped from our analysis stack.

Pixel selection is a critical step for PSI methods. The thresholds are usually fixed to get a good compromise between point density and reasonable level of noise. However, this is not always straightforward. Relaxing the threshold leads to the inclusion of high level of noise PSs in our network and, thus, to an important source of errors in the ground displacement measurements. In this work, I propose different approaches to improve point density by mitigating the adverse effects of these noisier points. This is addressed in Chapters 4 and 5.

2.6.2.2. Topographic error estimation and correction: In this step, the topographic error of the DEM ($\Delta\varphi_{RTE}$) used for interferogram generation is estimated for each one of the PSs selected in the previous step. There are two goals to be achieved through this step: firstly, to remove the contribution of the DEM errors from our interferometric phase, which is the key to mitigate the effects of $\Delta\varphi_{RTE}$ on phase unwrapping errors. Secondly, the $\Delta\varphi_{RTE}$ allows to accurately geolocate the points on the ground. The approach used is described in [46] and is based in the maximization of the function:

$$\gamma = \frac{1}{N-1}\left|\sum_{i=1}^{N-1} e^{-j\left(\Delta\varphi_i - f\left(e_{top}, Bp(\Delta\varphi_i)\right)\right)}\right| \quad (2.12)$$

where γ is the gamma value, also called temporal coherence; N is the number of images which generated theN-1 interferograms.$\Delta\varphi_i$ is the ith interferogram of our network; and f is the function that estimates the corresponding phase in an interferogram with the same perpendicular baseline of $\Delta\varphi_i$ and with a topographic error e_{top}. The algorithm is based on brute force. A range of potential topographic errors is tested and the one that reaches the maximum γ is selected. The γ ranges between 0 and 1. The higher the value the better the agreement between topographic model and observations. Only those points with a γ higher than a given threshold are selected for the subsequent steps.

There are several reasons that can lead to a drop in γ. The higher the disagreement between the phase model and the real terrain the lower the γ values are. This disagreement can be caused by different components such as noise, ground displacements and/or the atmospheric phase component. An increase in noise is usually linked to an increase in temporal baseline. This is particularly critical in natural and vegetated areas. At the same time, the displacement component can cause a decline in γ when the temporal baseline is big enough to make it significant. Sentinel-1 revisit policy allowed us to set networks of interferograms with very low temporal baselines, high coherence and negligible influence of ground displacement on the estimation of $\Delta\varphi_{RTE}$. Thus, temporal coherence becomes a more robust estimator of the level of noise of a measured point. A specific objective of this thesis is to analyse different network configurations with the aim of optimizing the $\Delta\varphi_{\mathrm{RTE}}$estimation and obtaining a denser and more reliable network of PSs. This is addressed in Chapter 4.

2.6.2.3. Phase unwrapping: this step exploits a two-step phase unwrapping described in [70], 2+1D phase unwrapping. The first step consists in a spatial phase unwrapping. The algorithm used is based on the Minimum Cost Flow method [71] and is performed for each interferogram of the network and only using the points selected in the previous step. The second step is carried out point wise and performs a temporal consistency check of the unwrapped interferograms. The approach consists in solving the following system for each point:

$$\begin{cases} \Delta\varphi_{ij(unwrapped-etopofree)} = \overline{\varphi_j} - \overline{\varphi_i} \\ \overline{\varphi}_0 = 0 \end{cases} \quad (2.13)$$

The solution is obtained by iterative least squares with outlier rejection and the system stops when the following condition is fulfilled:

$$\left|\Delta\varphi_{ij(unwrapped-etopofree)} - \left(\overline{\varphi_j} - \overline{\varphi_i}\right)\right| \cong 0 \; \forall i \; and \; \forall j \in [i, i+5] \quad (2.14)$$

$\Delta\varphi_{ij(unwrapped-etopofree)}$ is the unwrapped phase of the interferogram calculated using the images i, j and after removing its $\Delta\varphi_{RTE}$,$\overline{\varphi_j}$ and $\overline{\varphi_i}$ are the estimated phases. The final output of this step is, for each point, the temporal evolution of the phase, i.e., the time series.

Phase unwrapping errors are the most important source of errors in PSI techniques. The 2+1D phase unwrapping algorithm aims to provide quality indicators about the reliability

of the phase unwrapping for each point. However, the number and the significance of these errors will strongly depend on the quality of the PS network selection as well as its combination in time. The particularity in the context of Sentinel-1 is the network used since the high temporal sampling allows redundant networks to be produced with more than five interferograms per image with maximum temporal baselines of 30-60 days. This redundancy very much mitigates the loss of points caused by temporal decorrelation.

In this thesis, three approaches are proposed as complementary methods to the PSIG chain, aimed at reducing phase unwrapping errors and improving the density of points. These approaches are fully based on the performances of the Sentinel-1 constellation. However, they can be extended to other constellations when the requirements are met. Chapters 4 and 5 address the aforementioned approaches.

2.6.2.4. Atmospheric phase screen (APS) filtering: one of the critical steps in PSI processing is atmospheric filtering. The most common approach consists of the application of space-time filters that are generally governed by strong hypotheses about the atmospheric signal, such as high spatial correlation and low temporal correlation. In particular, the PSIG chain exploits the Butterworth filter (a low-pass filter) to remove the atmospheric contribution to the phases φ_i (very low spatial phase variation) followed by a temporal filter to separate the APS signal from the temporally correlated components, usually associated with terrain deformations.

However, this strong assumption that allows to systematically remove APS effects may not be fulfilled and lead to erroneous results such as: signs of false displacements caused by unfiltered very local atmospheric phenomena, loss of real displacement areas such as those that affect large areas and with time series with not strong temporal correlation, or loss of part of the deformation signal because part of it is filtered as atmosphere Moreover, the APS signal can be an important source of phase unwrapping errors, especially when its spatial behaviour has a turbulent nature. Again, the success in the phase unwrapping in these conditions is strongly linked to having enough spatial density.

In this thesis, I analyse different approaches to remove the APS component, which are based on weaker hypotheses, and that allow its removal before phase unwrapping is performed. Again, such approaches are fully based on the very high coherent interferograms provided by the high revisit time of the Sentinel-1 constellation. Chapters 3 and 5 address the atmospheric phase filtering methods proposed.

As an overall summary of the chapter, this thesis focuses on methods that exploit the short temporal baselines provided by Sentinel-1 to: (i) improve the PS density provided by the standard PSI approaches keeping the level of quality; (ii) improve APS estimation by proposing methods with weaker hypothesis than the standard ones; and (iii) mitigate the effects of APS and noise in the phase unwrapping approach, thus improving the PSI measurements quality. These goals are achieved by providing alternative approaches to the PSIG chain to obtain: (i) fast assessment of studied areas; (ii) better selection of points; and (iii) mitigation of phase unwrapping errors incidence in the final displacement maps. In summary, better and more reliable ground displacement maps. All these methods are described and tested in the following chapters.

Chapter 3

APS estimation with auxiliary data and Saastamoinen model

3.1. Introduction to APS

As discussed in the previous chapter, a SAR image records both the amplitude and the phase of radar signals. The recorded phase values provide information on the slant distance (range) from the radar antenna to a ground resolution cell. Any resolution cell in a SAR image is arranged according to its range and its location along the azimuth of the radar platform. The azimuth location is determined from Doppler frequency shift. The range dimension is however ambiguous since different points in a single resolution cell can have the same range [61]. Therefore, two SAR images are always combined to resolve the ambiguity to generate the three-dimensional terrain or deformation information. In general, two SAR images are combined by the complex conjugate multiplication of the images. This forms a SAR interferogram. The commonly used InSAR configurations are the across-track, along-track or the repeat-pass interferometry. The atmospheric effects are assumed to be cancelling out in across-track and along- track interferometry, as the atmospheric conditions are very similar for the two SAR images. In repeat-pass interferometry, however, the atmospheric effects can become very significant as the atmospheric conditions can vary considerably between the two acquisitions. We hereinafter will limit our discussions to repeat-pass InSAR interferometry only. We limit our discussion to repeat pass SAR interferometry in this thesis.

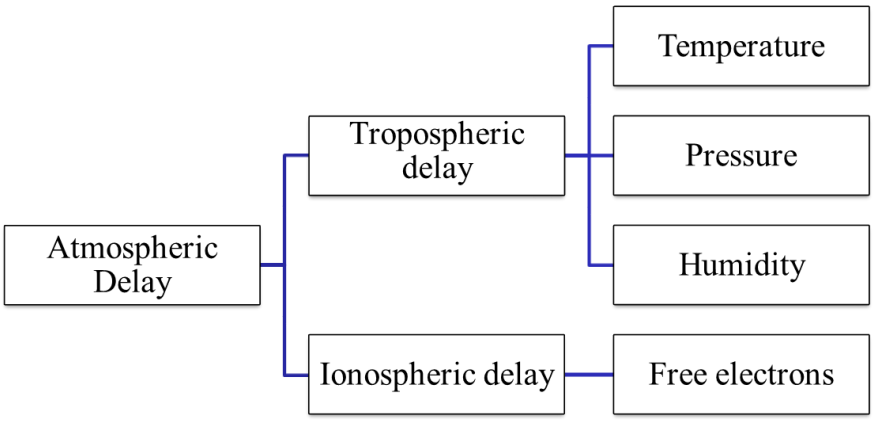

Figure 3.1. Parameters affecting APS estimation

Chapter 3 was presented as a conference paper in the 2018 ISPRS TC III Mid-term Symposium "Developments, Technologies and Applications in Remote Sensing", 7–10 May, Beijing, China. Krishnakumar, V., Monserrat, O., Crosetto, M., & Crippa, B. (2018). Atmospheric phase delay in Sentinel SAR interferometry.

Atmospheric artefacts in SAR interferograms are mainly due to changes in the refractive index of the medium. The atmosphere is divided into many different layers out of which the two major layers troposphere and ionosphere are responsible for the artefacts in the interferograms. The troposphere which is the lowest portion of the Earth's atmosphere contains 99% of water vapour and aerosols. Propagation delays are caused due to air refractivity gradients of the troposphere [81]. Free electrons and ions that define the refractive index in this area [82] characterize the ionosphere, which is located at a height of 50 km-1500 km. The effects of these layers on the phase of an interferogram have been subjected to detailed study in many research works. Changes in the refractive index can be caused by three parameters: pressure, temperature and water vapour. In most cases, the spatial variation of pressure and temperature is not large enough to cause strong, localized phase gradients in SAR interferograms. Their effects are smaller in magnitude and more evenly distributed throughout the interferogram when compared with that of the water vapour, and sometimes difficult to be distinguished from errors caused by orbit uncertainties [82, 80]. The artefact caused by localized water vapour generally dominates the atmospherically induced artefact in SAR interferogram. Water vapour is mainly contained in the near-ground surface troposphere (about 2 km above ground), where a strong turbulent mixing process occurs. Turbulent mixing will result in 3D spatial heterogeneity in the refractivity and can cause localized phase gradient in flat and mountain regions as well [82, 80]. Besides turbulent mixing, another atmospheric process with clear physical origin is vertical stratification. Vertical (stratification results in the nearly vertically distributed refractivity profile and will affect mountain region only [82, 80].

This chapter will provide a theoretical review on the issues of the atmospheric effects on InSAR, along the lines of the APS estimation model implemented in the study area of Canary Islands. We will examine the principles of atmosphere interaction with radar signal and repeat-pass InSAR. The limitations of using auxiliary data for APS estimation are discussed by demonstrating the implementation of the atmospheric model in an area such as an island with complex geophysical phenomena.

3.2. Methodology

In this section is described the research implemented up to now. The main target of the procedure is to derive the deformation activity maps, with as maximized accuracy as possible. The procedure can be applied to any satellite SAR sensor. However, it

provides the best performances with the S-1 characteristics. The procedure is divided in two blocks (see Figure 3.2):

1) SAR data processing: that includes all the processing steps to derive the deformation map. It also includes phase unwrapping and improvement of phase unwrapping. It mainly addresses the objectives 1 and 4 listed in the objectives section.
2) Atmospheric Phase estimation: Includes the procedure to calculate the total atmospheric phase delay and separate the hydrostatic wet delay caused by the water vapour. It mainly addresses the objectives 2 and 3 listed in the objectives section.

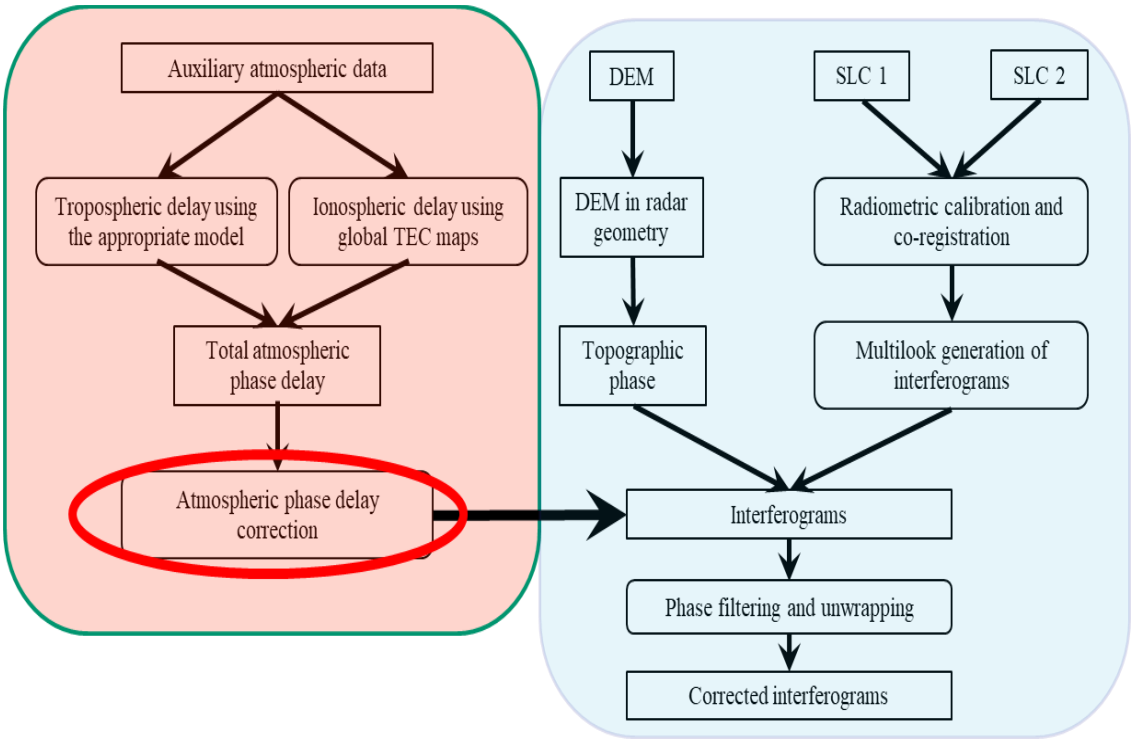

Figure 3.2. Methodology showing pre-processing of interferograms and APS estimation.

3.3. Atmospheric Refraction Delay

The refractivity index N can be expressed as [83]:

$$N = k_1 \frac{P_d}{T} + k_2 \frac{e}{T} + k_3 \frac{e}{T^2} \quad (3.1)$$

Where P_d is the partial pressure of dry air in mbar, T is the temperature in kelvin, e is the partial water vapour pressure in mbar and k_1, k_2, k_3 are constants of atmospheric refractivity. A significant number of different k_1, k_2 and k_3 values have been suggested in the past fifty years, e.g., Smith and Weintraub [83], Boudouris [84] and Thayer [85] (see Table 2.1) among others.

Table 3.1. The constants of atmospheric refractivity proposed by different authors

Authors	k1	k2	k3
Smith and Weintraub	77.607 ± 0.013	71.6 ± 8.5	3.747 ± 0.031
Boudouris	77.59 ± 0.08	72.0 ± 10.5	3.754 ± 0.030
Thayer	77.604 ± 0.014	64.79 ± 0.08	3.776 ± 0.004

We have adopted the commonly used Thayer's constants in this work. The RADAR signals are subjected to propagation delay that is explained in the following equations.

$$\psi_1 = \frac{4\pi}{\lambda}(L_1 + \Delta L_1) \tag{3.2}$$

$$\psi_2 = \frac{4\pi}{\lambda}(L_2 + \Delta L_2) \tag{3.3}$$

Where, $\psi_1$is the phase measured during first image acquisition,$\psi_2$is the phase measured during second image acquisition,$L_1$is the slant range during first image acquisition, $L_2$is the slant range during second image acquisition , λ is the wavelength of the RADAR signal, ΔL_1= atmospheric propagation delay corresponding to first acquisition, ΔL_2= atmospheric propagation delay corresponding to second acquisition. From the above equations, the interferometric phase is

$$\varphi = \psi_1 - \psi_2 = \frac{4\pi}{\lambda}(L_1 - L_2) + \frac{4\pi}{\lambda}(\Delta L_1 - \Delta L_2) \tag{3.4}$$

Where, $\frac{4\pi}{\lambda}(L_1 - L_2)$ is the topography and surface deformation induced interferometric phase $\frac{4\pi}{\lambda}(\Delta L_1 - \Delta L_2)$ is atmosphere induced interferometric phase. The layers of the atmosphere that affect the propagation of radio waves are the ionosphere and troposphere. The difference in the refractive indices of the atmospheric layers affect the propagation of electromagnetic waves. The repeat-pass InSAR shows random variations in phase due to atmospheric heterogeneities giving inaccurate measurements [86]. From the previous research on atmospheric phase screen estimation, the primary difference between tropospheric and ionospheric effects on InSAR can be inferred. Troposphere leads to an increase in observed range or phase delay whereas ionosphere leads to a decrease in observed range or phase advance. Hence, the total atmospheric delay can be written as

$$\Delta\phi_{atmosphere} = \Delta\phi_{troposphere} + \Delta\phi_{ionosphere} \tag{3.5}$$

The ionosphere extending from a height of 50 km to 1500 km above the Earth's surface is characterized by free electrons, which are caused due to external sources like solar radiation. A complete survey of the potential ionospheric effects on the performance of space-based SAR systems has been carried out by Xu et al,.[87]. The ionosphere affects the signal delay proportionately to λ^2. The number of free electrons in the ionosphere is represented by electron density, in electrons per m^2. RADAR signals traveling through the ionosphere are delayed along their paths by interactions with these free electrons. Thus, the ionospheric delay can be regarded as a path integral through the ionospheric electron density [88]. This integral is known as the Total Electron Content (TEC). The electron density varies diurnally, seasonally and geographically. Two approaches are mentioned here which can be applied for phase correction.

1) Split spectrum processing: the phase bias is estimated from each spectrum phase, which is obtained by dividing the single spectrum into several spectrum components.
2) The GPS technique: a global TEC map can be derived with the aid of GPS information, which can be used to estimate phase corrections. The global TEC map produced by the Centre for Orbit Determination in Europe (CODE) on a daily basis.

While at X-band and C- band frequencies the effects are small, current and future L-band systems would benefit from ionospheric compensation. Hence, in this study, we have assumed that the ionospheric phase has a negligible part to play in the APS estimation. Hence, the main contribution is assumed to be from tropospheric phase delay, especially from the wet delay in that.

The troposphere, which is the lowest portion of the Earth's atmosphere, contains 99% of water vapour and aerosols. The path delay due to troposphere is caused due to air refractivity gradients [89]. The air refractivity gradients in the troposphere are due to the dry air pressure, temperature, air moisture and condensed water in clouds or rain. Propagation delay results in an excess path length, which is caused by variations of refractivity. This excess path length is given by

$$\Delta R_e = 2 * 10^{-6} \int_0^H \frac{N}{\cos\theta} dh \tag{3.6}$$

Where, H is the Vertical distance travelled by the RADAR wave in m, N is the Refractivity, θ is the Incidence angle, H is the topographic height. In most cases, the

spatial variations of pressure and temperature are not large enough to cause strong, localized phase gradients in SAR interferograms. Their effects are generally smaller in magnitude and more evenly distributed throughout the interferogram when comparing with that of the water vapor [90].

3.4. APS estimation case study

The tropospheric zenith delay can be estimated from auxiliary data such as GPS observations or meteorological data. This enables the atmospheric effects on InSAR measurements to be evaluated and calibrated to certain extent. Since in general the density of network is much lower than the SAR resolutions, interpolation is needed for un sampled pixels in a SAR image. Although there exist different interpolators, those that are able to take into consideration the turbulent nature of the atmosphere are preferred in this case. An attempt was made to capture the tropospheric effects using the Saastamoinen model with the ground level meteorological data from the Spanish Agencia Estatal de Meteorología (AEMET) as an input, acquired over the Canary Islands lying within the latitude (30, 25) and longitude (-20, -10). The study area presented here is The Tenerife Island is the biggest island of the Canaryian archipelago (Spain), located in the Atlantic Ocean off the coast of Africa. The Canary Islands is notable for the volcanic and sharp mountains, hence is a highly prone area to landslides and slope failures.

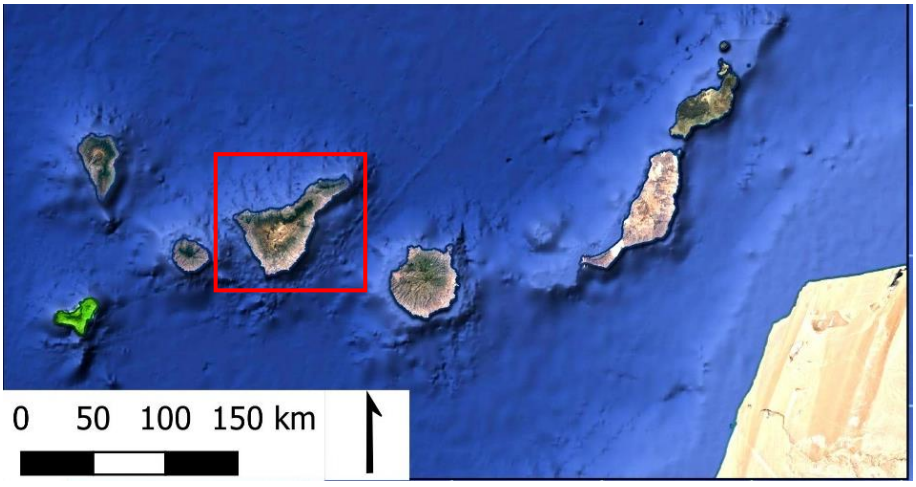

Figure 3.3. Study area of Canary Island and Tenerife used for demonstration of Saastamoinen model to estimate atmospheric phase

sl	station	lat	long
1	Gran Canaria Aeropuerto	27.91778	-15.383
2	Agaete	28.10111	-15.828
3	Agüimes	27.9025	-15.4539
4	Arucas	28.14167	-15.5069
5	La Aldea de San Nicolás	28.00111	-15.8075
6	La Aldea de San Nicolás, Tasarte	27.90889	-15.77
7	Telde	27.9875	-15.4578
8	Tejeda	27.99528	-15.6158
9	San Bartolome Tirajana, Cuevas del Pinar	27.92667	-15.6
10	San Bartolome Tirajana, El Matorral	27.8125	-15.4533
11	San Bartolome Tirajana, Lomo Pedro Alfonso	27.85694	-15.645
12	San Bartolome Tirajana, Las Tirajanas	27.92	-15.5742
13	Telde, Melenara	27.98694	-15.3778
14	Mogán, Puerto Rico	27.78	-15.7111
15	Maspalomas	27.73583	-15.5958
16	Maspalomas, C. Insular Turismo	27.75806	-15.5756
17	Las Palmas de Gran Canaria, Pl. de la Feria	28.11306	-15.4214
18	Las Palmas de Gran Canaria, San Cristobal	28.08972	-15.4161
19	Las Palmas de Gran Canaria, Tafira	28.07806	-15.4533
20	Teror	28.07528	-15.5472
21	Vega de San Mateo	27.97722	-15.5839
22	Adeje	28.08139	-16.7111
23	Antigua	28.41722	-14.0194
24	Anaga	28.50806	-16.1956
25	Arico	28.18111	-16.4836
26	Candelaria	28.35889	-16.4014
27	La Orotava, Cañadas Teide	28.22417	-16.6264
28	Izaña	28.30889	-16.4994
29	San Cristóbal de La Laguna,Llano de los Loros	28.52667	-16.2806
30	Los Silos	28.37861	-16.8175
31	La Victoria de Acentejo	28.43472	-16.4547
32	Tenerife Norte Aeropuerto	28.4775	-16.3294
33	Puerto de la Cruz	28.41806	-16.5481
34	Tenerife Sur Aeropuerto	28.04694	-16.5611
35	Sta.Cruz de Tenerife	28.46333	-16.2553
36	San Juan de la Rambla	28.38972	-16.6297
37	Agulo	28.17889	-17.2131
38	Vallehermoso, Alto Igualero	28.10694	-17.2492
39	Vallehermoso, Chipude C.F.	28.11083	-17.2633
40	Vallehermoso, Dama	28.05444	-17.3067
41	San Sebastián de la Gomera	28.08972	-17.1114

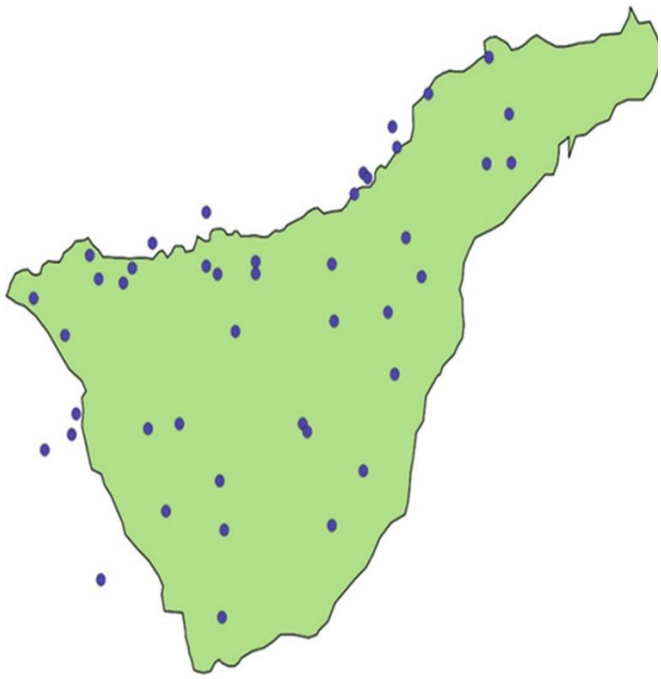

Figure 3.4. The AEMET weather stations located in and around Tenerife

The figure 3.4 shows the extent of the 41 weather stations located in the island of Tenerife. The pressure, humidity and temperature data are collected from all these stations and interpolated (using Inverse distance weighted IDW interpolation) to cover the extent of the Island.

The atmospheric phase delay is computed using the Saastamoinen model for the day of acquisition of the master and the slave separately, to be combined later to obtain a wrapped interferogram with the atmospheric phase delay. In the ideal scenario, the estimated wrapped APS is then removed from the original wrapped interferogram to obtain a residual interferogram free of the atmospheric phase. The figure 3.5 shows an example of an interferogram with strong atmospheric influence (characterized by the fringes) of 6 days temporal baseline from 20.05.2017 to 26.05.2017. The meteorological parameters from the AEMET weather stations located in the island of Tenerife was used as an input for the Saastamoinen model to calculate the wrapped atmospheric phase. The calculated phase was interpolated to cover the Island.

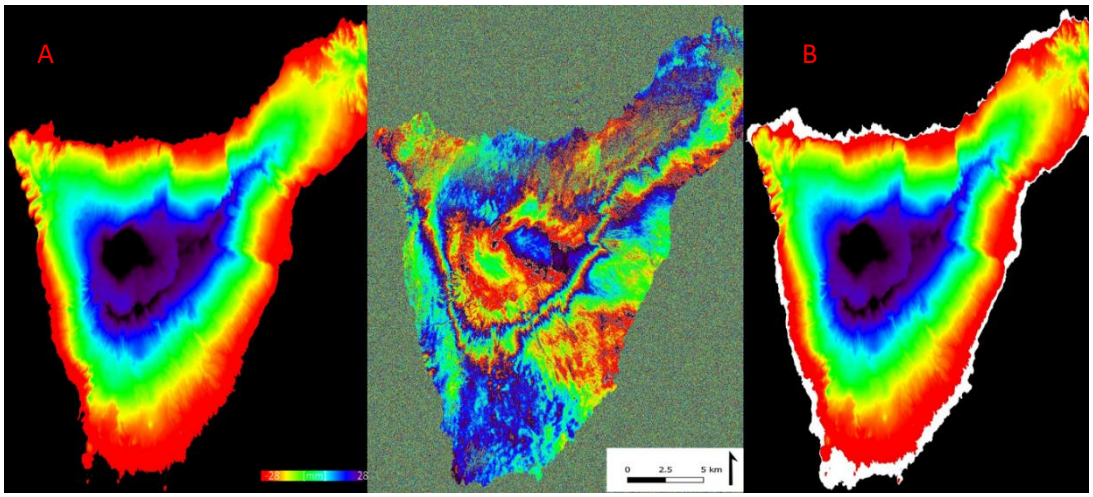

Figure 3.5 Example 1 of interpolated tropospheric phase delay using Saastamoinen model, meteorological data from AEMET weather stations for master(A) and slave(B), with the corresponding 6-day interferogram (middle).

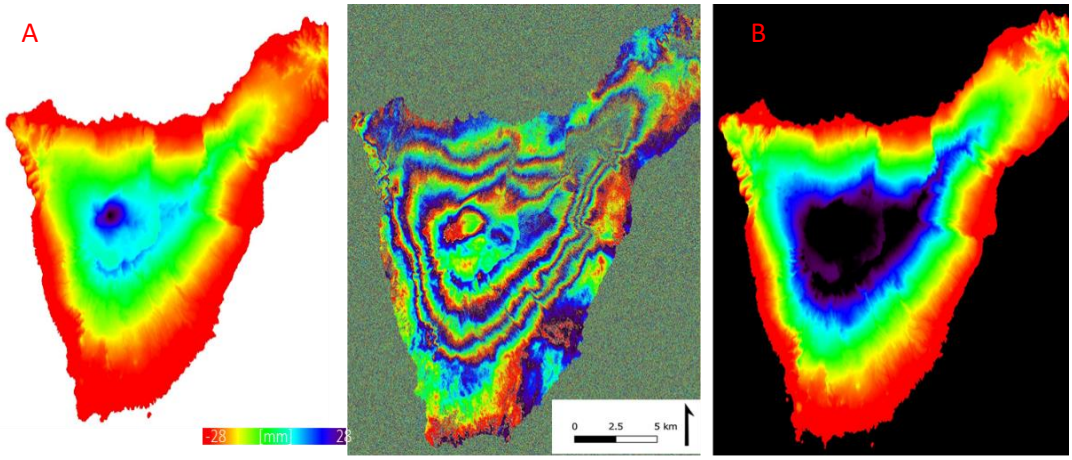

Figure 3.6 Example 2 of Interpolated tropospheric phase delay using Saastamoinen model, meteorological data from AEMET weather stations for master(A) and slave(B) example, with the corresponding 6-day interferogram with strong stratified component of the APS (middle).

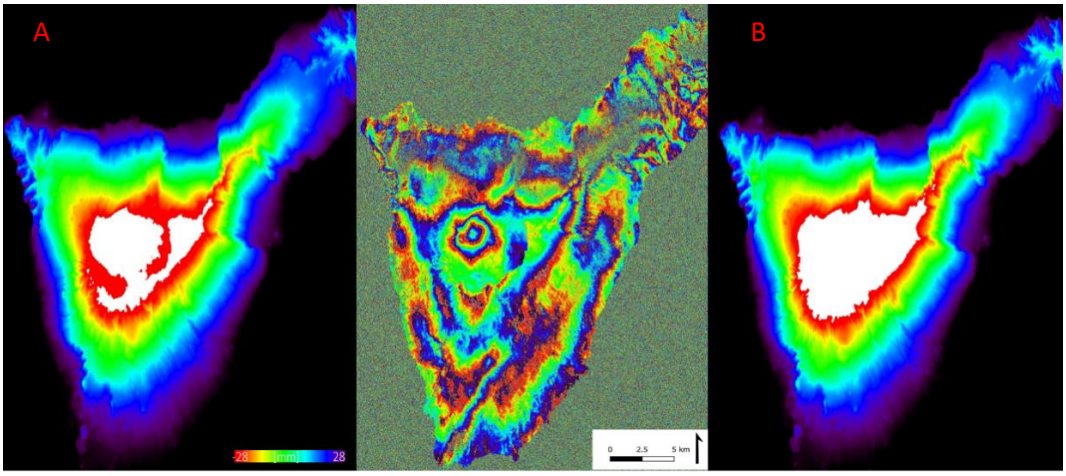

Figure 3.7 Example 3 of Interpolated tropospheric phase delay using Saastamoinen model, meteorological data from AEMET weather stations for master(A) and slave(B) example, with the corresponding 6-day interferogram with strong stratified component of the APS (middle).

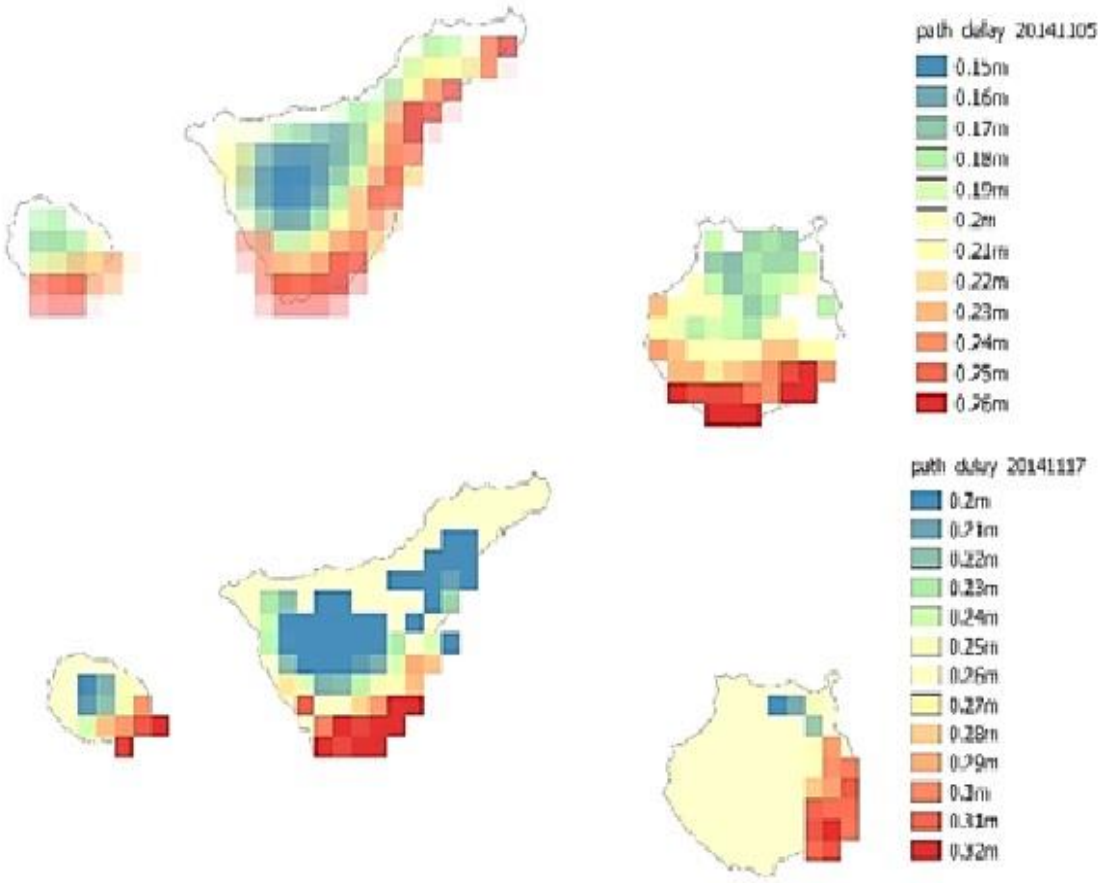

Figure 3.8 Master and Slave tropospheric path delays from MODIS data.

An attempt was also made using auxiliary data available via MODIS (Moderate Resolution Imaging Spectroradiometer) cloud product Terra (MOD06) to simulate the tropospheric phase delay. When the ground data gave a tropospheric phase delay of 0.25 m to 0.48 m, the MODIS data resulted in a delay of 0.15 m to 0.32 m. Obviously, the tropospheric path delay calculated using MODIS data is poorly estimated compared to the one from the station data. The results can be improved if input data at a greater spatial density is available. The MODIS data acquired for the Canary Islands had severe data gaps and had very low resolution.

To verify the calculated phase delay, we made use of the Generic Atmospheric Correction Online Service for InSAR (GACOS) platform by Yu et al.,[91]. This model integrates operational high-resolution ECMWF data (0.125^0 resolution and temporal sampling of 6 hours) and continuous GPS tropospheric delay estimates using an iterative tropospheric decomposition model.

It can be inferred from the examples shown above that the estimated atmospheric phase is topographically correlated. The island characterised by the presence of a volcanic mountain in the middle has meteorological parameters associated with it. Both the phase modelled using actual meteorological data, as well as the GPS observations in GACOS can be seen comparably homologous, but both fail to capture the effects of the atmosphere seen in the interferograms. Even though both approaches use different sources of input data, they use the same Saastamoinen model to construct the atmospheric phase hence failing in the process. Unfortunately, for all the interferograms, the Saastamoinen model failed to capture the highly volatile atmosphere of the island. It could also be seen that the APS interferograms for all the available interferograms were congruent. Many reasons can be conceived for the failure of the model. The first and foremost being, the scarce distribution of the data. For an island with a very turbulent environment, the extent of the distribution of weather stations was really less. Many of the atmospheric effects are localized and hence are lost in interpolation. Secondly, the Saastamoinen model remains quite simple to effectively capture the subtle phase differences. For the purpose of the demonstration of the laxity of the model, figure 3.10 shows an example of an APS interferogram for the same interferogram mentioned above, along with the interferogram obtained after removing the APS from the original wrapped interferogram.

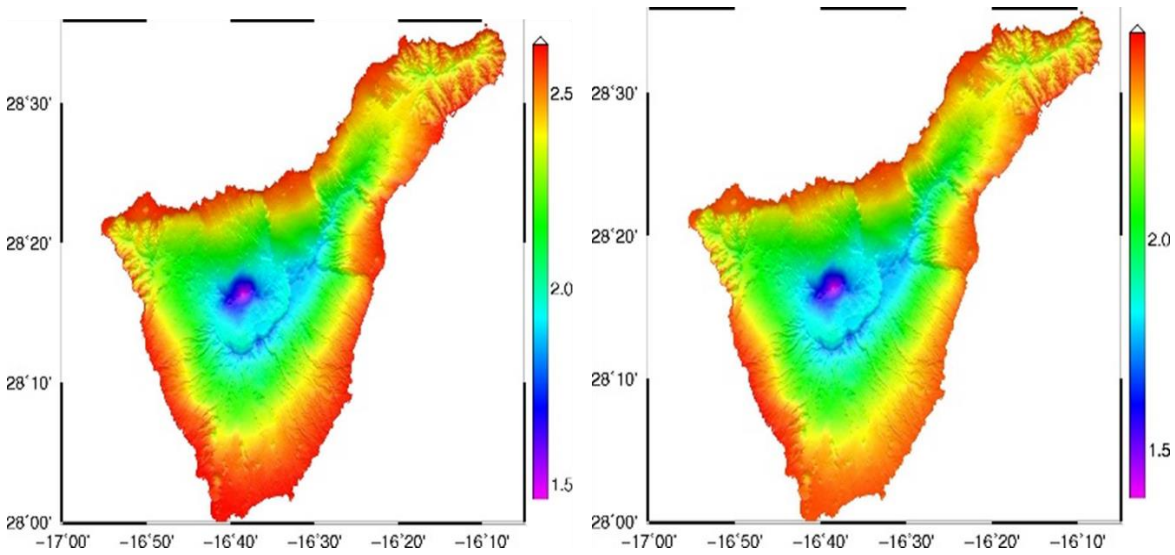

Figure 3.9 GACOS tropospheric delay map derived from ECMWRF weather data at 0.125^0 (14 km) resolution and Saastamoinen model for master and slave images example.

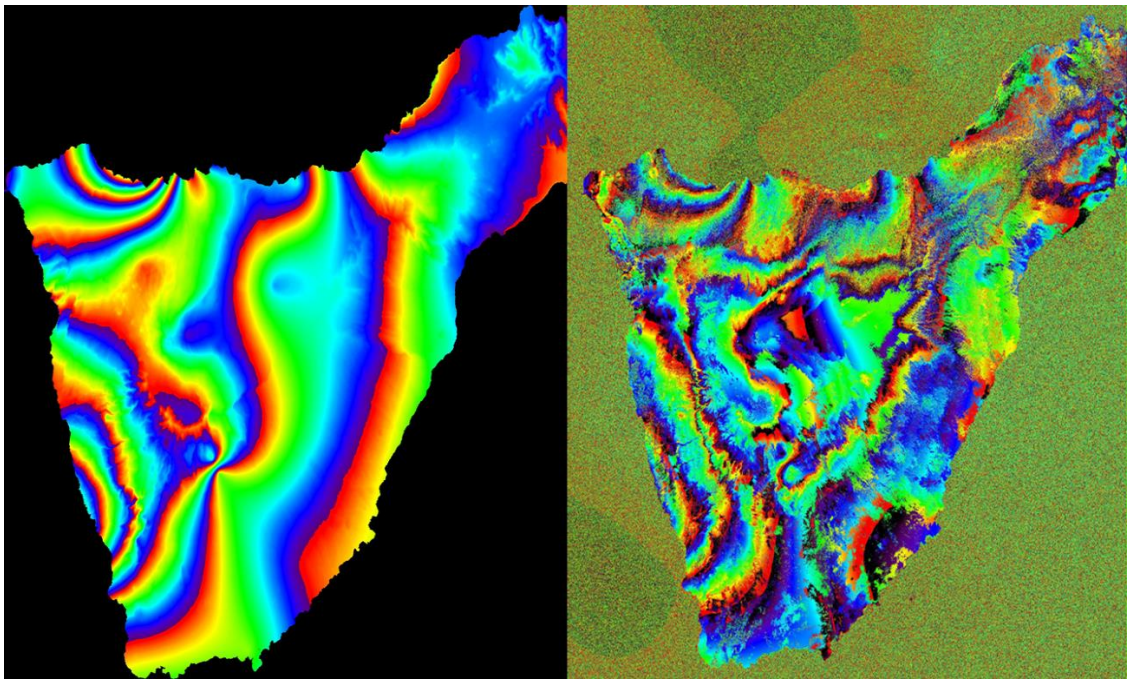

Figure 3.10 The APS interferogram estimated from the master APS and slave APS with the Saastamoinen model and the corresponding interferogram

In the example above, not only the APS interferogram fails to remove the atmospheric effects in the original interferogram but also can be seen introducing new artefacts and fringes in the original interferogram. The availability of surface data at good sampling rate spatially and temporally was the main challenge faced while using the Saastamoinen model for tropospheric phase correction. Furthermore, the difference in the source of the auxiliary data did not matter as all these methods use the Saastamoinen model. From this study, it could be inferred that, in an area like Tenerife the tropospheric delays are topography dependent. From this case study, it can be concluded that a simple atmospheric model is not effective in removing the atmospheric effects in an area of highly volatile and localized physical phenomena. The availability of more densely distributed data might make a difference in the estimation. Even though a number of studies are being conducted in the atmospheric signals of the SAR data, the spectral signatures of APS signals are not evaluated. In addition, there is a lack of models that can integrate measurements from various sources and capture the intricate nature of the atmospheric components depending on the area of study.

Chapter 4

A data driven approach – Spectrum splitting and filtering

4.1. Introduction to data driven approaches for interferogram filtering

As mentioned in the previous chapters, the cleaning of the interferograms to reduce noise and errors can be achieved in two ways, by using external data models or by data-driven methods. The previous chapter explained an approach to estimation and removal of APS has a significant contribution in unwrapping errors using auxiliary data. In this chapter, we demonstrate an approach using the interferometric phases itself, which can be manipulated, through a series of filtering and addition processes, leading to an effective cleaning of the interferogram. These filtering techniques operate in the frequency domain of the interferogram. The proposed procedure can be applied to the data acquired by any satellite SAR sensor. However, it provides the best performances with the Sentinel-1 characteristics. The case studies presented in this chapter illustrate how Advanced DInSAR based techniques can provide a detailed terrain deformation map to monitor geohazard activity in areas with complex topographical conditions. The active deformation areas (ADA) maps, aimed at geohazard risk early warning and management can also be generated quickly from the deformation and velocity maps. The procedure is complete with the deformation time series maps and ADA maps as the end products.

The use of SAR interferometry is often impeded by decorrelation from thermal noise, temporal change, and baseline geometry. Interferometric phase filtering aims to filter the noise in the interferograms while avoiding phase loss and resolution degradation. Recently, many interferometric phase filtering methods have been proposed. These methods are divided into two categories: spatial domain filtering methods and frequency domain filtering methods. Among the spatial domain filtering methods, the multi-look filter [92] is one of the most commonly used and has the best filtering effects but it has several limitations such as loss of data and addition of false signals. The spatial domain filtering techniques are used directly on pixels of an image. Frequency domain filters are used for smoothing and sharpening of an image by separating the different frequency components in the image. One of the most commonly used frequency domain filters in the interferogram processing chain is the low pass filter. In 1998, Goldstein R M et al.

Part of Chapter 4 was published as Qiu, Z., Monserrat, O., Crosetto, M., Krishnakumar, V., & Zhou, L. (2021). An innovative extraction methodology of active deformation areas based on sentinel-1 SAR dataset: the catalonia case study. *International Journal of Remote Sensing*, *42*(16), 6231-6247.

proposed the Goldstein filter, which is regarded as the classical frequency domain filtering method for noise removal [93], there are also other widely employed frequency domain filters such as Gaussian.

A signal processing filter is a process or a device used for filtering a signal from an unwanted component such as background noise. Usually, the interfering signals are suppressed by identifying and removing some frequency bands. There are various types of filters, which are classified based on various criteria such as linearity (linear or non-linear), time (time variant or time invariant), analogue or digital, active or passive, and so on. The concept of filtering is easier to visualize in the frequency domain. To work with interferograms in the frequency domain there are three basic steps to be followed:

1) The image must be transformed from the spatial domain into the frequency domain using the Fast Fourier Transform (FFT).
2) The resulting complex image must be multiplied by a filter that usually has only real values.
3) The filtered image must be transformed back to the spatial domain using Inverse Fast Fourier Transforms (IFFT).

4.2. Methodology

4.2.1. Power spectrum analysis

Power spectrum is technically a Fourier transform of the correlation function and reveals information on the correlation structure of the signal. For interferograms a power spectrum is typically the sum of the narrow-band components combined with broad-band noise and it gives the distribution of the signal among various frequencies. An image can be converted into its frequency spectrum mathematically using Fourier transforms as mentioned above. The power spectrum of an interferogram is composed of two parts: the coherent part generating the fringe, and the noise. In order to evaluate it, first, we oversample both images in range by a factor 2:1; the spectrum of each image is then a rectangle, occupying half of the available frequency range [94]. Then, we cross-multiply the two images and thus we convolve the two spectra along the range axis. The principal phase components are estimated using the frequency spectrum with an adaptive bound and are then removed from the original combined noisy phase where the residual phase corresponds to the noise components of the interferogram. If the two images are very incoherent, the resulting spectrum convolution of the two rectangles is triangular and

centred in the origin. If there is a coherent component in the two images after cross multiplication, it generates a peak at zero frequency, if the baseline is zero. The power spectrum is a plot of the magnitude of the various components of the frequency domain image. The distribution of frequencies in different interferograms are different, hence different interferograms have a different power spectrum. The radius of the power spectrum decides the cut-off frequency to be used in the low pass filter (LPF). The cut-off frequency (ω_c) of the ideal LPF determines the amount of frequency components passed by the filter. In general, the value of ω_c is chosen such that most components of interest are passed through, while most components not of interest are eliminated. Usually, this is a set of conflicting requirements. Hence, a useful way to establish a set of standard cut-off frequencies is to compute circles, which enclose a specified fraction of the total image power. In order to develop an automated process to decide the cut off frequency of interferograms, an iterative process was employed by increasing the cut-off frequency by five at every step and calculating the correlation of the residual images with respect to each other to know the extent of changes happening by increasing the cut-off. Then cut-off where the correlation becomes 0.99 was selected as the frequency cut-off for the respective interferogram. The general goal of the power spectrum analysis was to develop an automated process to split the interferograms with the best threshold to extract the deformation signals.

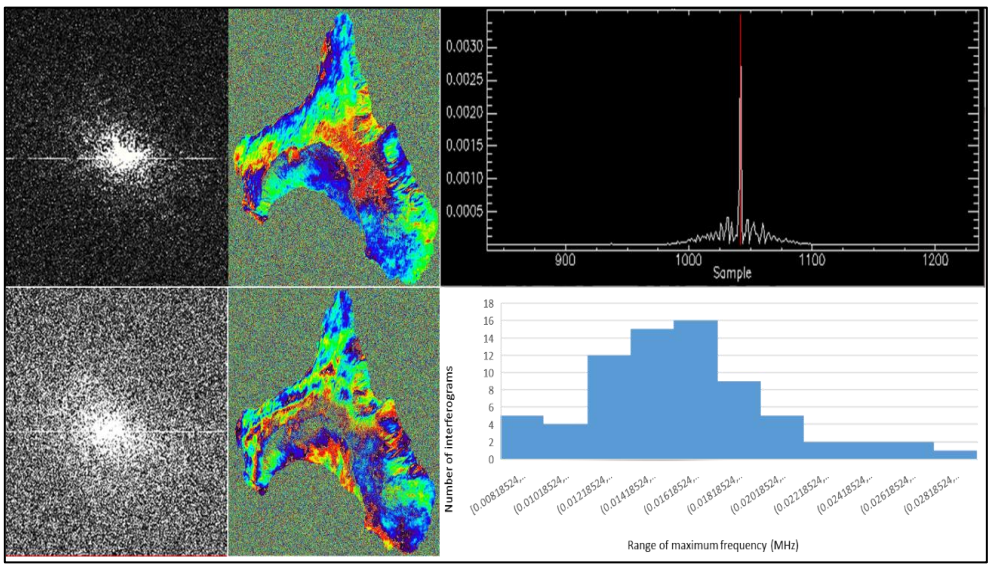

Figure 4.1. The changes in the power spectrum of the interferograms and determination of threshold frequency for the splitting of interferograms.

Table 4.1 the variation of correlation of the residuals of interferograms with respect to the cut-off frequencies

Cut-off frequency	Int 36	Int 37	Int 95	Int 96	Int 100	Int 155	Int 121	Int 122
40	0.97106	0.97150	0.97127	0.97146	0.97089	0.9718	0.97061	0.97137
45	0.97550	0.97642	0.97602	0.97612	0.97577	0.9758	0.97636	0.97551
50	0.97812	0.97964	0.97908	0.97982	0.97913	0.9791	0.97959	0.97940
55	0.98148	0.98068	0.98181	0.9816	0.98231	0.9812	0.98215	0.98256
60	0.98382	0.98432	0.98355	0.9836	0.98479	0.9835	0.98417	0.98348
65	0.98508	0.98613	0.98609	0.9863	0.98637	0.9853	0.98514	0.98643
70	0.98711	0.98791	0.98775	0.9873	0.98723	0.9871	0.98735	0.98691
75	0.9884	0.98867	0.98881	0.9891	0.98909	0.9881	0.98856	0.98870
80	0.99011	0.99020	0.98989	0.9900	0.99034	0.9897	0.98962	0.99038
85	0.99109	0.99126	0.99095	0.9915	0.99117	0.9908	0.99078	0.99130
90	0.99227	0.99220	0.99171	0.9920	0.99154	0.9918	0.99204	0.99241

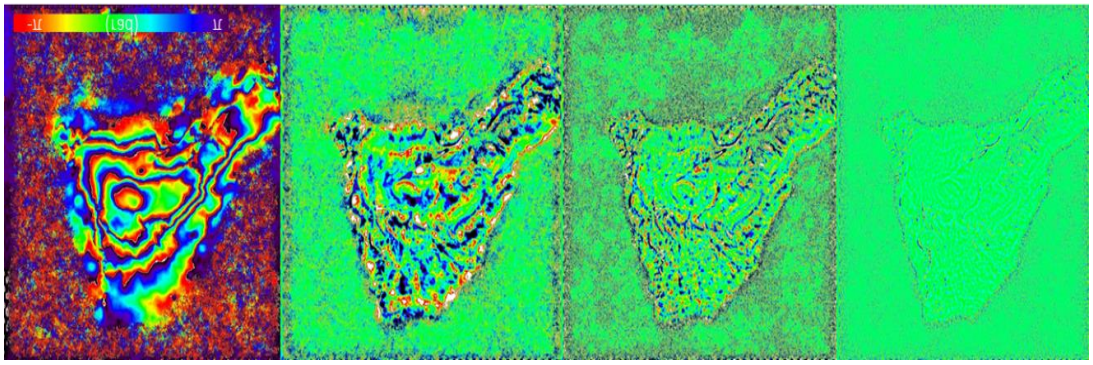

Figure 4.2. Changes in the fringe pattern of the interferogram with respect to the threshold frequency used for the splitting. The images show the residual interferogram with a threshold frequency of 0, 20, 30 and 40 (right to left)

4.2.2. High and low frequency splitting

The main goal of all the interferometric analysis presented in this thesis is to discover the deformation time series and velocity maps of the active areas from the available interferograms quickly and correctly, which is useful for geohazard detection and early warning. In this section, the procedure to detect the active deformation area from interferograms directly without any complex and time-consuming analysis is described. The entire process of this approach can be divided into 4 blocks where the final output is an ADA map as well as an accumulated deformation TS for each point along the satellite LOS direction at each acquisition time.

An interferogram consists of a complex combination of phase information from deformation, atmosphere, noise etc., and it is very difficult to extract only the deformation

information from wrapping phases directly and correctly. According to InSAR principle and frequency spectrum analysis [96], the interferometric phases can be divided into two parts: High Frequency (HF) and Low frequency (LF). In image processing, the low frequencies usually represent the general shape of the image and the high frequencies are needed to sharpen the edges and provide fine detail. Edges and sharp transitions in grey values in an image contribute significantly to high-frequency content of its Fourier transform. Regions of relatively uniform grey values in an image contribute to low-frequency content of its Fourier transform. Hence, an image can be smoothed in the Frequency domain by attenuating the high-frequency content of its Fourier transform. We propose a similar approach here to split the consecutive interferograms into two parts: high and low frequency, with an appropriate filter. The high frequencies are residual phases from the filtering process containing only slow periodical deformations (few mm/yr to several cm/yr), fast local movements (few mm/day), spatially decorrelated noise and residual topographic errors due to the used DEM. The spatially correlated atmospheric phase are the main low frequency components and are worthless for our goal, but there can be a part of deformations phase contained in LF, usually movements with high spatial correlation. In other words, the low frequencies are the changes that take place slowly over the time, such as the atmosphere, in contrast to the high frequencies i.e., those signals undergoing rapid changes over the time such as deformations, noise etc. The advantages of this method over the use of auxiliary data are, there is no wait for an external data source to provide the information to model the atmosphere, there is no addition of unwanted information which can also result in erroneous interpretations in addition to being a fast and easy procedure. Since the systematic errors caused by the DEM or orbits can be corrected with calibration, these errors are considered to be easily resolvable in this analysis. Hence, the simplified phase distribution in an interferogram can be written as:

$$\varphi = \varphi_{defo} + \varphi_{atm} + \varphi_{noise} = \varphi_{high} + \varphi_{low} \tag{4.1}$$

$$\varphi_{high} = \varphi_{noise} + \varphi_{defo\_main} \tag{4.2}$$

$$\varphi_{low} = \varphi - \varphi_{high} = \varphi_{atm} + \varphi_{defo\_residual} \tag{4.3}$$

Where φ_{defo} is the deformation phase, φ_{atm} is atmospheric phase and φ_{noise} is noise phase, $\varphi_{defo_main}$is the main part of the deformation phase, and $\varphi_{defo\_residual}$ represents the residual deformation phase. The signals pertaining to noise belong to the high

frequencies of the frequency spectrum of the image and atmospheric signals are the low frequencies in the spectrum. The deformation signals, even though are concentrated more on the high frequency side of the spectrum in the 6-day interferograms, can also be seen distributed throughout the spectrum and can be extracted part by part with an effective frequency division processing [96, 27].

The SAR signal sensor and processor can use the full synthetic aperture and the complete signal data history in order to produce the highest possible resolution, albeit very speckled, Single Look Complex (SLC) SAR image product. Multiple looks may be generated by averaging over range and/or azimuth resolution cells. An improvement in radiometric resolution using multiple looks, is often accompanied by a degradation in spatial resolution. The goal of the multi-looking process is to obtain an image with approximately squared pixels considering the ground range resolution and the pixel spacing in azimuth. In particular, in order to avoid over or under sampling effects in the geocoded image, it is ideal to generate a multi-looked image corresponding to approximately the same spatial resolution foreseen for the geocoded image product. Depending on the area and nature of the study, it is possible to work with full resolution images or multi-looked images. The redundant networks of interferograms can be generated as a full-resolution (pixel footprint: 4 by 14 m) images or 10 in range by 2 in azimuth (10x2) multi-look (pixel footprint: 40 by 28 m) depending upon the application. The pre-processing images, usually follows a series of typical steps such as extraction and merging of bursts and swaths for the study area, azimuth and range focusing, image co-registration, with a DEM etc. before the interferograms generation. In order to fully exploit the temporal sampling of Sentinel-1 data generate the interferogram network with short spatial-temporal baseline has to be generated as the first step of the process. This process requires an analysis of the minimum temporal baseline to be used to guarantee good quality of deformation detection quality with high coherence. The general scheme of the procedure, shown as a flowchart in Figure 4.3. As mentioned before the approach here is to split the consecutive interferograms in the network into two parts: high frequency (HF) and low frequency (LF). A threshold for each interferogram is adopted from the power spectrum of the respective interferogram where different thresholds are evaluated to achieve the best separation effect. For example, in the Catalonia test site, only the pixels with cut off threshold higher than 40 have been selected as HF by Butterworth band-pass filtering, for the Canary Islands the threshold is 80.

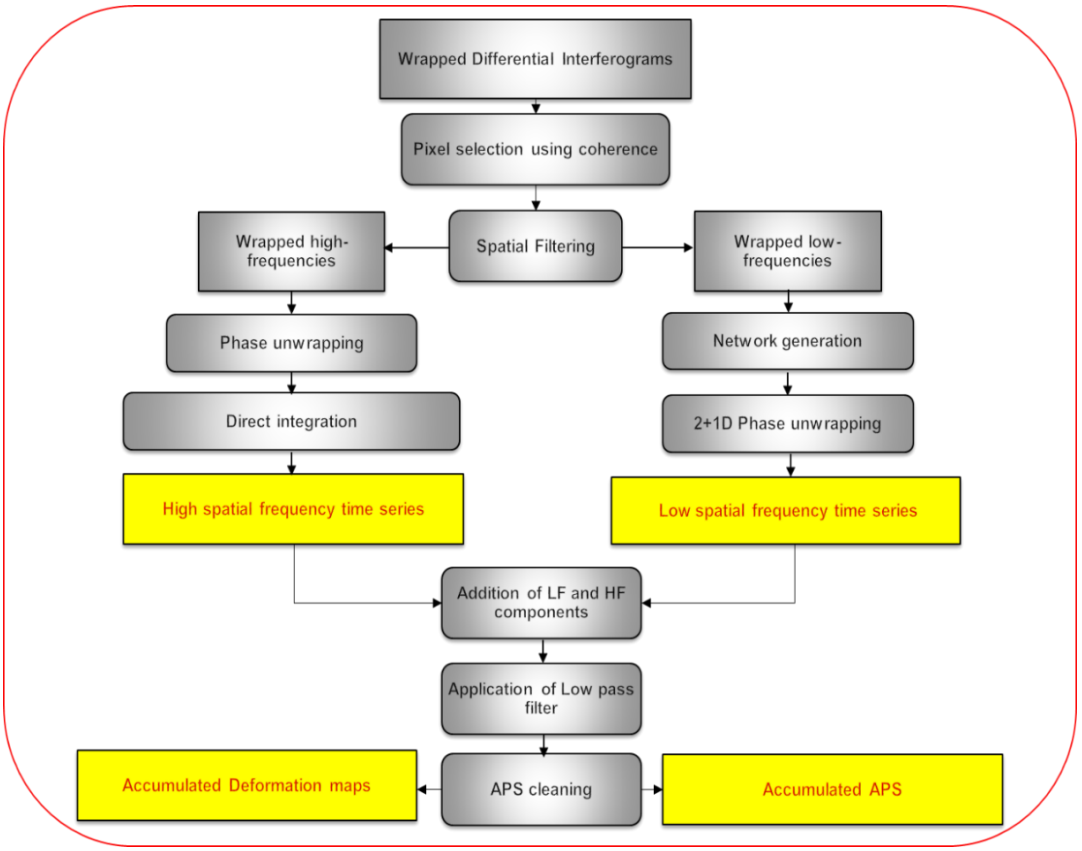

Figure 4.3 Flow chart of the proposed spectrum splitting and filtering approach

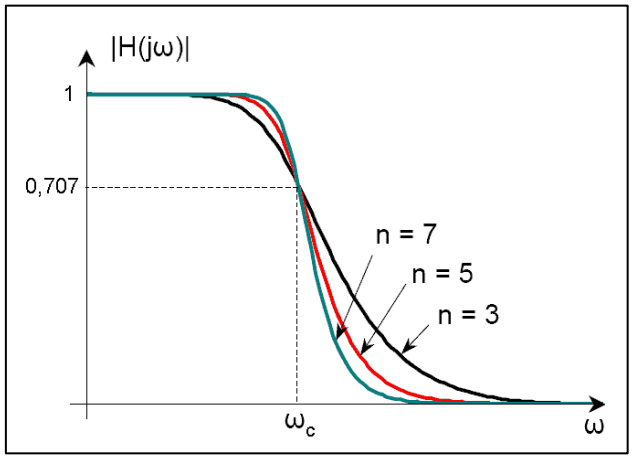

Figure 4.4 Butterworth filter frequency response

The main steps of the process are described below:

1) Pixel selection*:* The first step is the pre-pixel selection. Not all points can be used for obtaining the time series. A variety of methods can be adopted to perform this based on coherence, dispersion of amplitude (DA) etc. The threshold might vary for different sites and the final value seeks a trade-off between sampling density and noise. We select the points that have average coherence above a given threshold. The

average coherence is the average of the coherences of the whole set of interferograms. Those points with coherence smaller than the selected threshold are removed before phase unwrapping. We usually select a low threshold to include the maximum number of points.

2) Splitting using LPF: The Butterworth filter [97] shown in Figure 4.4. is used to separate the signals into high and low frequencies on complex, discrete Fourier transform of the wrapped interferograms, following the equation:

$$|H_a(j\omega)| = \frac{1}{\sqrt{1+\left(\frac{\omega}{\omega_c}\right)^{2N}}} \tag{4.4}$$

Where H_a is the filtered image or pixel, ω is the frequency, ω_c is the cut-off frequency, and *N* is the order. An inverse Fourier transform of the filtered image H_a will produce an output image of the interferogram with only low frequency signals. The LF band phase φ_{low}dominated by the atmospheric phase is separated from the interferogram, and then the HF band phase dominated by the deformation phase is separated from the interferogram by conjugation operation as given in Eq.4.4 and Figure 4.5.The filtering is performed on wrapped interferograms, in order to minimize the errors corresponding to the atmosphere during the phase unwrapping. The time-series of the interferometric phase sequences corresponding to HF and LF are $\varphi_{high}^{k}$and $\varphi_{low}^{k}$where k ϵ (1, 2, 3….N-1)respectively, as shown in Figure 4.6. After HF and LF separation, it is also possible to use additional smoothing filters like Goldstein filter to adaptively denoise the interferogram to remove the residual noise phase $\varphi_{noise}$from HF. In this study, we use the Goldstein filter only in the Catalonia case study.

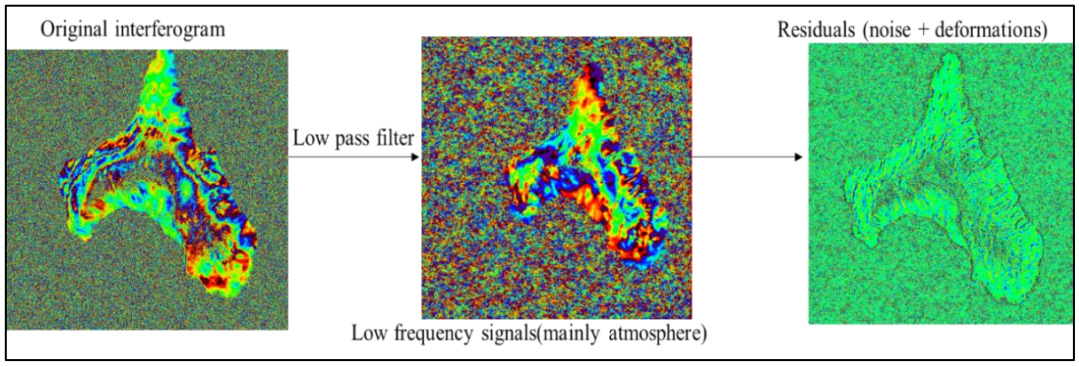

Figure 4.5. Splitting of Fourier transformed interferograms using a Low pass Butterworth filter, resulting in the separation of the phases into spatially correlated low frequency signals which contains the phase contribution of the atmosphere and the residuals composed of phase from noise and deformations.

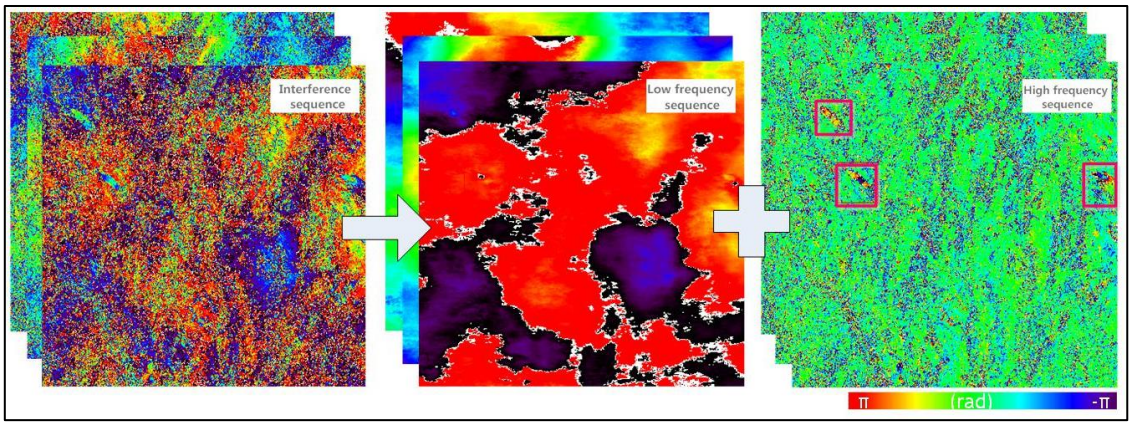

Figure 4.6. High and low frequency band separation time series

3) Phase unwrapping: After HF and LF splitting, the phase unwrapping is performed separately for the low and high frequency signals. We use a simple direct spatial unwrapping algorithm for the HF. Since the low frequency signals of the wrapped interferograms posed more challenging than the high frequency signals, a long-drawn- out procedure of 2+1D phase unwrapping [46] was adopted to reduce the errors and jumps in the unwrapped outputs. A 1D (temporal) iterative least square is performed after the 2D phase unwrapping. The index of redundancy (internal reliability) is used to properly detect the outliers at each iteration. The internal redundancy directly depends on the network (design matrix) and stochastic model (variance-covariance matrix). The iterative LSM identify, in a robust way, the unwrapping errors and correct the corresponding observations which determined that error, this is also possible because the algorithm takes advantage of unwrapping error magnitude (which is a priori known). The resolution is only possible when the network presents a high degree of redundancy.
4) Integration of the HF and LF to form the time series: A pixel wise processing is performed in this step, which analyses over unwrapped interferometric phases with time series. An iterative process, exploiting the Single Value Decomposition (SVD) least squares method and adopting an outlier rejection strategy, builds the matrix used for SVD by so-called residuals associated with observations of unwrapped interferometric phases. This procedure determines the phase values associated with each SAR image, starting from a stack of interferograms. The accumulated phase over time is estimated for each point as follows:

$$\begin{cases} \varphi_i = \varphi_{i-1} + \Delta\varphi_{i(i-1)} & i = 1 \div N \\ \varphi_0 = 0 \end{cases} \tag{4.5}$$

Where φ_i the accumulated phase at the acquisition is time i, and $\Delta\varphi_{i(i-1)}$ is the interferometric phase between the images i and i-1.

5) Atmospheric phase estimation and reduction: Once we have a separate unwrapped accumulated phase of LF and HF, the corresponding interferograms are added back to form whole unwrapped interferograms using Inverse Fourier transforms. Then this stack of interferograms demands the removal of the atmospheric phase. The standard low pass filter is used to remove the atmospheric contribution to the phases φ_i (very low spatial phase variation). The estimation of the atmospheric component of any PSI procedure is based on identification of stable areas in the surroundings of the deformation area as the atmospheric phase component is firstly estimated over the stable areas. Usually, APS estimation requires an input of the temporal evolution of the phases (TEP) estimated with 2+1D phase unwrapping. The estimated APS is removed from the TEP. The remaining phases are then transformed into deformations, obtaining the final TS deformation.

4.3. Results and discussion

4.3.1. Catalonia case study

These results were derived from S1 SLC images over Catalonia, which is an autonomous community of Spain consisting of four provinces: Barcelona, Girona, Lleida, and Tarragona. Catalonia has a marked geographical diversity, considering the relatively small size of its territory. The geography is conditioned by the Mediterranean coast, with 580 kilometres (360 miles) of coastline, and large relief units of the Pyrenees to the north.

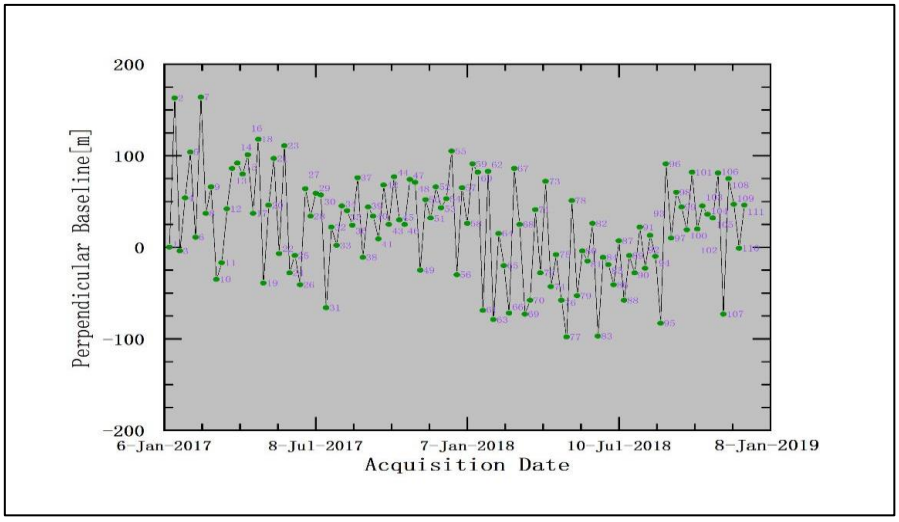

Figure 4.7 The temporal baseline plot of the processed interferograms.

The Catalan territory can be divided into three main geomorphologic units:

1) The Pyrenees: mountainous formation that connects the Iberian Peninsula with the European continental territory, and located in the north of Catalonia;
2) The Catalan Coastal Mountain ranges or the Catalan Mediterranean System: an alternating elevations and planes parallel to the Mediterranean coast.
3) The Catalan Central Depression: structural unit, which forms the eastern sector of the Valley of the Ebro.

The study area Catalonia is covered by a single S1 frame. In particular, two swaths and 7 bursts have been processed for monitoring measurement. The used SAR dataset consists of 111 S1 Wide Swath images spanning around two years period, with the first acquisition time in January 2017 and last one in January 2019. All the images from twin S1 satellites have been collected for measurement in this study, and the minimum temporal gap is 6 days, while the maximum is 12 days which is defined by the image availability. Figure 4.7 shows all the acquisition times of the processed images and perpendicular baselines of interferograms. As explained in the introduction, the aim of this study is to generate the TS deformation maps for Catalonia because the deformation procedure is quite useful and important for the geohazard analysis. One interferometric network was designed with the minimal temporal baseline (6 days or 12 days due to the data downloading failure) to guarantee the coherences between these pairs shown in the Figure 4.7 which is the key point for interferogram generation with good quality.

The monitoring results of this study covers an approximate area of 19,000 km^2. 111 images have been processed by proposed method, with most part of interferograms affected by serious decorrelation and noise with the mean coherence less than 0.25 (the threshold of PS candidates for PSI approach), due to the vegetation coverage and topography. However, the active deformation time series with excellent coverage could be generated using the proposed methodology, even for the active areas with large-scale displacement in short time, such as mines. To analyse these deformation results, some examples are illustrated below. Compared with the results from traditional PSI techniques, more than 5 million coherent points could be extracted for deformation monitoring with greater coverage which are valuable for civil risk evaluation and management. The accumulated deformation maps from some areas are shown along with a sample of the retrieved temporal deformation of a selected point among them. Three main deformation mechanisms have been identified Catalonia:

1) Underground mining activities are detected using the proposed method in intense ADA (towns of Súria, Cardona and Sallent among others) with serious settlements (Figure 4.10 and 4.11).
2) Heavy surface load in the Barcelona Port and Airport whose subsidence has already been more than 10cm from January 2017 to January 2019. However, the dam nearby estuary of the EI LIobregat River has raised up more than 12cm in Figure 4.12 and 4.13.
3) Intense water extraction is well recognized in some urban areas, most part of Igualada city is very stable, but there is a few subsidence in the downtown of this city might be caused by water extraction or urban construction in Figures 4.14 and 4.15.

Figure 4.8 Footprint of the processed amplitude image and area of interest. The area is covered by 2 sub-swaths and 7 bursts

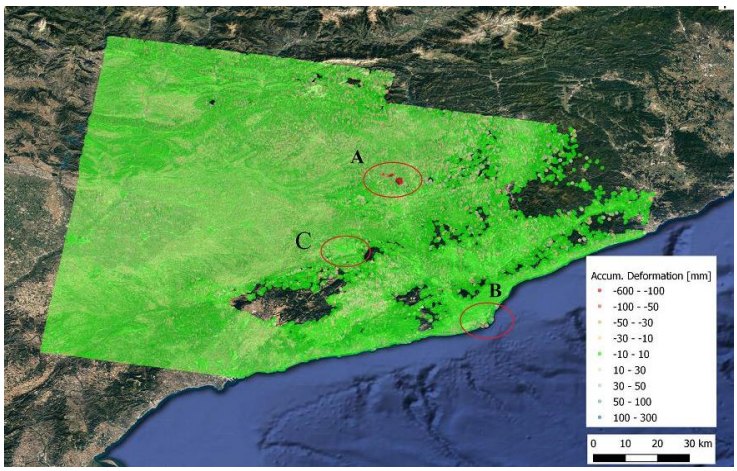

Figure 4.9 accumulated deformation map of study area using the splitting method. Three examples of deformation results are given below (red circle).

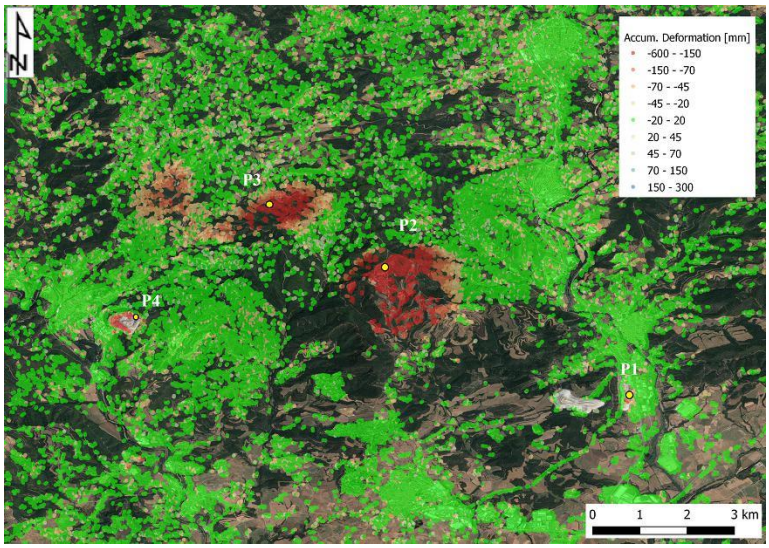

Figure 4.10 Active deformation map of area A revealing a surface subsidence (over – 60 cm) caused by mining activities during observation period.

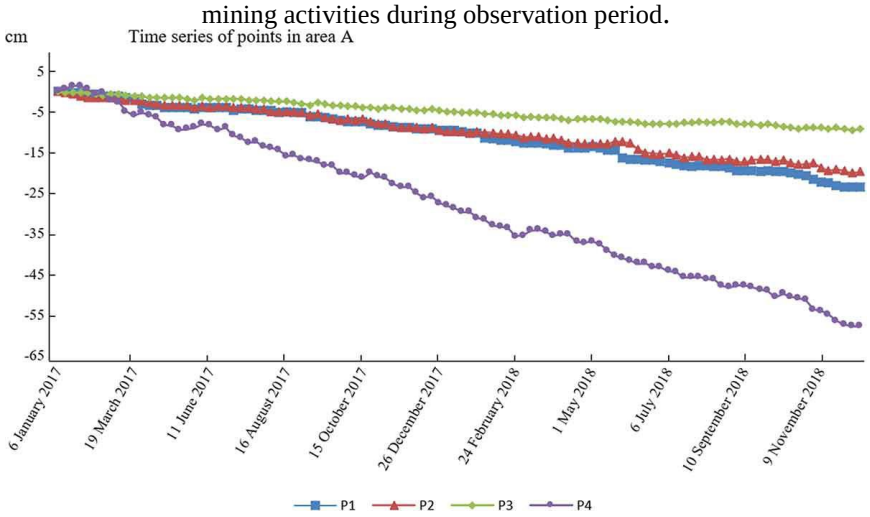

Figure 4.11 Four points of deformation results with time series located in the area A shown in Figure 4.9

Figure 4.12 Active deformation map of area B (Barcelona Ports). P1 and P2 have notable settlement (between –2 and –6 cm) due to surface loading during the observation period, P3 has a lifting deformation (over 5 cm) caused by the sedimentation.

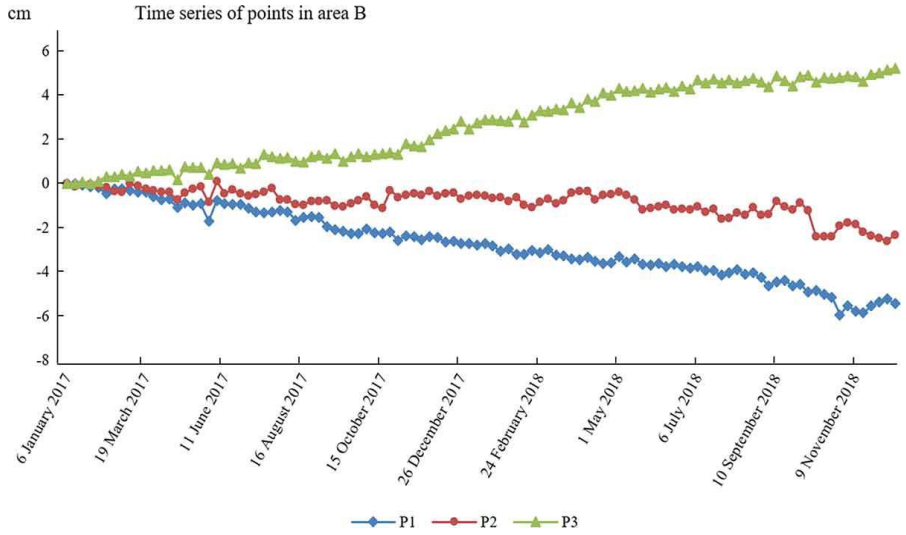

Figure 4.13 Three points of deformation results with time series located in the area B shown in Figure 4.9.

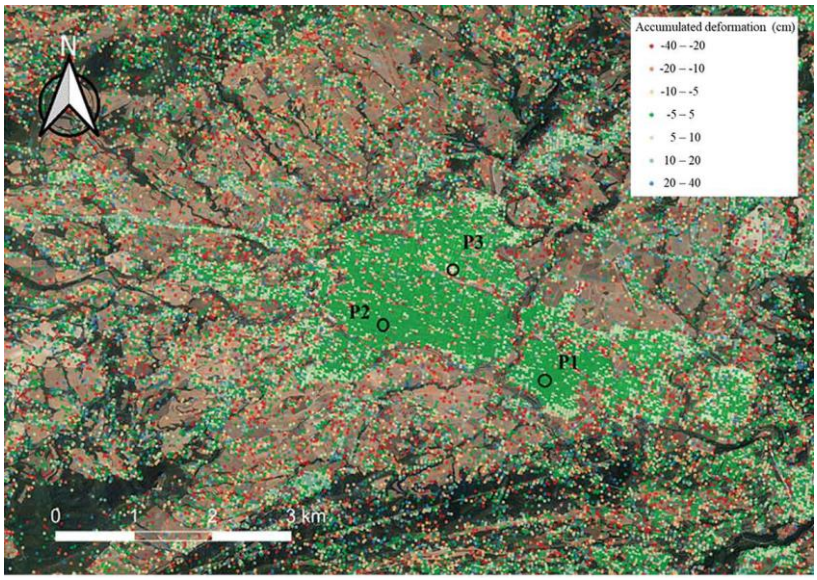

Figure 4.14 Active deformation map of area C (Igualada). P1 and P2 are all very stable during the observation period, but P3 has a settlement (–13 cm) caused by the water extraction.

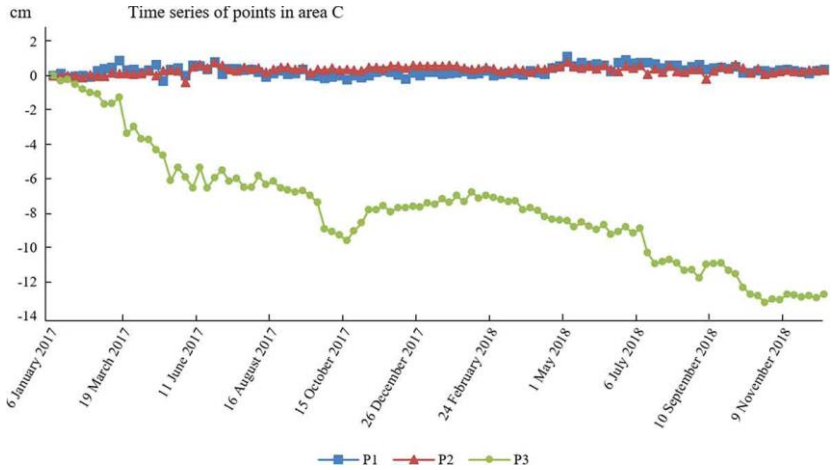

Figure 4.15 Three points of deformation results with time series located in the area C shown in Figure 4.9

4.3.2. Canary Islands case study

El Hierro is the south-westernmost island of the Canaryian archipelago (Spain), located in the Atlantic Ocean off the coast of Africa. El Hierro Island is volcanic and sharply mountainous, hence is a highly prone area to landslides and slope failures. With an area of 268 km^2 and a population of 10.679 inhabitants (Instituto Nacional de Estadística (INE) 2018), the island has three municipalities, Frontera, El Pinar and Valverde, where the capital is located. The island is the emergent summit of a volcanic shield, which rises from a depth of 3700-4000 m deformation is one of the parameters that can reflect a change in the volcanic system, which can potentially lead to an eruption. Hence, the goal was to rapidly and semi-automatically generate a product to be easily exploited in the geohazard management by the Civil Protections Authorities and the Geological Surveys [95, 98].

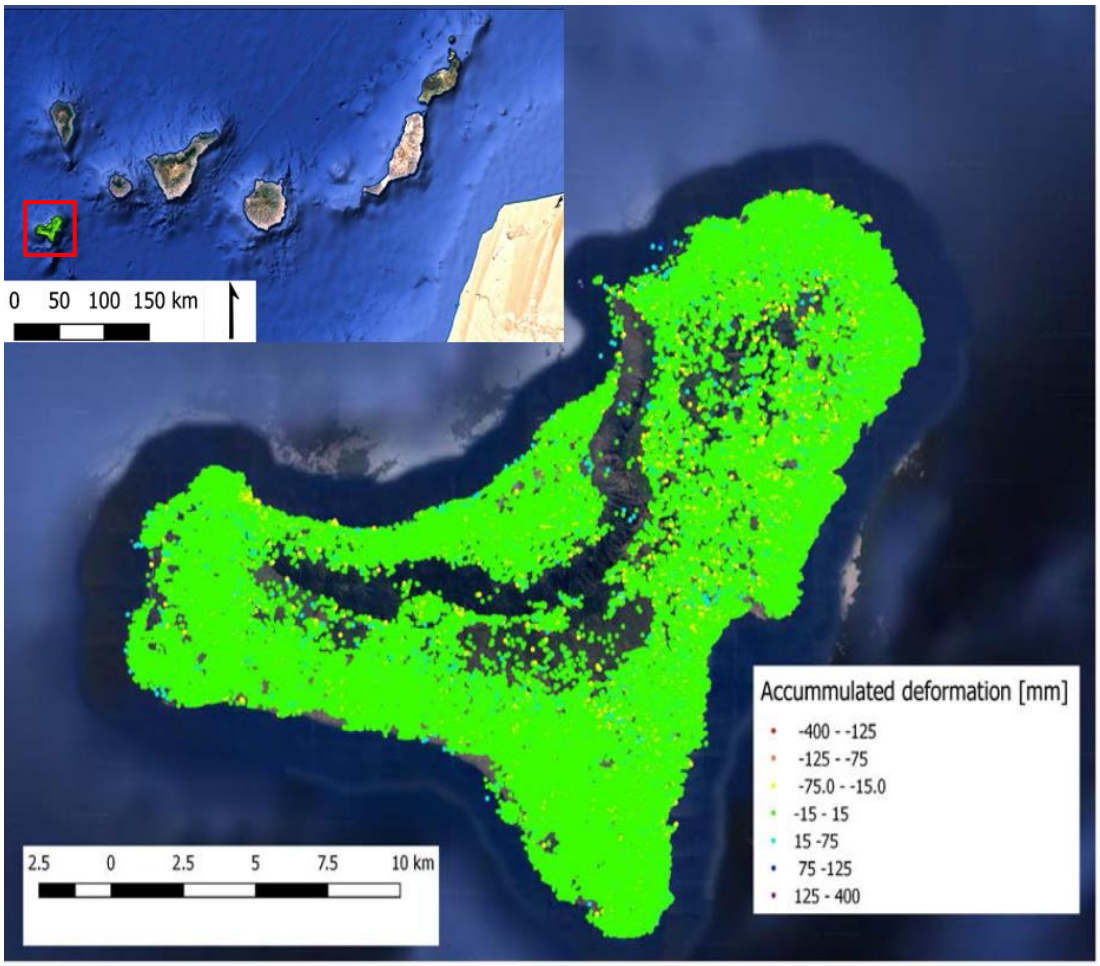

Figure 4.16 Deformation activity map of El Hierro representing the accumulated displacement in the monitored period.

The three measured islands, La Palma, Hierro and Tenerife, are covered by a single Sentinel-1 frame. The dataset consisted of 83 Sentinel-1 Wide Swath, covering one year and 8-month period, starting in January 2017 and ending in August 2018. Due to critical atmospheric components and noise, some images were discarded for different islands. In particular, the dataset of El Hierro island was reduced to 74 images covering the period from May 2017 to August 2018. The selected resolution has been the multi-look 2x10 that corresponds to a footprint of approximately 28x36 m. This resolution is a compromise between density of measurable points, due to coherence, and resolution high enough to detect small deformation phenomena. The displacement maps are directly derived from Sentinel-1 (S-1) data by means of A-DInSAR analysis, which provides qualitative information. The analysis of these maps demands user expertise and must be done with the support of complementary data like GPS or other geodetic techniques.

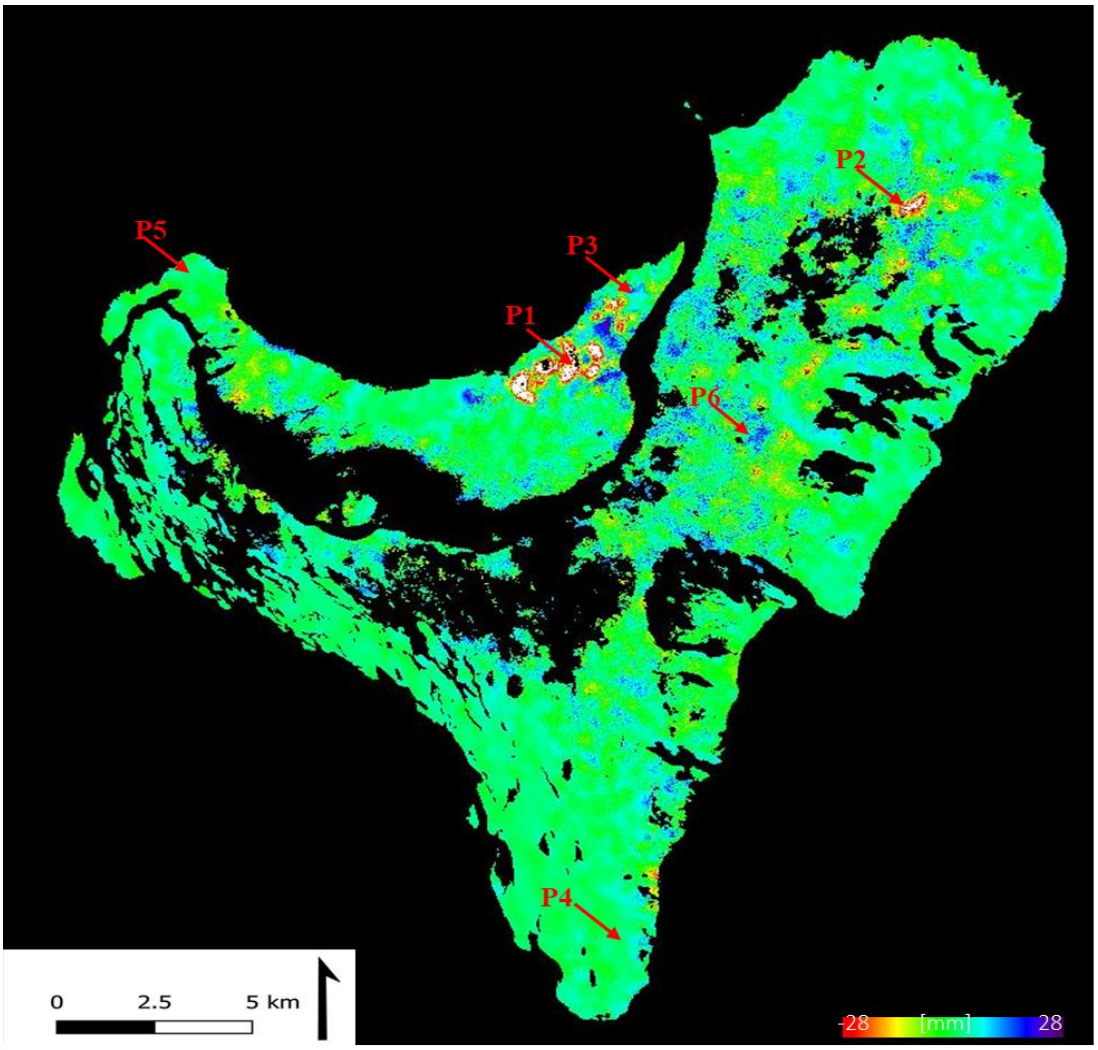

Figure 4.17 Accumulated displacement map of El Hierro Island and examples of time series obtained with the DI approach. The time-series of two sets of points P1, P2, P3, P4, P5, P6 located in the seemingly unstable and stable areas of the island respectively are shown in figure 4.18.

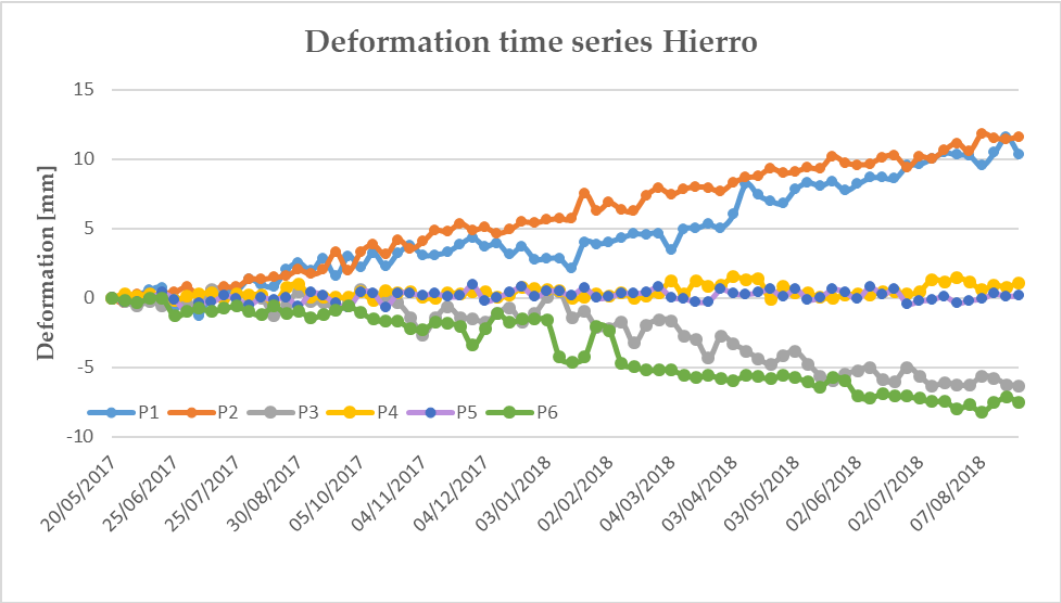

Figure 4.18 Examples of deformation time series of El Hierro P1, P2, P3, P4, P5, P6 as shown in figure 4.17

The deformation maps were produced and analysed in radar geometry during the processing. There were not detected significant displacement signals in the DIMs during the monitored period. The results were compared with those obtained by using Persistent Scatterer (PS) technique, a consolidated and reliable technique. The comparison was performed on a set of common points. The comparison results confirmed the reliability of the approach at least for this set of points. For example, the standard deviation of the accumulated displacement differences is ≅8mm and the average 1 mm. However, there were areas without PS, i.e., not included in the comparison, with uplift deformation trends where no movements were expected and difficult to be interpreted from a geological point of view. The points with mean coherence higher than 0.1were used for the splitting approach. The sampling density achieved in the first instance was not deemed enough and, as a measure to improve the density of points, a spatial averaging within homogeneous coherent pixels of single look images were performed to form multi-looked observations. Most of the S-1 A-DInSAR processing approaches makes use of multi-looked images to reduce noise, but this averaging seems to be introducing a variant systematic signal, which shows no characteristics of stochastic noise, among the multi-looked interferograms, mimicking deformation signal patterns (Figure 4.18 P4). This signal, which in this case is present in highly coherent points, is not filtered out during pixel selection and can be wrongly interpreted as deformation patterns, especially when prior knowledge about the area under observation is unavailable. The complex geophysical characteristics of the Island, such as the coasts and the presence of high cliffs

has significant influence in the signals. This signal is named ‘fading signals’ because of the reason that the signal perishes with the increment in temporal baseline [52]. The explanation to these trends is the integration in time of a systematic error of the filtering in areas with low coherence. This problem is still not solved in a general way.

Once we have the displacement maps called DIM in the CTTC- geomatics framework of A-DInSAR processing chain of interferograms for deformation monitoring, it can be further developed into a DAM (deformations area) map consisting the estimated velocity in mm/yr and the deformation time series (TS) for a set of selected points. It is relatively easy to be interpreted. Finally, the processing chain also produces the ADA (active deformation area) map, which is derived by a semi-automatic extraction of the most significant detected active deformation areas. It is a very simplified map that points the attention on the areas affected by displacements and provides key information about its movements [26, 99]. An example of ADA map of El Hierro is given below, and the discussion of the ADA extraction procedure is beyond the scope of this thesis. The number of measured points is 96196. The standard deviation of the velocity is 5.6 mm/yr and the moving threshold has been set as 11.2 mm/yr. (i.e., 2σ). The reason of these high thresholds is that the monitored period is still short. It is expected to have a significant improvement with longer periods.

However, for the Canary Island site, we exploited the high coherence at a relatively long temporal baselines to solve it. The used approach is: (i) select an interferogram with high coherence and at least one-year temporal baseline; (ii) split it to get the high frequency component. (iii) unwrap it; (iv) compare the result with the DAM map covering the same period; (iv) remove the areas with absolute differences bigger than 8 mm. Figure 4.19 shows the obtained DAM in El Hierro Island after applying the post-processing correction. It is worth noting that this solution is not applicable at every place. It is based in the coherence stability of the Canary Islands at relatively long temporal baselines.

The main challenge is to generate rapidly and semi-automatically a product to be easily exploited in the geohazard management by the Civil Protections and the Geological Surveys [100]. The main advantage of the proposed method is the possibility of semi-automatically generating active deformation maps with TS to reveal the subsidence procedure for wide areas and break the maximum deformation detection ability of InSAR approach based on S1 datasets. The quality of the obtained results is good enough in this test site area. However, there are some issues to be solved in order to improve the

coverage with a reasonable reliability. We have focused most of the tests on Hierro Island given that it was the most interesting island for civil protection. The main goal was to tune the approach. For this reason, we have worked with a short dataset easy to be reprocessed. Apart from the theoretical drawback such as acquisition geometry and displacement limitation, there are two other aspects that spatially influence the possibility of detecting movements: the frequency splitting process and the lack of noisy phase elimination.

Similarly, deformation activity maps were derived for Tenerife and La Palma using the same splitting procedure. The colours represent the accumulated deformation during the monitored period. The north east part of the island does not have points because it was not included in the acquisition frame. A total of 661544 points have been measured. The standard deviation of the velocity is 4.1 mm/yr. The moving threshold, i.e., the minimum velocity of a point to be considered a moving point, has been set as 8.2 mm/yr (i.e., 2σ). This threshold is relatively high. However, a significant decrease is expected with longer monitoring periods. For a better perspective and understanding a comparison was also made in parameters such as density of points and reduction in phase unwrapping jumps between the standard PSIG chain and the splitting approach. As seen in figure 4.20, the density of the points has significantly increased (approximately 18%) and there is visible reduction in phase unwrapping errors.

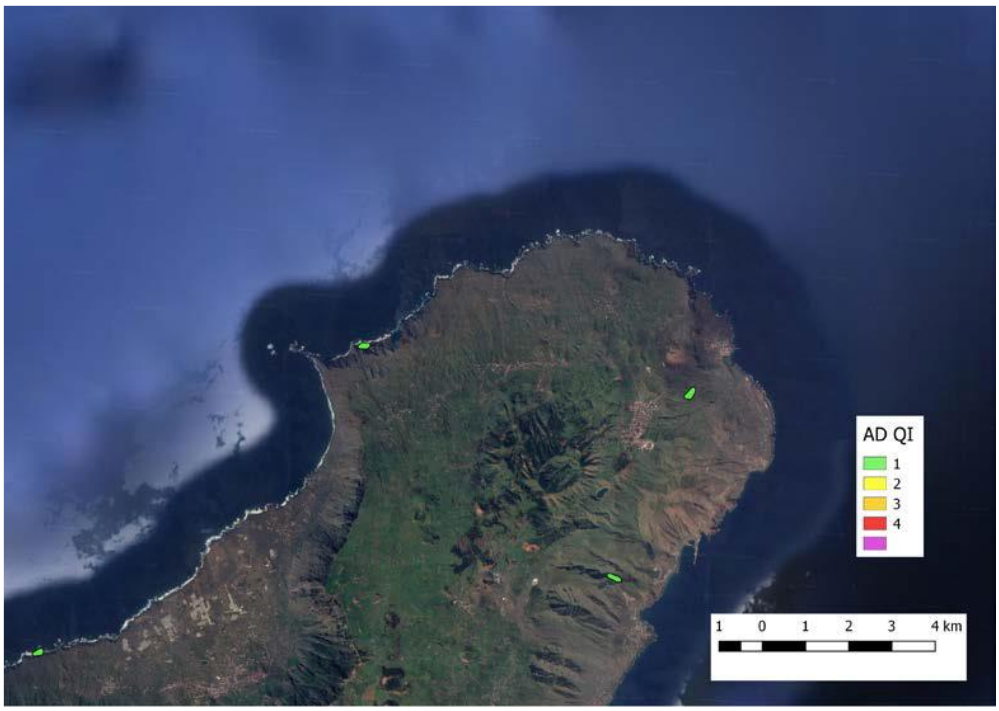

Figure 4.19 ADA map of el Hierro.

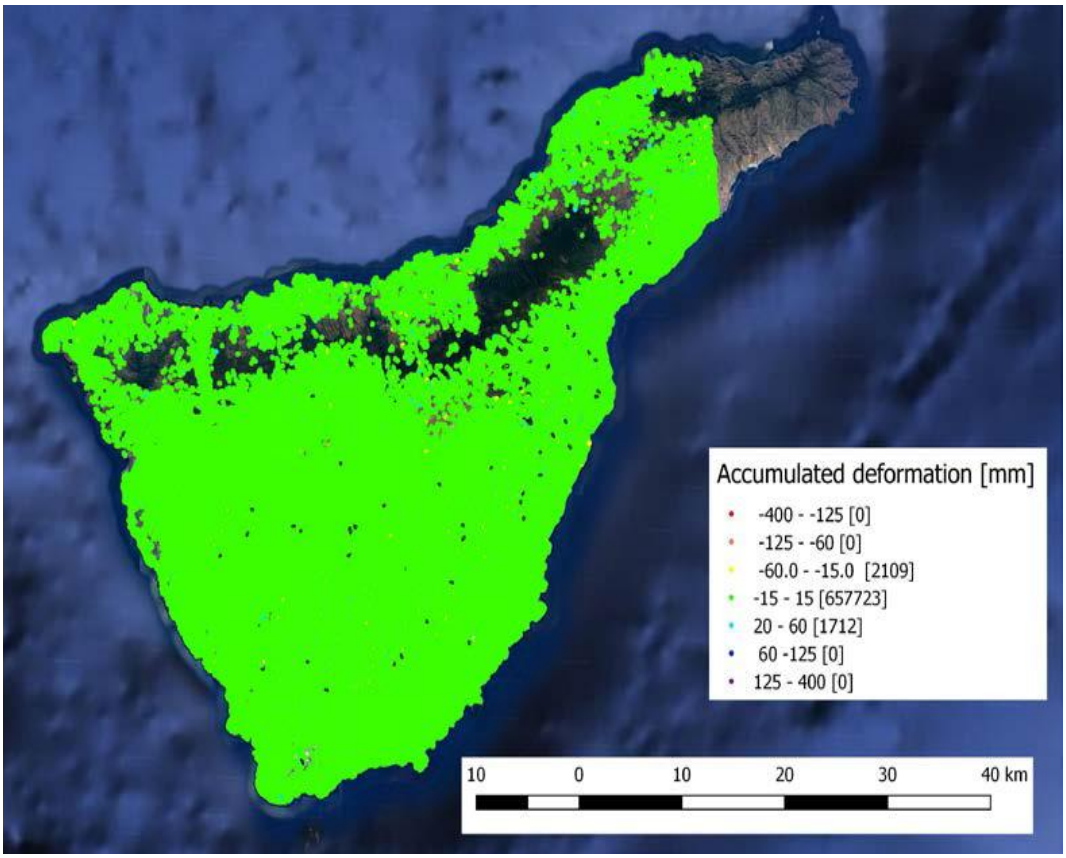

Figure 4.20 DAM map of Tenerife representing the accumulated displacement in the monitored period

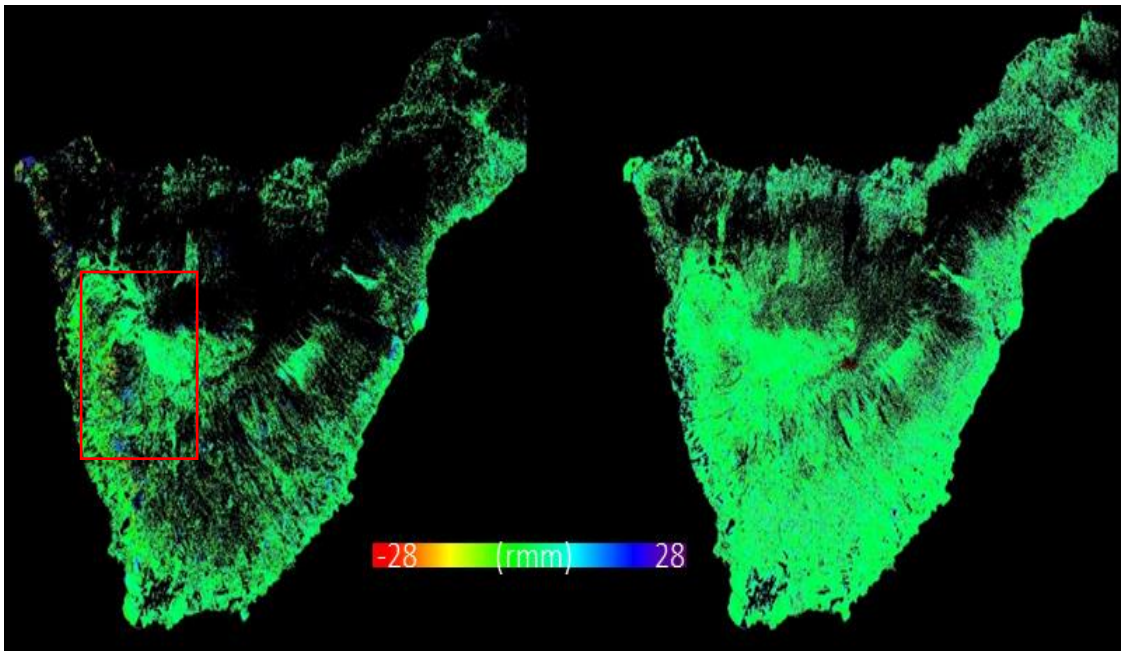

Figure 4.21 The accumulated deformation in Tenerife using the splitting (right) and the standard PSIG chain (left). It shows a significant improvement in the spatial coverage of PSs and reduction in phase unwrapping errors (red box).

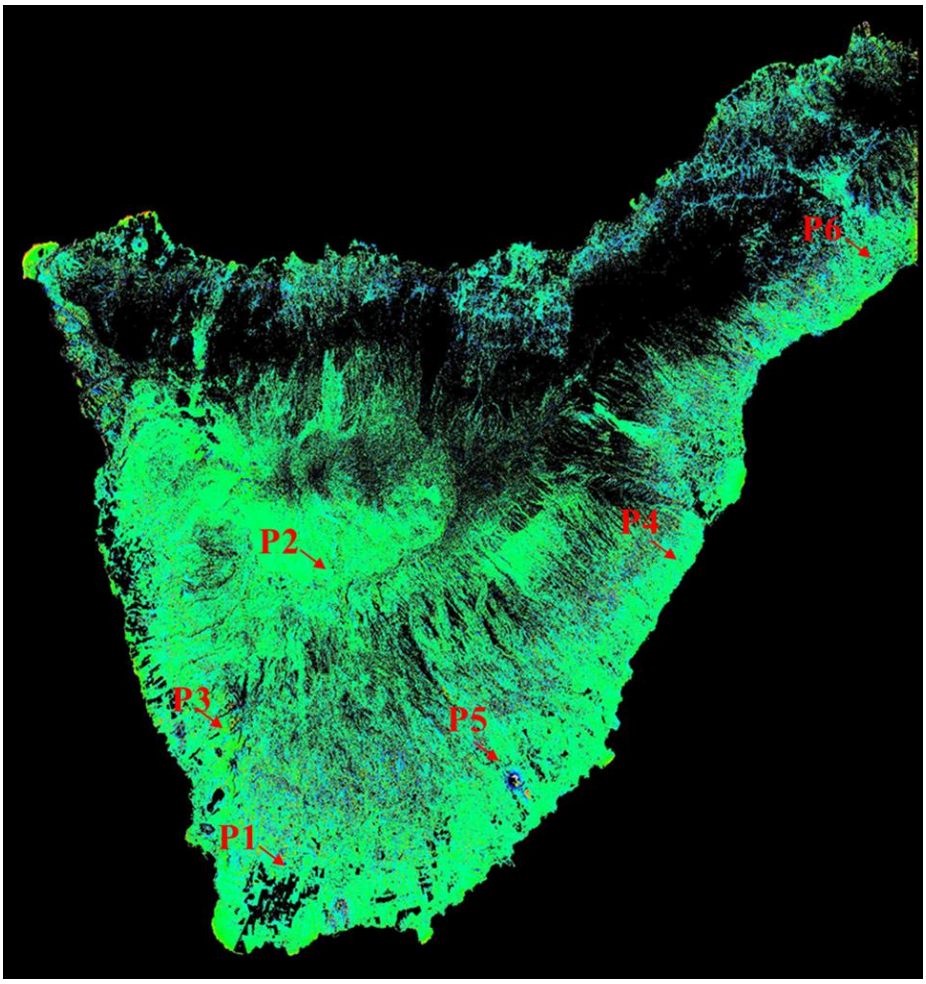

Figure 4.22 Accumulated displacement map of Tenerife Island and examples of time series obtained with the DI approach. The time-series of two sets of points P1, P2, P3, P4, P5, P6 located in the seemingly unstable and stable areas of the island respectively are shown in figure 4.23.

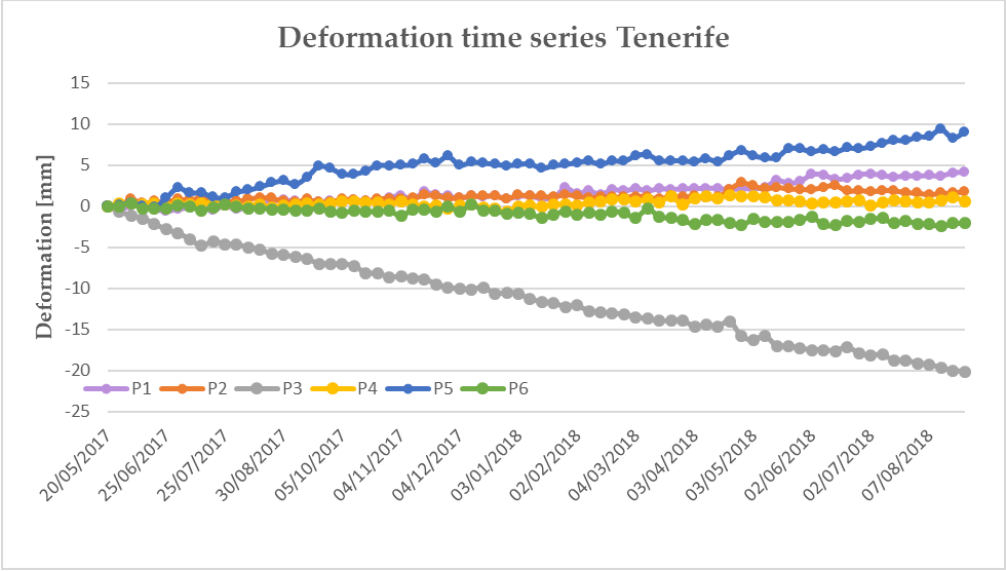

Figure 4.23 Examples of deformation time series of El Hierro P1, P2, P3, P4, P5, P6 as shown in figure 4.22

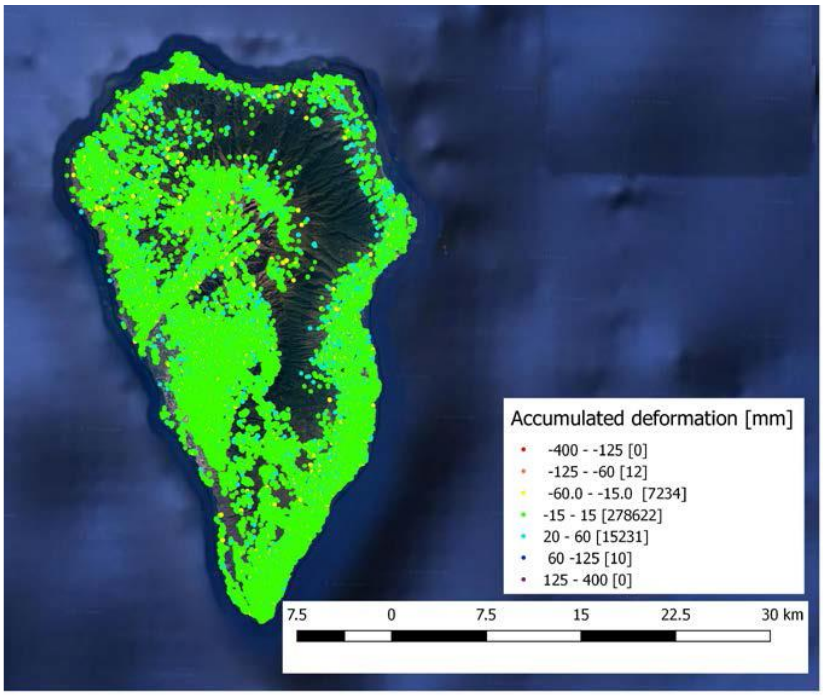

Figure 4.24 DAM map of La Palma representing the accumulated displacement in the monitored period

As a general remark, the proposed approach seems to work and provides good results. However, as commented above, there are still some aspects to be solved to make it replicable in different areas. Therefore, additional experiments and applications are required to verify the feasibility of this methodology. It also has to be noted that there have not been any critical displacements identified during the monitored period. It is worthy to mention that the accuracy of any approach we propose cannot be concluded without ground truth validation. But the main problem with the validation of the results were unavailability of ground data. The future scope of the study can include validation with ground data. One of the goals to be addressed in this thesis is to develop simple and fast near real time methods to generate deformation maps. In that context the splitting approach provides very useful results for expert users to detect hot-spots susceptible to represent a potential risk, not only high magnitude deformation. It would be useful to see this method as a rapid tool to monitor ground displacements with high point density rather than an accurate geodetic approach. We are proposing a ground displacement mapping tool.

Chapter 5

Data driven approaches using short temporal baselines

5.1. Introduction

This chapter focuses on two additional methods using the interferograms itself to further exploit the Sentinel-1 SAR data for deformation monitoring. Both methods discussed in this chapter use a network of interferograms with short temporal baselines. The approaches provide very useful results for expert users to also detect hot-spots susceptible to a potential risk, in addition to high magnitude deformations. Regarding the innovative aspect, we are showing the potentials on the use of such a simple approach with Sentinel-1 data. These approaches are helpful especially when there is a deformation area of relatively small surface, which is surrounded by stable areas.

In this section we describe three case studies where the proposed methodologies are applied for the semi-automatic identification and pre-screening of the deformation processes. Firstly, a successful case of application of the DI: a region located in the north of Chile, entailing two open pit mines. Secondly, a less favourable case of DI but successful for PSIG-STB, the Hierro Island test site. Finally, an example of the Barcelona metropolitan area where the results of PSIG-STB have been used operatively to monitor different infrastructures. The areas are choosen as such to demonstrate the effectiveness and limitations of the 2 approaches. Mining fields are high risk areas with very high deformations and it demand a fast near real time deformation monitoring system, and DI serves that purpose effectively. Then as an example for an urban area to demonstrate the approach we selected Barcelona. El Hierro presented an interesting complex topography to test the approaches.

5.2. Direct integration approach

The first approach which we call the Direct integration (DI) is a fast and unsupervised approach to map and monitor active areas in remote and natural environments. This approach provides a rapid and simple solution to screen wide areas and to map and analyze the evolution of relatively fast and local movements. Compared to standard A-DInSAR approaches, it provides a very high sampling density also in areas where it is not

Chapter 5 is published as Krishnakumar, V., Qiu, Z., Monserrat, O., Barra, A., López-Vinielles, J., Reyes-Carmona, C., ... & Gili, J. A. (2021). Sentinel-1 A-DInSAR Approaches to Map and Monitor Ground Displacements. *Remote Sensing*, *13*(6), 1120.

common to have measures. The idea of the DI approach is taking advantage of the high coherence from the short temporal baseline interferograms provided by S-1.

The DI approach, illustrated in figure 5.1, uses a stack of interferograms with a temporal baseline of the shortest period available, ideally 6 days, to easily retrieve a terrain deformation map over a set of PSs containing the information of the estimated annual velocity and the displacement time series. Thus, the input data consist of a set of N images and the corresponding N-1 interferograms calculated by using consecutive images. The DI approach has four main steps:

1) Pixel selection and phase unwrapping: We select the points that have average coherence above a given threshold. The average coherence is the average of the coherences of the whole set of interferograms. Those points with coherence smaller than the selected threshold are removed before phase unwrapping. We usually select a low threshold to include maximum number of points. Then these selected pixels of all the N-1 interferograms undergo phase unwrapping, which is performed using the Minimum Cost Flow (MCF) method described in [60, 101].
2) Direct integration of the phases: the accumulated phase over time is estimated for each point as follows:

$$\begin{cases} \varphi_i = \varphi_{i-1} + \Delta\varphi_{i(i-1)} & i = 1 \div N \\ \varphi_0 = 0 \end{cases} \tag{5.1}$$

   Where φ_i is the accumulated phase at the acquisition time i, and $\Delta\varphi_{i(i-1)}$ is the interferometric phase between the images i and i-1.
3) Atmospheric phase screen (APS) filtering: in this step, the Butterworth filter (a low-pass filter) is used to remove the atmospheric contribution to the phases φ_i (very low spatial phase variation). A temporal filter is then applied to separate the APS signal from the temporally correlated components, usually associated to terrain deformations.
4) Phase to displacement transformation and geocoding: the accumulated phase of each measured point is transformed into displacement as shown in Eq.2.6.

The final step in the geocoding where the corresponding ground coordinates for each pixel are found. This approach is not supervised and does not provide quality estimators. As explained later in this document, this method is not robust against the so-called fading

effects. However, it provides quantitative measurements that can be helpful to decide to apply more reliable approaches.

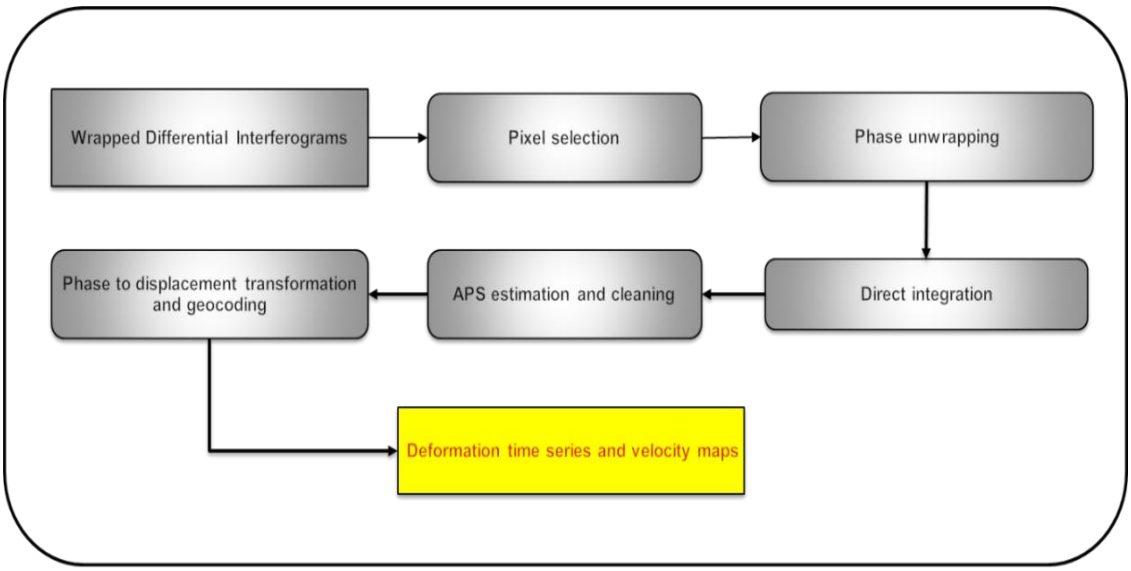

Figure 5.1 DI approach

5.2.1. North Chile region

The underground mining of mineral and ore deposits is widespread across the world. One of the side effects of mineral extraction is the occurrence of ground movements. These movements might be caused by changes in the distribution of load on the hard ground beneath or by water extraction from the aquifers. The monitoring of ground displacements is currently most often carried out with the use of traditional surveying methods, mainly precise levelling. Due to limitations such as spatial restrictions and high costs posed by classical measurement methods, DInSAR has become a very effective solution for the observation of ground movements in mining areas.

This first test site is a positive case of application of the DI approach. It is a good example to show how we can obtain fast and unsupervised accumulated displacement maps over wide regions to map and understand active areas in remote and natural environments. It is applied along a river basin, located in the central north of Chile (longitude -77.33° and latitude -27.35°). Figure 5.2 shows the accumulated deformation along the period ranging from October 2014 to March 2019, in ascending orbit. The number of processed images and interferograms is 81 and 80, respectively. The total number of points is 2 374 445. The time of processing is around 370 minutes with an Intel Core I5-6600 CPU @ 3.30 GHz and 32 GB of RAM. The processing is performed pixel-wise without parallelization.

Thus, the time could be reduced drastically. At a first glance, it is easy to observe the high coverage of the obtained results. The accumulated deformation map resulted in a standard deviation (σ) of 5 mm. We have used two times the σ value as a stability threshold (at 10 mm). With this threshold, the 7% of the points are considered moving points.

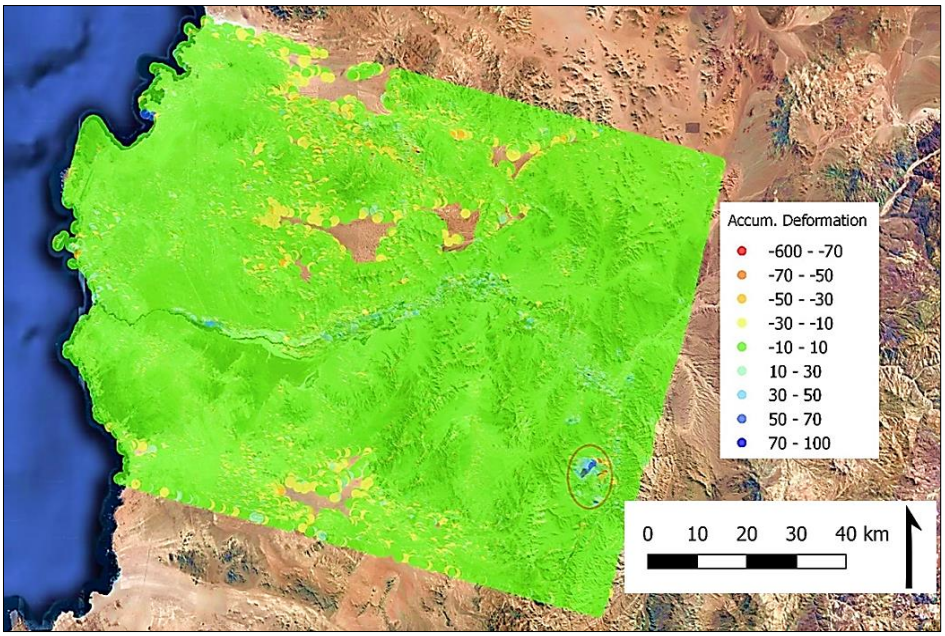

Figure 5.2 Accumulated deformation at the Chile river basin during the period 2015-2020. The red ellipse bounds the area shown in Figure 5.3.

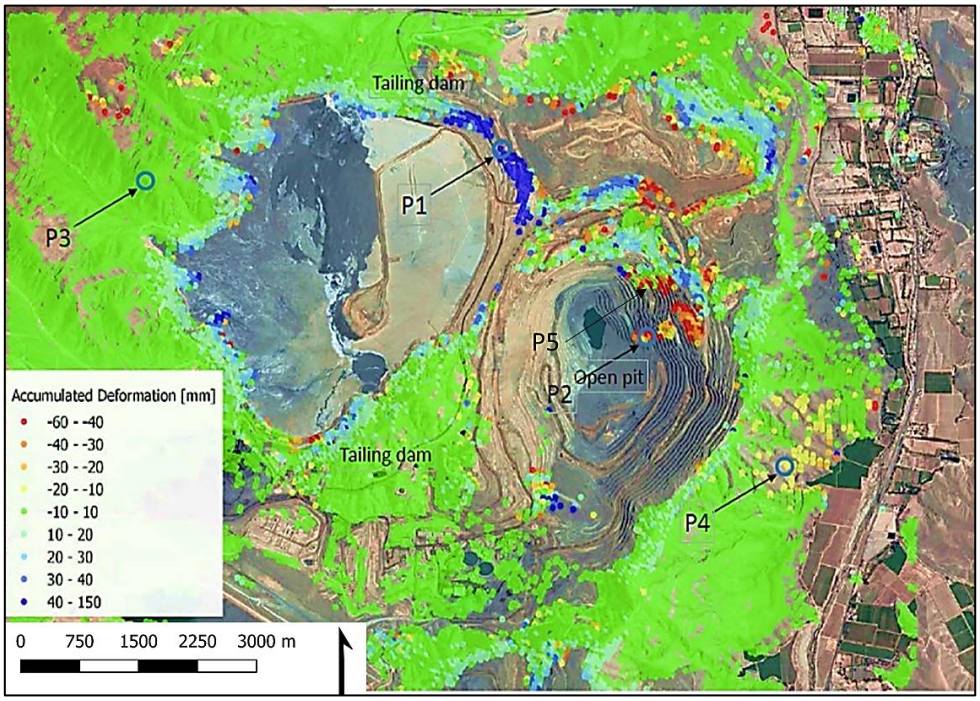

Figure 5.3 Copper mining pits displaying deformation- example 1. The accumulated displacement time-series of the points P1, P2, P3, P4 and P5 are shown in figure 5.4.

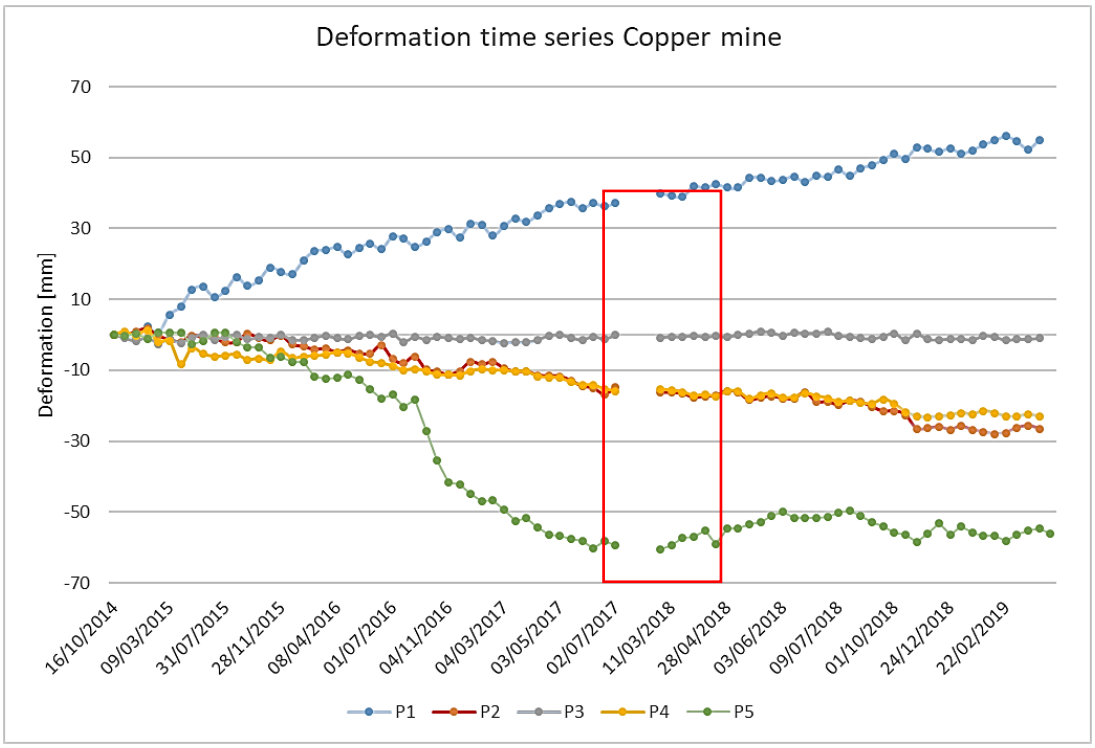

Figure 5.4 Deformation time series of North Chile open pit mine –example 1 of points P1, P2, P3, P4 and P5 shown in figure 5.3

Figure 5.3shows an interesting area affected by displacements, with the corresponding deformation time series (Figure 5.4) of four selected points: one stable (P3) and three unstable (P1, P2 and P4). Movements towards the satellite are shown in blue (positive values) while movements away from the satellite are shown in red (negative values). In this particular case, the detected movements are caused by different mining activities. The displacements shown by P2 and P4 are related to slope instability areas along the open-pit slopes resulting from excavation and the mining exploitation itself. The maximum measured displacements are around -60 mm/year (P2 area) and -30 mm/year (P4 area). Another interesting movement is the upheaval of the tailing dam (P1 area) where byproducts of the mining operations are stored and accumulated (figure 5.3). The accumulated displacement raises in an average of 55 mm. All of the times series displayed in figure 5.4 show almost regular trends despite having a discontinuity in the time-series (bounded by a rectangle, indicating the period where images were not available). However, because of this gap, the values of displacement can be underestimated due to phase unwrapping errors. The DI method does not have any quality estimator. It is worth noting that, despite these potential errors, the target of the analysis is fulfilled since it provides enough information to detect active areas.

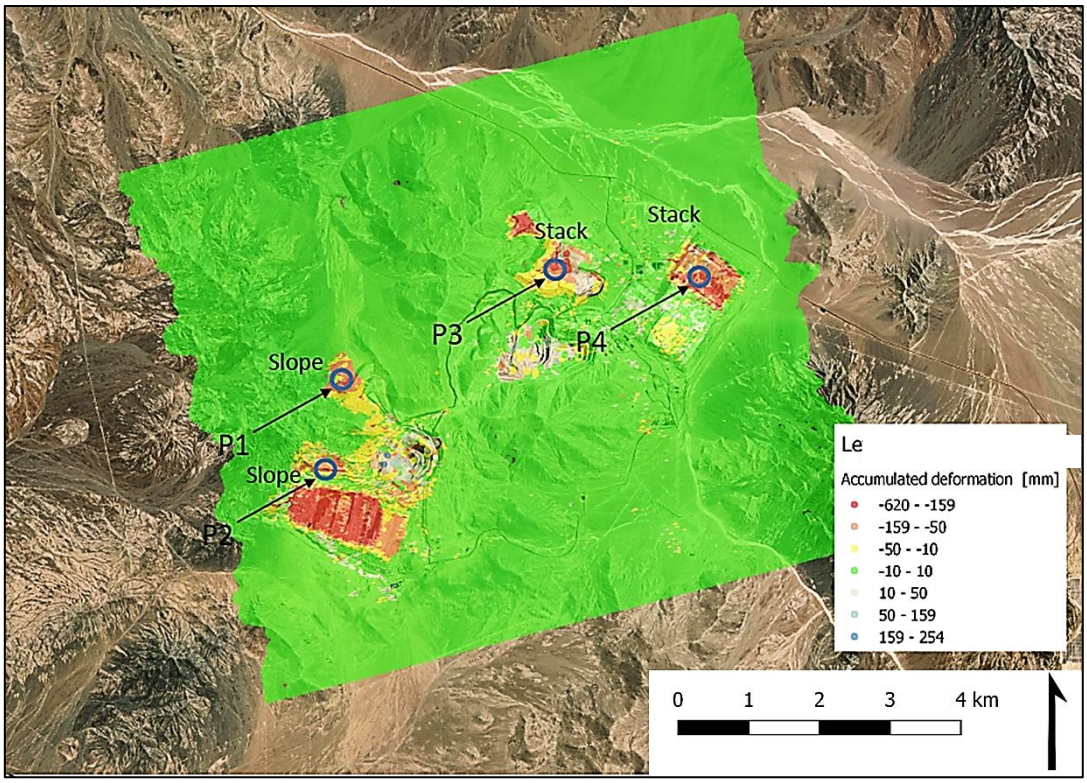

Figure 5.5 Copper mining pits displaying deformation-example 2. The accumulated displacement time-series of the points P1, P2, P3 and P4 are shown in figure 5.6.

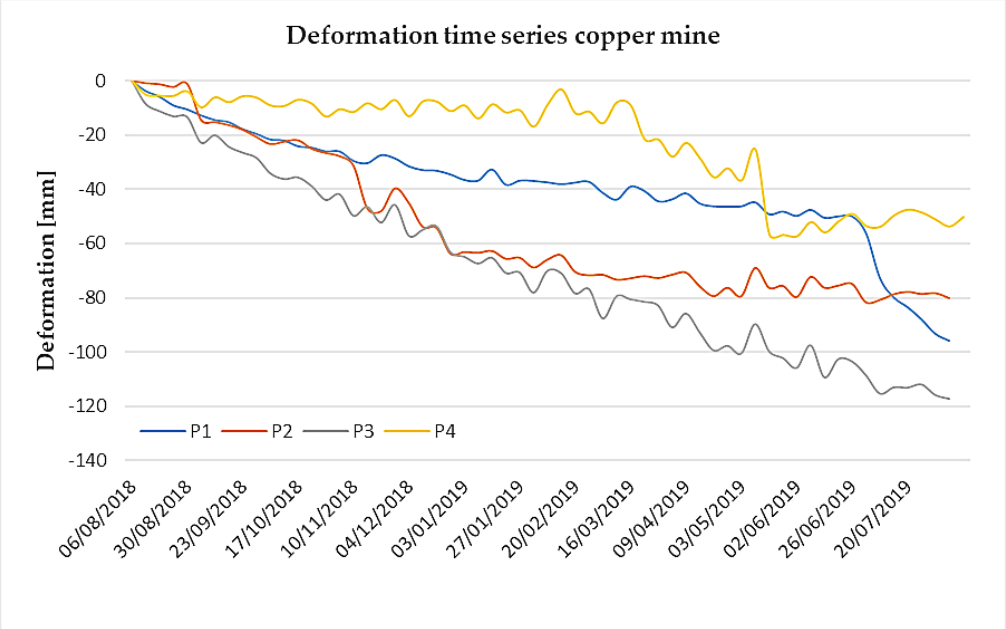

Figure 5.6 Deformation time series of North Chile open pit mine -example 2 of points P1, P2, P3 and P4 shown in figure 5.5.

Figures 5.5 show another example of a different copper mine out of the same river basin in Chile. In this case, we used the DI approach to data acquired during a year (August

2018-July 2019), also in the ascending orbit. The area under study shows very high deformations, which is demonstrated with the time-series of points P1, P2 (slopes) and P3, P4 (stacks) in figure 5.6. The displacements ranging from -60 cm/year to 20 cm/year are mainly due to settlements of mining wastes in the stacks and slope instabilities of the mining pits, similar to the previous example. Most of the deformation points showed liner or bilinear trends in the time-series. These points also displayed brief periods of stability. The results, in this case, show the ability of the proposed approach to properly detect active areas. Moreover, the approach can be used as a tool for supporting in situ measurement by providing information about the area of influence of the phenomena.

5.2.2. The Hierro Island

As shown in the previous chapter El Hierro is the south-westernmost island of the Canaryian archipelago (Spain), located in the Atlantic Ocean off the coast of Africa. El Hierro Island is volcanic and sharply mountainous, hence is a highly prone area to landslides and slope failures. Hence the goal was to rapidly and semi-automatically generate a product to be easily exploited in the geohazard management by the Civil Protections Authorities and the Geological Surveys.

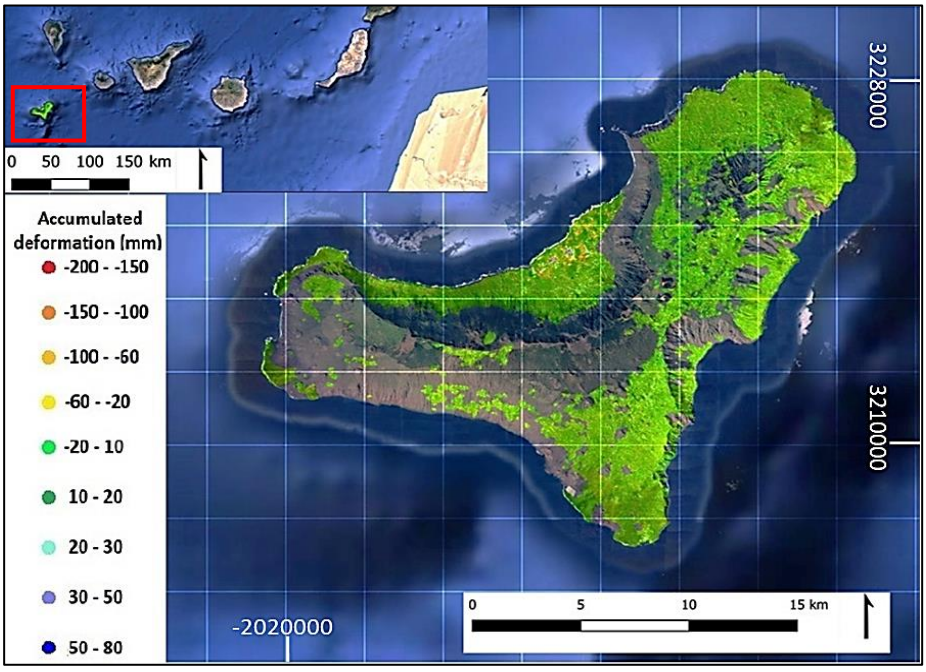

Figure 5.7 Satellite image showing the location of El Hierro in the Canaryian archipelago (Spain) and accumulated deformation map estimated for El Hierro island using the DI approach. The sampling density achieved (approximately 400 PS/km^2) can be inferred from this image.

The land cover is mainly volcanic rock fall, with sparse vegetation thus assuring high coherent radar response. The area of the island is approximately 260 km^2. The interferograms have good coherence and the occasional loss of coherence mainly affected the vegetated areas in the centre of the island. A stack of 74 S-1 images acquired in ascending orbit and 73 6-day interferograms were processed. The period of observations covers from 26-May-2017 to 02-July-2018. The points with mean coherence higher than 0.25 were used for the DI approach. The sampling density achieved in first instance was not deemed enough and, as a measure to improve the density of points, a spatial averaging within homogeneous coherent pixels of single look images were performed to form multi-looked observations. Most of the S-1 A-DInSAR processing approaches makes use of multi-looked images to reduce noise, but this averaging seems to be introducing a variant systematic signal, which shows no characteristics of stochastic noise, among the multi-looked interferograms, mimicking deformation signal patterns (figure 5.8). This signal, which in this case is present in highly coherent points, is not filtered out during pixel selection and can be wrongly interpreted as deformation patterns, especially when prior knowledge about the area under observation is unavailable. The complex geophysical characteristics of the Island, such as the coasts and the presence of high cliffs has significant influence in the signals. This signal is named 'fading signals' because of the reason that the signal perishes with the increment in temporal baseline.

Figure 5.8 shows the same result of figure 5.7 but in SAR geometry. The goal of this figure is to emphasize some peculiar deformation areas and to better show the level of noise of the results. The figure displays the time-series of two points in two different parts of the Island. The first point is located in the north of the Island. Even though it does not display a huge linear trend as point 2, it still shows a slight shift away from the satellite that can be wrongly interpreted as deformation. The second point displays a linear systematic trend towards the satellite starting from 0 to 16 mm in a period of one year, which can be characterized as upheaval under usual deformation analysis.

Since ground validation of these deformations were difficult to be undertaken and the area is of highly complex physical phenomena, it was practically easier to adopt a new method which can omit these kinds of points showing such deformation patterns, where in fact we do not know if these deformations are actually happening.

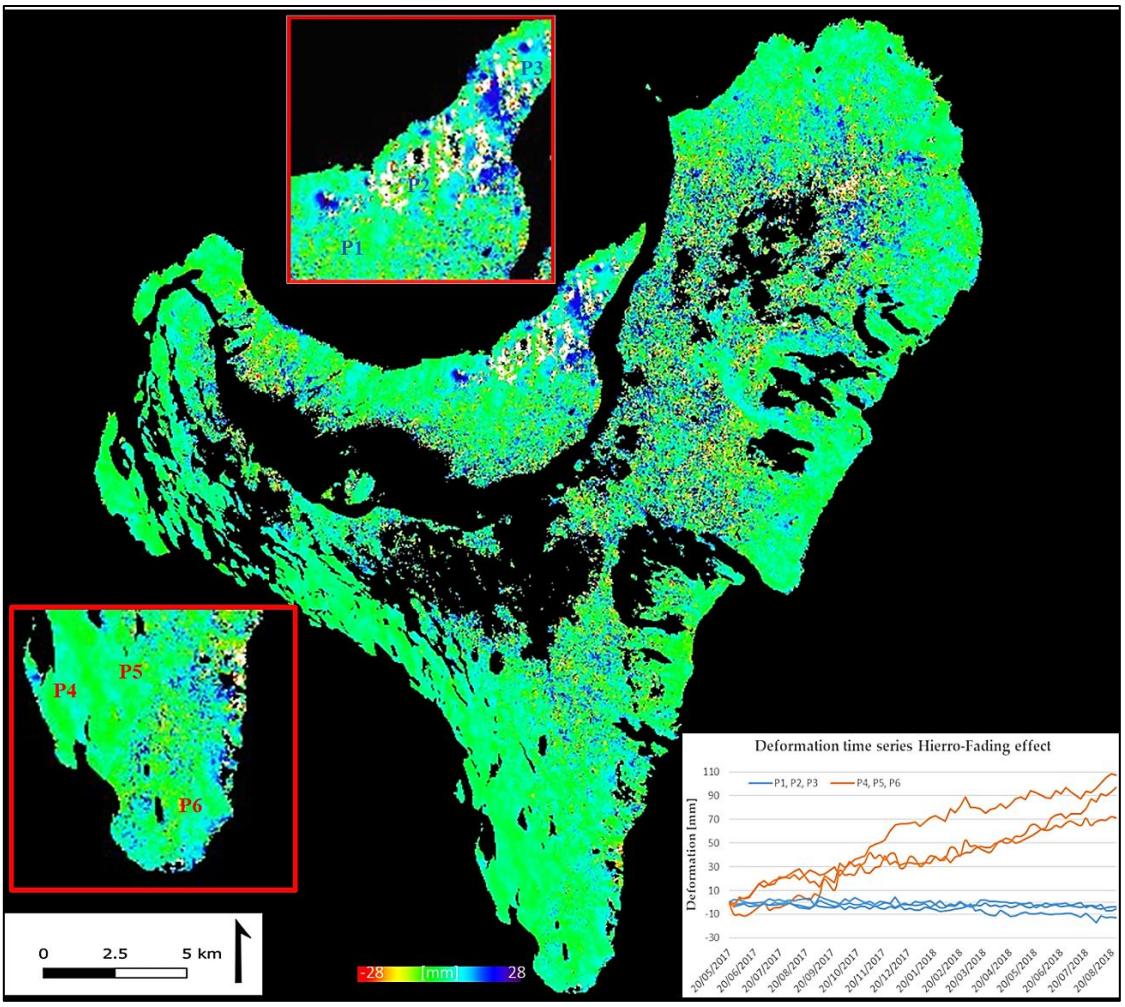

Figure 5.8. Accumulated displacement map of El Hierro island and examples of time series obtained with the DI approach. The time-series of two sets of points P1, P2, P3 and P4, P5, P6 located in the seemingly unstable and stable areas of the island respectively are shown to demonstrate fading effects.

5.3. PSIG-short temporal baseline approach

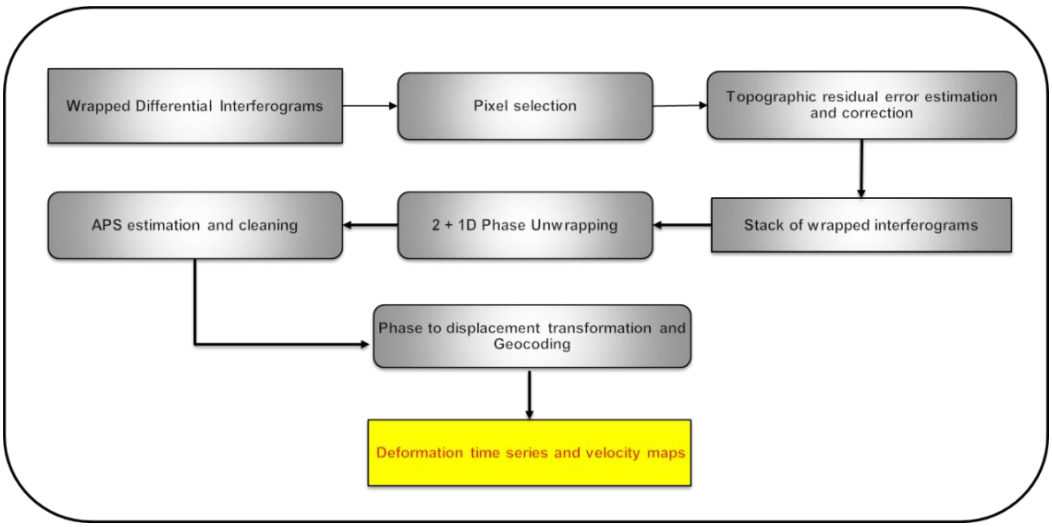

Figure 5.9 PSIG-STB approach

The main objective of the PSIG chain is to extend the interferometric analysis to wider areas using a unique, redundant, and connected network of points. The main goal is to propose a method with the same reliability of the standard A-DInSAR approaches but significantly improving the sampling density and reducing the phase unwrapping error sources.

Here, we propose a slightly different PSIG approach by constraining the temporal baselines to a given threshold, the PSIG-STB approach. The inputs include a stack of N co-registered SAR images, the dispersion of amplitude or coherence images and M wrapped interferograms, with M >> N. For each image, all the possible interferograms below a temporal baseline threshold are generated. The goal of the network is to ensure a good temporal sampling while preserving a high interferometric coherence. For instance, in the cases discussed in this paper, we have used interferograms with temporal baselines lower than 30 days. The procedure is illustrated in Figure 5.9. The main steps are described here below:

1) Pixel selection*:* The first step is the pre-pixel selection. It is based on the dispersion of amplitude index. The threshold might vary for different sites and the final value seeks a trade-off between sampling density and noise.
2) Topographic error estimation and correction: In this step, the topographic error of the DEM used in the interferogram generation is estimated. The assumption is that the phase component related to the residual topographic error, the thermal phase component and the phase noise are spatially uncorrelated. Given this assumption, the atmospheric component is the only phase component spatially correlated over stable areas. The approach used is described in [70] and is based in the maximization of the function as shown in Eq.2.7. For S-1 it means interferograms with temporal baselines of 6-12 days. This network allows hypothesizing that the phase component caused by movement is almost negligible in most of the interferograms. The algorithm is based on brute force. A range of potential topographic errors is tested and the one that reaches the maximum γ is selected. The γ ranges between 0 and 1. The higher the value the better the agreement between topographic model and observations. Only those points with a γ higher than a given threshold are selected for the subsequent steps. The use of high coherent interferograms allows us to have a very dense network of points with relatively high γ. The estimated topographic error is removed from each interferogram for each selected point.

3) 2+1D phase unwrapping: this step exploits a two-step phase unwrapping described in [70] and as shown in Eq.2.5. and Eq.2.6. The first step consists in a spatial phase unwrapping. The algorithm used is based in the Minimum Cost Flow method and is performed for each interferogram of the network and only using the points selected in the previous step. The second step is carried out point wise and performs a temporal consistency check of the unwrapped interferograms. The particularity in the context of S-1 is the network used. The high temporal sampling allows redundant networks to be produced with more than five interferograms per image with maximum temporal baselines of 30-60 days. Under these conditions, i.e., dense networks of points without topographic component and with low noise, the spatial phase unwrapping use to have reliable behaviour and the temporal consistency check provides its best performances. The final output of this step is, for each point, the temporal evolution of the phase, i.e., the time series. After the 2+1D phase unwrapping, we perform the APS filtering in the same way than in the DI procedure and we conclude with the estimation of the deformation velocity by using a robust linear regression for each displacement time series. In the present scenario, the PSIG-STB approach was developed as a different validation approach, when the DI approach revealed a peculiar systematic signal in multi-looked 6-day interferograms, especially in large, high humidity areas.

5.3.1. El Hierro results

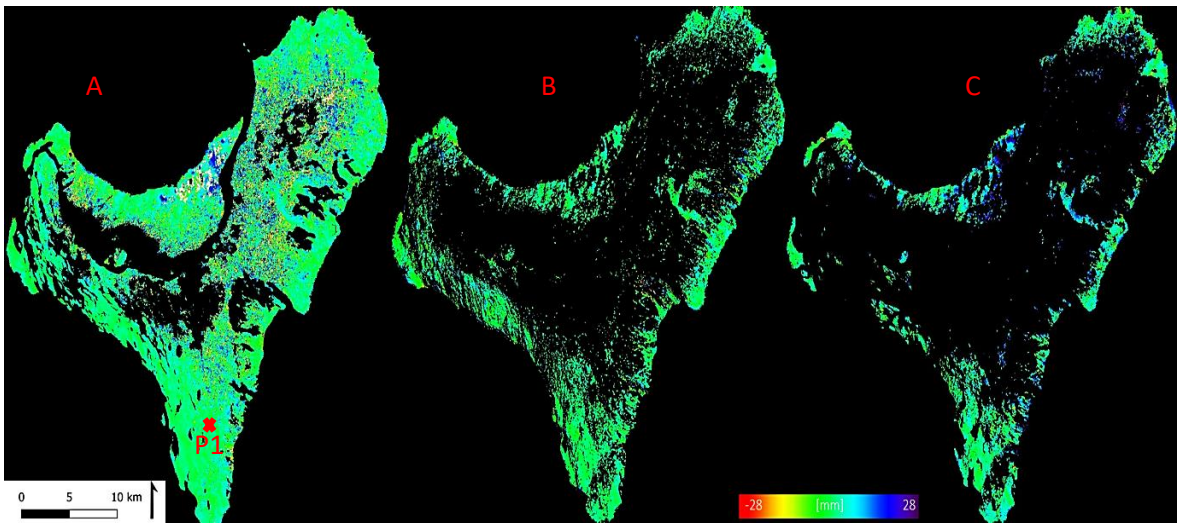

Figure 5.10 Accumulated deformation map of El Hierro island (Spain) estimated with multi-looked interferograms for a period of one year using A. the DI approach, B. the PSIG-STB approach and C. the standard PSIG approach

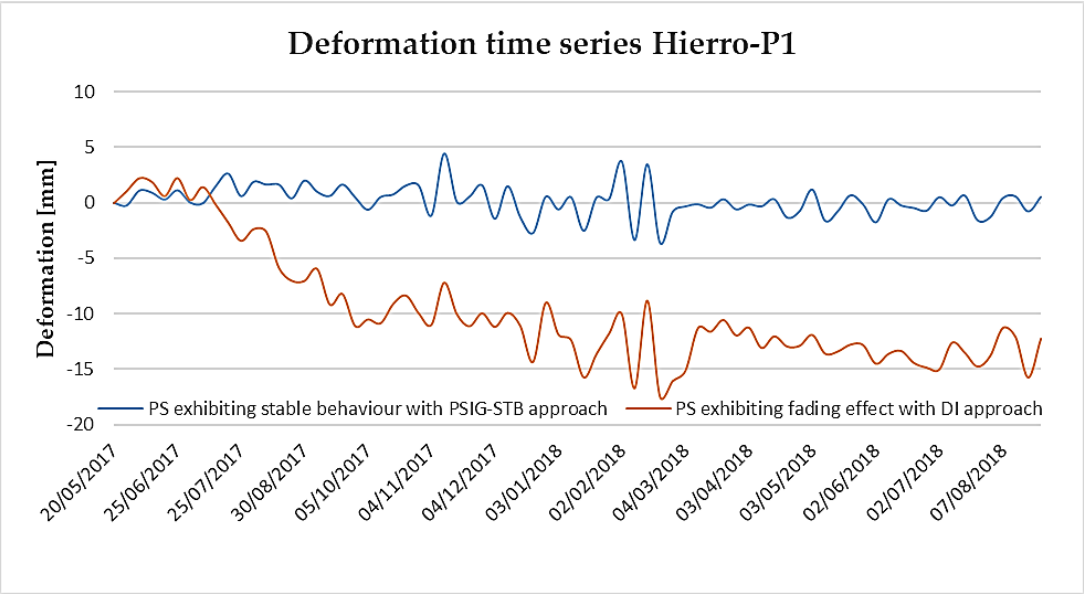

Figure 5.11 Example of fading effect exhibited by point P1 in figure 11 estimated using the DI approach in comparison with the same point exhibiting stable behaviour estimated using the PSIG-STB approach.

As mentioned before, if unattended, this particular signal can severely bias the deformation estimates of PS. The PSIG-STB approach proved itself a competent alternative in areas where the DI approach exhibited fading signals. Figure 5.10 shows the results obtained with (a) the DI, (b) the PSIG-STB and (c)the PSIG approaches, respectively. Many of such highly coherent 'problematic' points are filtered out in the PSIG-STB method. Almost all fading effects were filtered or not selected as good points. It can be seen that most of the points in (b) are showing an absolute deformation velocity below 1 mm/yr. The corresponding time series should ideally contain only a negligible deformation. Figure 5.11 shows one such point in the southern part of the island (P1 in figure 5.8), which had shown fading effects while using only the multi-looked 6-day interferograms in the DI approach. This unaccountable behavior has been corrected using the PSIG-STB approach. This approach also has the same advantages of DI, i.e., easy to implement but provides also robust results. However, the point density is sensibly lower. The accumulated deformation map resulted in a standard deviation (σ) of 0.95 mm, proving that most part of the island displayed stable behaviour in the PSIG-STB approach. Only the time series corresponding to8657 points out of 57821 points included in the dataset (i.e., the 15% of the points) have a total standard deviation higher than 1.9 mm. These statistics were considered satisfactory in the considered deformation monitoring.

To assess the performance of PSIG-STB approach, we also processed the standard PSIG chain described in [70]. The comparison between the accumulated deformation estimated

using the standard PSIG approach and the PSIG-STB approach is also provided in figure 5.10. The main advantages of the PSIG-STB approach over the standard PSIG approach is the reduction of phase unwrapping errors and jumps and an increase of 6% of the point density, i.e. 57821 points using the PSIG-STB and 54545 using the standard PSIG. The PSIG-STB approach is faster than the standard PSIG approach, efficiently and effectively filters out all the problematic points, showing fading effects. Especially, in this case where pixel selection with high coherence or dispersion of amplitude (DA) did not eliminate the points with strange trends, because the island has a high radar response. As a general statement, we assume that under the same conditions, in most of the cases, with shorter temporal baselines we will have higher spatial point density and thus easier spatial phase unwrapping. This is significantly important to solve phase unwrapping of relatively fast displacements as well as to reduce the phase unwrapping errors due to atmospheric phase component. Finally, it is worth noting that the PSIG approach shows an uplift area in the north east of the island. To the author`s knowledge there should be this type of activity during the monitored period [99]. Thus, we interpret that it could be related to phase unwrapping errors due to the atmosphere. It is clearly seen that these artefacts are not present in the PSIG-STB results.

The accumulated deformation map resulted in a standard deviation (σ) of 0.95 mm, proving that most part of the island displayed stable behaviour in the PSIG-STB approach. Only the time series corresponding to 8657 points out of 57821 points included in the dataset (i.e., the 15% of the points) have a total standard deviation higher than 1.9 mm. These statistics were considered satisfactory in the considered deformation monitoring.

5.3.2. Barcelona metropolitan area

The PSIG-STB procedure has been applied to the metropolitan area of Barcelona, Catalonia, Spain. Different types of geohazards such as urban settlement, mining subsidence and landslides have been identified in this study area. The inherently short-lived but physically present ‘fading signals’ were attributed as an outcome of multi-looked SAR images in [52]. However, in the study area of Catalonia, these signals were again present under the DI approach. Note that the two conventional product estimates of DInSAR, the surface displacement time series and displacement velocity are both compromised in the presence of these fading signals. Hence, we considered this study area was suitable to perform an additional, complementary deformation monitoring

analysis using PSIG-STB. In this case study, we limit our analysis to the efficiency in detection of PS and displacement time series, as it is usually done in urban applications, using PSIG-STB.The study area lies in the region of Catalonia, which is covered by a single S-1 frame. The analysed dataset includes 245 SLC S-1 images, which cover the period from March 6, 2015 to May 26, 2020.

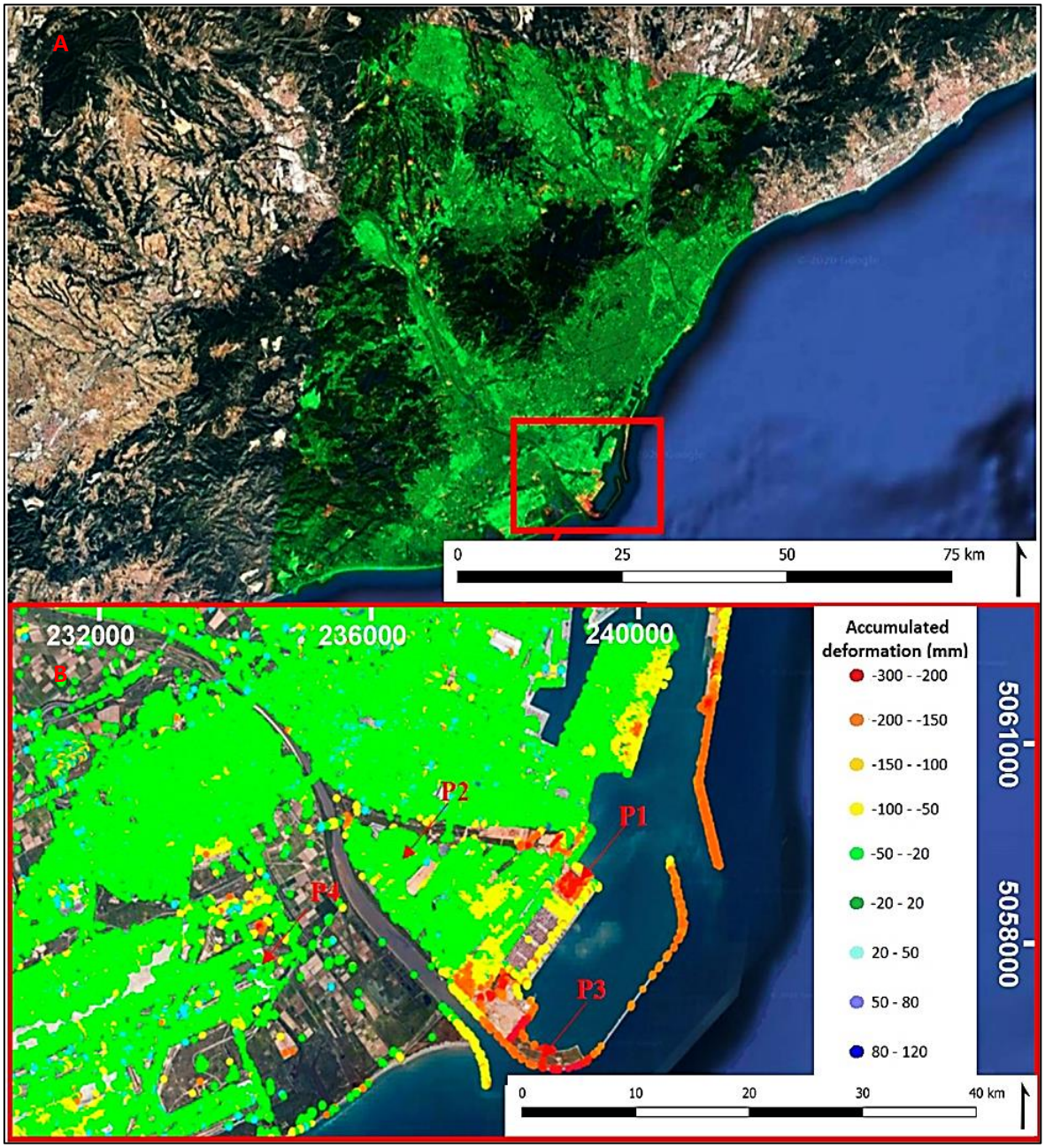

Figure 5.12 Accumulated deformation map of Barcelona metropolitan area (A) with a zoom of the Barcelona port dikes with more than 10 cm of accumulated displacement from January 2017 to January 2019 (B). The displacement time series of the points P1, P2, P3, P4 are shown in figure 5.13.

The interferograms were generated at full resolution using all possible image combinations, with a limit of 60 days. Even though the decorrelation was mainly due to vegetation coverage and topography, a good compromise had to be made between the noisy phase and the spatial coverage of PSs. Points with dispersion of amplitude lower than 0.4 were selected for the processing. Figure 5.12 shows the estimated accumulated displacement map for the processed area (A) and for a zone of the Barcelona harbour (B). In figure 5.12 A we observe several displacement areas that correspond to different movement phenomena such as mining activities, intense water extraction or urban construction as well as heavy surface loads or landslides. Figure 5.12 B shows a magnified portion with the Barcelona Port and El Prat Airport. Port dikes show values of more than 10 cm of accumulated displacement from January 2017 to January 2019. Figure 5.13 shows four examples of time series of points P1, P2, P3 and P4 indicated in figure 5.12, where different types of behaviours can be identified. In a relatively small area, there are deformations corresponding to an uplift (P4), probably related to underground water recovery. Some of the uplift detected in areas along the shores of the Llobregat River is mainly caused by sedimentation. The displacement in the whole frame ranged from -300 mm/year to 150 mm/year. Then there are PSs that are moving away from the satellite revealing a significant amount of sinking or subsidence, such as the points in the port and some structures in the urban area (P1 and P3): settlements in the dyke (P3) or in the harbour (P1). Then there are stable points where all the observations are consistent, with less or no outlier candidates (e.g., P2), which helps to assess the quality of the deformation time series.

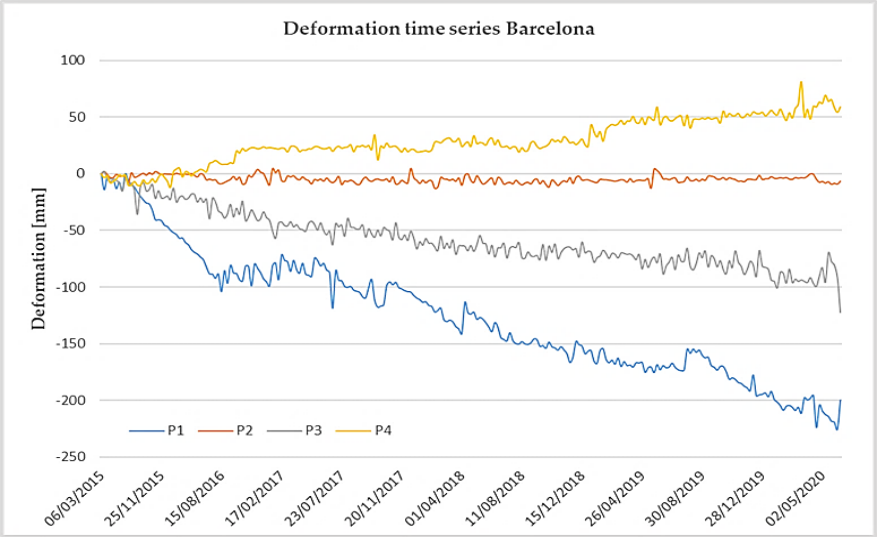

Figure 5.13 Accumulated deformation time-series for a period of 5 years of points P1, P2, P3 and P4 in figure 5.12 using the PSIG-STB approach with full-resolution SLC images.

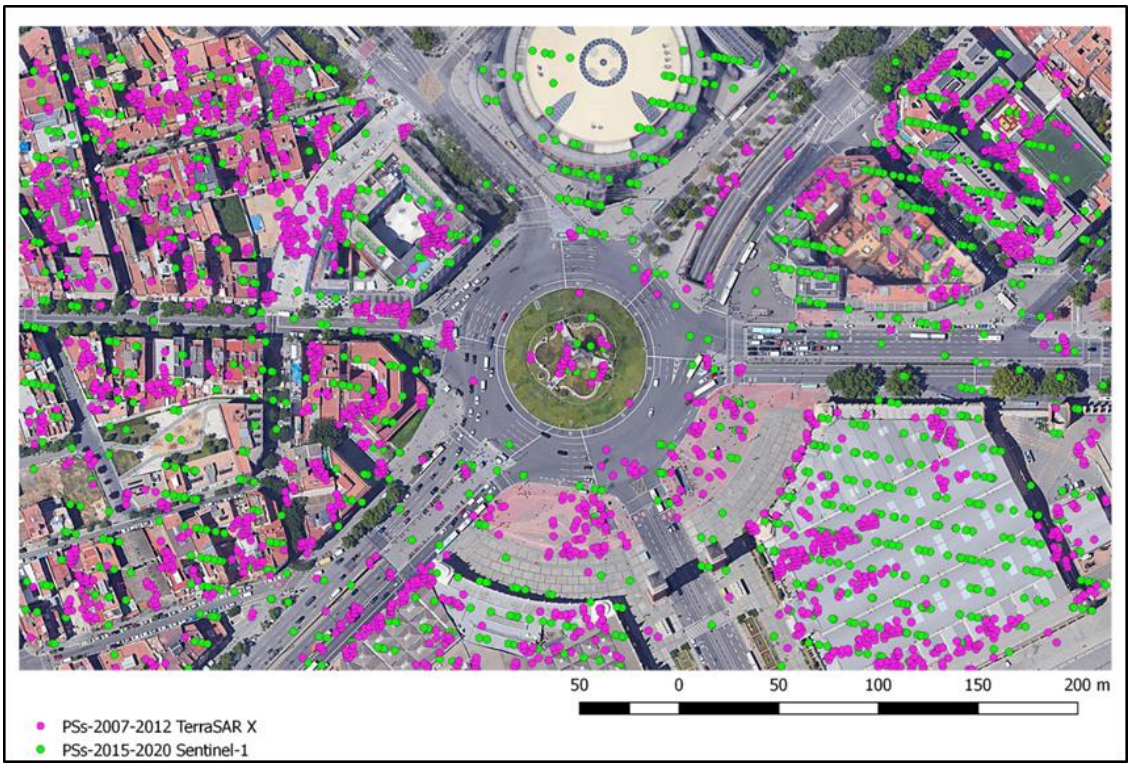

Figure 5.14 PS density TerraSAR X vs Sentinel-1

For a better understanding of the merits of the proposed method a comparison is made for standard PS and PSIG-STB. Even though the density of the PSs (1637 and 1766) in the given frame which shows a main square in the city of Barcelona- Placa de Espanya, the spatial distribution of the PSs are cluttered in standard PSIG approach, but are very well apportioned with the combination of Sentinel-1 data and PSIG-STB methodology. Although an improvement was visible with phase unwrapping, the main advantage of this approach as mentioned before has to be its promptitude, which is quite essential when it comes to having a pilot study of the area of interest, with an automated flow chain.

5.4. Discussion

With the implementation of the fully automatic approaches in three different areas, characterized by substantially different physical, geographical and meteorological conditions, it can be inferred that an unsupervised identification and pre-screening of the deformational processes is possible. The results of copper mines (Chile study case) demonstrate the capability of the DI approach to discern active areas and to deliver high quality deformation maps to aid in situ monitoring. In this area of dry physiography, the DI approach revealed very high deformations. So even with phase unwrapping errors it gave enough information to end-users to conclude whether a comprehensive analysis of

the active areas is necessary. Future investigations should test methods to better understand the nature and mitigate the effects of the fading effect in multi-looked interferograms (as shown for El Hierro) and to find ways to detect points potentially affected by phase unwrapping errors.

As the areas of interest became vast, and their topography became intricate, the deformations were impaired with more phase unwrapping errors and fading effects. Since these tricky points were persistent after pixel selection based on coherence, it was pragmatic to endorse another data-driven approach to acquire accurate deformation maps, thereby proceeding to the PSIG-STB approach. This approach has demonstrated to be a method able to be used in both urban and natural environments and showing robust results. However, compared to the DI it shows a significant decrease in the sampling density which can result in the loss of key information. Thus, a systematic approach to deal with wide areas can be to use the DI to rapidly detect those areas potentially affected by displacement and then apply the STB-PSIG on the detected moving areas. PSIG is a very consolidated PSI chain that has been widely used in previous publications by several groups worldwide. Thus, we consider PSIG-STB would not have a decrease of reliability with respect PSIG chain.

Some of the characteristic spikes and dips in the deformation time series correspond to phase unwrapping errors when the jump between two consecutive dates is equal to 2π or multiples of 2π. These errors are very common in A-DInSAR analysis and tolerable since many times they can be identified and rectified with point-by-point analysis. Although an overall improvement was visible with phase unwrapping, in the PSIG-STB approach, the main advantage of both the methods as mentioned before has to be the promptitude, which is quite essential when it comes to having a pilot study of the area of interest, with a self driven flow chain. If we consider the processing time, the standard PSIG chain remains the reference technique. After all, it has to be noted that the time series of the PSs depicted in the paper is the result of two automated approaches; it can definitely be improved with careful and skilled interpretation and rectification.

While dealing with the fading effects in further studies, it is debatable whether it is possible to insert a form of "intelligent filter" in the downstream of the processing chain that can distinguish the reliable time series from the artificially created ones. Unfortunately, this work supports the inference that this distinction is not feasible. Because our results show that, the artificially created fading effects also exhibit linear or

bilinear trends similar to a deformation time series. Thus, a pixel selector upstream the processing chain that helps to identify the good points offers the advantage of not interpreting artificial trends as real ones.

Finally, it is worth mentioning that the forthcoming constellations such as Capella Space or Ice Eye will be able to provide shorter revisit times. Therefore, with such a short revisit time, arises a need for near real time processing, to fully exploit the data available in the near future. In such a scenario, the proposed approaches will be really useful as automated tools to perform a preliminary study.

Chapter 6

Conclusions

Since the invention of Persistent scatterer interferometry efforts have always been made in the following technical aspects (not limited to) of the technique:

- Pixel selection to improve the quality and quantity of the scatterers
- Phase unwrapping algorithms to reduce errors
- Improving the flexibility of deformation and atmospheric models
- Integration of data from various sensors and sources to validate and analyse the observations better

This work had been made to fit in the context of these general research areas. The three post-processing approaches complementing the PSIG chain of CTTC have been implemented and the results derived with the Sentinel-1 SAR dataset have been analyzed in this thesis. All the data driven approaches depicted in this thesis are designed to fully exploit the Sentinel-1 data. It does not claim to introduce new algorithm but simple tweak the existing DInSAR techniques and customize it to Sentinel-1 capabilities, which has resulted in fast, semi-automatic deformation monitoring tools. In addition, a study on using external data that can be integrated into the processing chain for atmospheric phase screen estimation has also been presented in this document. The conclusions are organized in two main blocks: the conclusions related to the work done in this thesis focusing on the positive outcomes, the limitations regarding the proposed methodologies and the scope of future research to overcome the same.

Focusing on the successful part of the thesis, which consists of the three complementary approaches, namely the splitting, the DI, and the PSIG-STB the following inferences, can be made:

- The main characteristics and performances of the proposed procedures have been illustrated in the results obtained from three different cases of study. The main advantages and drawbacks have been pointed out and discussed.
- All three approaches provide fast and straightforward solutions to analyse deformations affecting large areas.

- In comparison to the standard PSIG chain, the discussed approaches provide a denser PS sampling which allows the measurement of deformations that were not observable using the standard PSIG.
- The DI approach provides a light way for fast analysis of large areas ensuring good point density but has a strong dependence on the operator data analysis skills.
- The splitting and the PSIG–STB approach provides a robust method able to assess the reliability of the active areas detected by the DI but also very useful to be used instead of standard A-DInSAR approaches. It provides very nice performances compared to a classical PS chain like the PSIG approach by improving both the point density as well as the robustness against phase unwrapping errors.

As mentioned before, the main advantages of the proposed methods are the promptness, convenience and the possibility of an automatic generation of deformation maps and time series to reveal displacement phenomena for wide areas and to fully exploit the detection ability of InSAR based on S-1 datasets. In addition, improvements in the time series as well as in the density of points are observed for all the datasets using the DI and PSIG-STB methods in comparison to the traditional PSIG chain. With emphasis on that point the following pointers can be made regarding the limitations of the techniques mentioned in this study.

- Even though a number of studies are being conducted in the atmospheric signals of the SAR data, the spectral signatures of APS signals are not evaluated. In addition, a lack of data and models can capture the volatility of the atmospheric signals.
- The improvement of the PSs is in quantity, the quality of the PS needs to be further evaluated. For filtering of points, the generation of a quality index for each image of a given deformation time series can be carried out .
- In this thesis, we also pointed out the presence of a peculiar systematic signal in multi-look interferograms. The results show that the appearance of fading signals that can lead to wrong interpretation of false ground movements. The analysis of such fading signals serves as an example to show that, for an effective calibration, we need to perform comprehensive research on various possible physical sources

of inconsistencies and design case-specific models to explain the interferometric phase of each source.

- Generally, the PSI validation activities are based on the comparison of deformation velocities and time series with independent estimations of the same quantities acquired by sources of better quality, e.g., levelling or GPS measurements. In any case, for the fading effects, further studies on various test sites are inevitable.

Funding: This work has been partially funded by AGAUR, Generalitat de Catalunya, through a grant for the recruitment of early-stage research staff (Ref: FI_B 00741) and through the Consolidated Research Group RSE, "Remote Sensing" (Ref: 2017-SGR-00729). It has been also partially funded by the Spanish Ministry of Economy and Competitiveness through the DEMOS project "Deformation monitoring using Sentinel-1 data" (Ref: CGL2017-83704-P) and by AGAUR.

References

1. Crosetto, M., Monserrat, O., Iglesias, R., & Crippa, B. (2010). Persistent scatterer interferometry. Photogrammetric Engineering & Remote Sensing, 76(9), 1061-1069.
2. Massonnet, D. and Feigl, K.L., 1998. Radar interferometry and its application to changes in the Earth's surface. Reviews of geophysics, 36(4), pp.441-500.
3. Zebker, H.A. and Goldstein, R.M., 1986. Topographic mapping from interferometric synthetic aperture radar observations. Journal of Geophysical Research: Solid Earth, 91(B5), pp.4993-4999.
4. Madsen, S.N., Zebker, H.A. and Martin, J.A.N.M., 1993. Topographic mapping using radar interferometry: Processing techniques. IEEE Transactions on Geoscience and remote sensing, 31(1), pp.246-256
5. Amelung, F., Galloway, D.L., Bell, J.W., Zebker, H.A., Laczniak, R.J., 1999. Sensing the ups and downs of Las Vegas: InSAR reveals structural control of land subsidence and aquifer-system deformation. Geology, 27(6), 483-486.

6. Gao, Q., Zribi, M., Escorihuela, M. J., & Baghdadi, N. (2017). Synergetic use of Sentinel-1 and Sentinel-2 data for soil moisture mapping at 100 m resolution. Sensors, 17(9), 1966.
7. Massonnet, D., Feigl, K., Rossi, M. and Adragna, F., 1994. Radar interferometric mapping of deformation in the year after the Landers earthquake. Nature, 369(6477), p.227.
8. Delouis, B., Nocquet, J. M., & Vallée, M. (2010). Slip distribution of the February 27, 2010 Mw= 8.8 Maule earthquake, central Chile, from static and high-rate GPS, InSAR, and broadband teleseismic data. Geophysical Research Letters, 37(17).
9. Béjar-Pizarro, M., Álvarez Gómez, J. A., Staller, A., Luna, M. P., Pérez-López, R., Monserrat, O., ... & Mateos, R. M. (2018). InSAR-based mapping to support decision-making after an earthquake. Remote Sensing, 10(6), 899.
10. Bawden, G.W., Thatcher, W., Stein, R.S., Hudnut, K.W. and Peltzer, G., 2001. Tectonic contraction across Los Angeles after removal of groundwater pumping effects. Nature, 412(6849), p.812.
11. Solari, L., Del Soldato, M., Raspini, F., Barra, A., Bianchini, S., Confuorto, P., ... & Crosetto, M. (2020). Review of Satellite Interferometry for Landslide Detection in Italy. Remote Sensing, 12(8), 1351.
12. Wegmüller, U., Walter, D., Spreckels, V., Werner, C.L., 2010. Nonuniform ground motion monitoring with TerraSAR-X persistent scatterer interferometry. IEEE TGARS, 48, 895–904.
13. Ge, L., Chang, H.C. and Rizos, C., 2007. Mine subsidence monitoring using multi-source satellite SAR images. Photogrammetric Engineering & Remote Sensing, 73(3), pp.259-266
14. Galloway, D.L., Hudnut, K.W., Ingebritsen, S.E., Phillips, S.P., Peltzer, G., Rogez, F. and Rosen, P.A., 1998. Detection of aquifer system compaction and land subsidence using interferometric synthetic aperture radar, Antelope Valley, Mojave Desert, California. Water Resources Research, 34(10), pp.2573-2585.
15. Fruneau, B., Deffontaines, B., Rudant, J.P. and Le Parmentier, A.M., 2005. Monitoring vertical deformation due to water pumping in the city of Paris (France) with differential interferometry. Comptes Rendus Geoscience, 337(13), pp.1173-1183.

16. Fielding, E.J., Blom, R.G. and Goldstein, R.M., 1998. Rapid subsidence over oil fields measured by SAR interferometry. Geophysical Research Letters, 25(17), pp.3215-3218.
17. Yu, B., Liu, G., Li, Z., Zhang, R., Jia, H., Wang, X., Cai, G., 2013. Subsidence detection by TerraSAR-X interferometry on a network of natural persistent scatterers and artificial corner reflectors. Computers & Geosciences, 58, 126-136.
18. Gabriel, A.K., Goldstein, R.M. and Zebker, H.A., 1989. Mapping small elevation changes over large areas: differential radar interferometry. Journal of Geophysical Research: Solid Earth, 94(B7), pp.9183-9191.
19. Crosetto, M., Monserrat, O., Cuevas-González, M., Devanthéry, N., & Crippa, B. (2016). Persistent scatterer interferometry: A review. ISPRS Journal of Photogrammetry and Remote Sensing, 115, 78-89.
20. Aslan, G., Foumelis, M., Raucoules, D., De Michele, M., Bernardie, S., & Cakir, Z. (2020). Landslide Mapping and Monitoring Using Persistent Scatterer Interferometry (PSI) Technique in the French Alps. Remote Sensing, 12(8), 1305.
21. Reyes-Carmona, C.; Barra, A.; Galve, J.P.; Monserrat, O.; Pérez-Peña, J.V.; Mateos, R.M.; Notti, D.; Ruano, P.; Millares, A.; López-Vinielles, J.; et al. Sentinel-1 DInSAR for Monitoring Active Landslides in Critical Infrastructures: The Case of the Rules Reservoir (Southern Spain). Remote Sens. 2020, 12, 809.
22. Costantini, M.; Ferretti, A.; Minati, F.; Falco, S.; Trillo, F.; Colombo, D.; Novali, F.; Malvarosa, F.; Mammone, C.; Vecchioli, F.; et al. Analysis of surface deformations over the whole Italian territory by interferometric processing of ERS, Envisat and COSMO-SkyMed radar data. Remote Sens. Environ. 2017, 202, 250–275.
23. Solari, L., Crosetto, M., Balasis-Levinsen, J., Casagli, N., Frei, M., Moldestad, D. A., & Oyen, A. (2020, May). The European Ground Motion Service: a continental scale map of ground deformation. In EGU General Assembly Conference Abstracts (p. 3148).
24. Solari, L., Bianchini, S., Franceschini, R., Barra, A., Monserrat, O., Thuegaz, P., ... & Catani, F. (2020). Satellite interferometric data for landslide intensity evaluation in mountainous regions. International Journal of Applied Earth Observation and Geoinformation, 87, 102028.

25. Frattini, P.; Crosta, G.B.; Rossini, M.; Allievi, J. Activity and kinematic behaviour of deep-seated landslides from PS-InSAR displacement rate measurements. Landslides 2018, 15, 1053–1070.
26. Barra, A., Solari, L., Béjar-Pizarro, M., Monserrat, O., Bianchini, S., Herrera, G., ... & Ligüerzana, S. (2017). A methodology to detect and update active deformation areas based on sentinel-1 SAR images. Remote sensing, 9(10), 1002
27. Wright, T., Parsons, B. and Fielding, E., 2001. Measurement of interseismic strain accumulation across the North Anatolian Fault by satellite radar interferometry. Geophysical Research Letters, 28(10), pp.2117-2120.
28. Crosetto, M., Monserrat, O., Cuevas, M. and Crippa, B., 2011. Spaceborne differential SAR interferometry: Data analysis tools for deformation measurement. Remote Sensing, 3(2), pp.305-318.
29. Bonano, M., Manunta, M., Marsella, M. and Lanari, R., 2012. Long-term ERS/ENVISAT deformation time-series generation at full spatial resolution via the extended SBAS technique. International Journal of Remote Sensing, 33(15), pp.4756-4783.
30. Mora, O., Mallorqui, J.J. and Broquetas, A., 2003. Linear and nonlinear terrain deformation maps from a reduced set of interferometric SAR images. IEEE Transactions on Geoscience and Remote Sensing, 41(10), pp.2243-2253.
31. Ferretti, A., Fumagalli, A., Novali, F., Prati, C., Rocca, F. and Rucci, A., 2011. A new algorithm for processing interferometric data-stacks: SqueeSAR. IEEE Transactions on Geoscience and Remote Sensing, 49(9), pp.3460-3470.
32. Crosetto, M., Devanthéry, N., Cuevas-González, M., Monserrat, O. and Crippa, B., 2014. Exploitation of the full potential of Persistent Scatterer Interferometry data. The International Archives of Photogrammetry, Remote Sensing and Spatial Information Sciences, 40(7), p.75.
33. Monserrat, O., Crosetto, M., Cuevas, M. and Crippa, B., 2011. The thermal expansion component of persistent scatterer interferometry observations. IEEE Geoscience and Remote Sensing Letters, 8(5), pp.864-868.
34. Berardino, P., Fornaro, G., Lanari, R., & Sansosti, E. (2002). A new algorithm for surface deformation monitoring based on small baseline differential SAR interferograms. IEEE Transactions on geoscience and remote sensing, 40(11), 2375-2383.

35. Eineder, M., Adam, N., Bamler, R., Yague-Martinez, N. and Breit, H., 2009. Spaceborne spotlight SAR interferometry with TerraSAR-X. IEEE Transactions on Geoscience and Remote Sensing, 47(5), pp.1524-1535.
36. Fornaro, G., Reale, D. and Verde, S., 2013. Bridge thermal dilation monitoring with millimeter sensitivity via multidimensional SAR imaging. IEEE Geoscience and Remote Sensing Letters, 10(4), pp.677-681.
37. Crosetto, M., Monserrat, O., Cuevas-González, M., Devanthéry, N., Luzi, G. and Crippa, B., 2015. Measuring thermal expansion using X-band persistent scatterer interferometry. ISPRS Journal of Photogrammetry and Remote Sensing, 100, pp.84-91.
38. Barra, A., Monserrat, O., Mazzanti, P., Esposito, C., Crosetto, M. and Scarascia Mugnozza, G., 2016. First insights on the potential of Sentinel-1 for landslides detection. Geomatics, Natural Hazards and Risk, 7(6), pp.1874-1883.
39. Huang, Q., Crosetto, M., Monserrat, O. and Crippa, B., 2017. Displacement monitoring and modelling of a high-speed railway bridge using C-band Sentinel-1 data. ISPRS Journal of Photogrammetry and Remote Sensing, 128, pp.204-211.
40. Ferretti, A., Colombo, D., Fumagalli, A., Novali, F. and Rucci, A., 2015. InSAR data for monitoring land subsidence: time to think big. Proceedings of the International Association of Hydrological Sciences, 372, p.331.
41. Bru, G., González, P. J., Mateos, R. M., Roldán, F. J., Herrera, G., Béjar-Pizarro, M., & Fernández, J. (2017). A-DInSAR monitoring of landslide and subsidence activity: A case of urban damage in Arcos de la Frontera, Spain. Remote Sensing, 9(8), 787.
42. González, P. J., Bagnardi, M., Hooper, A. J., Larsen, Y., Marinkovic, P., Samsonov, S. V., & Wright, T. J. (2015). The 2014–2015 eruption of Fogo volcano: Geodetic modeling of Sentinel-1 TOPS interferometry. Geophysical Research Letters, 42(21), 9239-9246.
43. Albino, F., Biggs, J., Yu, C., & Li, Z. (2020). Automated Methods for Detecting Volcanic Deformation Using Sentinel-1 InSAR Time Series Illustrated by the 2017–2018 Unrest at Agung, Indonesia. Journal of Geophysical Research: Solid Earth, 125(2), e2019JB017908.
44. Sowter, A., Amat, M. B. C., Cigna, F., Marsh, S., Athab, A., & Alshammari, L. (2016). Mexico City land subsidence in 2014–2015 with Sentinel-1 IW TOPS:

Results using the Intermittent SBAS (ISBAS) technique. International journal of applied earth observation and geoinformation, 52, 230-242.

45. Delgado Blasco, J. M., Foumelis, M., Stewart, C., & Hooper, A. (2019). Measuring urban subsidence in the rome metropolitan area (italy) with sentinel-1 snap-stamps persistent scatterer interferometry. Remote Sensing, 11(2), 129.
46. Bakon, M., Czikhardt, R., Papco, J., Barlak, J., Rovnak, M., Adamisin, P., & Perissin, D. (2020). remotIO: A Sentinel-1 Multi-Temporal InSAR Infrastructure Monitoring Service with Automatic Updates and Data Mining Capabilities. Remote Sensing, 12(11), 1892.
47. López-Vinielles, J., Ezquerro, P., Fernández-Merodo, J. A., Béjar-Pizarro, M., Monserrat, O., Barra, A., ... & Sarro, R. (2020). Remote analysis of an open-pit slope failure: Las Cruces case study, Spain. Landslides, 17(9), 2173-2188.
48. Zinno, I., Bonano, M., Buonanno, S., Casu, F., De Luca, C., Manunta, M., ... & Lanari, R. (2018). National scale surface deformation time series generation through advanced DInSAR processing of sentinel-1 data within a cloud computing environment. IEEE Transactions on Big Data.
49. Tomás, R., Pagán, J. I., Navarro, J. A., Cano, M., Pastor, J. L., Riquelme, A., ... & Lopez-Sanchez, J. M. (2019). Semi-automatic identification and pre-screening of geological–geotechnical deformational processes using persistent scatterer interferometry datasets. Remote Sensing, 11(14), 1675.
50. Lanari, R., Bonano, M., Casu, F., Luca, C. D., Manunta, M., Manzo, M., ... & Zinno, I. (2020). Automatic Generation of Sentinel-1 Continental Scale DInSAR Deformation Time Series through an Extended P-SBAS Processing Pipeline in a Cloud Computing Environment. Remote Sensing, 12(18), 2961.
51. Galve, J. P., Pérez-Peña, J. V., Azañón, J. M., Closson, D., Caló, F., Reyes-Carmona, C., ... & Herrera, G. (2017). Evaluation of the SBAS InSAR service of the European space Agency's Geohazard Exploitation Platform (GEP). Remote Sensing, 9(12), 1291
52. Ansari, H., De Zan, F., & Parizzi, A. (2020). Study of Systematic Bias in Measuring Surface Deformation with SAR Interferometry.
53. Goldstein, R., 1995. Atmospheric limitations to repeat-track radar interferometry. Geophysical research letters, 22(18), pp.2517-2520.

54. Massonnet, D. and Feigl, K.L., 1995. Discrimination of geophysical phenomena in satellite radar interferograms. Geophysical research letters, 22(12), pp.1537-1540.
55. Zebker, H.A., Rosen, P.A. and Hensley, S., 1997. Atmospheric effects in interferometric synthetic aperture radar surface deformation and topographic maps. Journal of Geophysical Research: Solid Earth, 102(B4), pp.7547-7563.
56. Hanssen, R.F., Weckwerth, T.M., Zebker, H.A. and Klees, R., 1999. High-resolution water vapor mapping from interferometric radar measurements. Science, 283(5406), pp.1297-1299.
57. Tarayre, H. and Massonnet, D., 1996. Atmospheric Propagation heterogeneities revealed by ERS-1 interferometry. Geophysical Research Letters, 23(9), pp.989-992.
58. Ferretti, A., Savio, G., Barzaghi, R., Borghi, A., Musazzi, S., Novali, F., Prati, C. and Rocca, F., 2007. Submillimeter accuracy of InSAR time series: Experimental validation. IEEE Transactions on Geoscience and Remote Sensing, 45(5), pp.1142-1153.
59. Sandwell, David T., and Evelyn J. Price. "Phase gradient approach to stacking interferograms." Journal of Geophysical Research: Solid Earth 103.B12 (1998): 30183-30204.
60. Costantini, M., Farina, A. and Zirilli, F., 1999. A fast phase unwrapping algorithm for SAR interferometry. IEEE Transactions on Geoscience and Remote Sensing, 37(1), pp.452-460.
61. Bürgmann, R., Rosen, P.A. and Fielding, E.J., 2000. Synthetic aperture radar interferometry to measure Earth's surface topography and its deformation. Annual review of earth and planetary sciences, 28(1), pp.169-209.
62. Hanssen, R., 2001. Radar interferometry. Kluwer Academic Publishers, Dordrecht (The Netherlands)
63. Zebker, H. A., & Villasenor, J. (1992). Decorrelation in interferometric radar echoes. IEEE Transactions on geoscience and remote sensing, 30(5), 950-959.
64. Bamler, R., & Hartl, P. (1998). Synthetic aperture radar interferometry. Inverse problems, 14(4), R1.
65. Ferretti, A., Cespa, S., Novali, F., Perissin, D., Rocca, F., & Prati, C. (2006, May). PSInSAR: using satellite radar data to measure surface deformation remotely. In 3rd IAG/12th Symposium, Baden.

66. Blanco-Sanchez, P., Mallorquí, J. J., Duque, S., & Monells, D. (2008). The coherent pixels technique (CPT): An advanced DInSAR technique for nonlinear deformation monitoring. In Earth sciences and mathematics (pp. 1167-1193). Birkhäuser Basel.
67. Kampes, B., & Adam, N. (2005). The STUN algorithm for persistent scatterer interferometry. Proceedings of FRINGE 2005, 1-14.
68. Kampes, B. M. (2006). Radar interferometry (Vol. 12). The Netherlands: Springer.
69. Werner, C., Wegmuller, U., Wiesmann, A., & Strozzi, T. (2003, July). Interferometric point target analysis with JERS-1 L-band SAR data. In IGARSS 2003. 2003 IEEE International Geoscience and Remote Sensing Symposium. Proceedings (IEEE Cat. No. 03CH37477) (Vol. 7, pp. 4359-4361). IEEE.
70. Devanthéry, N., Crosetto, M., Monserrat, O., Cuevas-González, M., & Crippa, B. (2014). An approach to persistent scatterer interferometry. Remote sensing, 6(7), 6662-6679
71. Costantini, M., Falco, S., Malvarosa, F., Minati, F., & Trillo, F. (2009, July). Method of persistent scatterer pairs (PSP) and high-resolution SAR interferometry. In 2009 IEEE International Geoscience and Remote Sensing Symposium (Vol. 3, pp. III-904). IEEE.
72. Razi, P., Sumantyo, J. T. S., Perissin, D., & Kuze, H. (2018). Long-term land deformation monitoring using Quasi-Persistent Scatterer (Q-PS) technique observed by sentinel-1A: Case Study Kelok Sembilan. Advances in Remote Sensing, 7(4), 277-289.
73. Lanari, R., Casu, F., Manzo, M., Zeni, G., Berardino, P., Manunta, M., & Pepe, A. (2007). An overview of the small baseline subset algorithm: A DInSAR technique for surface deformation analysis. Deformation and Gravity Change: Indicators of Isostasy, Tectonics, Volcanism, and Climate Change, 637-661.
74. Crosetto, M., Biescas, E., Duro, J., Closa, J., & Arnaud, A. (2008). Generation of advanced ERS and Envisat interferometric SAR products using the stable point network technique. Photogrammetric Engineering & Remote Sensing, 74(4), 443-450.
75. Kuehn, F., Albiol, D., Cooksley, G., Duro, J., Granda, J., Haas, S., ... & Murdohardono, D. (2010). Detection of land subsidence in Semarang, Indonesia,

using stable points network (SPN) technique. Environmental Earth Sciences, 60(5), 909-921.

76. Ferretti, A., Novali, F., Fumagalli, A., Prati, C., Rocca, F., & Rucci, A. (2009, December). Beyond PSInSAR: the SqueeSAR approach. In AGU fall meeting abstracts (Vol. 2009, pp. G31A-02).
77. Hooper, A., Zebker, H., Segall, P., & Kampes, B. (2004). A new method for measuring deformation on volcanoes and other natural terrains using InSAR persistent scatterers. Geophysical research letters, 31(23).
78. Hooper, A. (2008). A multi-temporal InSAR method incorporating both persistent scatterer and small baseline approaches. Geophysical Research Letters, 35(16).
79. Wassie, Y., Mirmazloumi, S. M., Monserrat, O., Crippa, B., Palamà, R., Barra, A., & Crosetto, M. (2021, September). Interferometric SAR deformation timeseries: a quality index. In Microwave Remote Sensing: Data Processing and Applications (Vol. 11861, p. 118610A). SPIE.
80. Mirmazloumi, S. M., Wassie, Y., Navarro, J. A., Palamà, R., Krishnakumar, V., Barra, A., ... & Monserrat, O. (2022). Classification of ground deformation using sentinel-1 persistent scatterer interferometry time series. GIScience & Remote Sensing, 59(1), 374-392.
81. Doin, M.P., Lasserre, C., Peltzer, G., Cavalié, O. and Doubre, C., 2009. Corrections of stratified tropospheric delays in SAR interferometry: Validation with global atmospheric models. Journal of Applied Geophysics, 69(1), pp.35-50.
82. Xu, J., Peng, Y., & Xia, X. G. (2004). Parametric autofocus of SAR imaging-inherent accuracy limitations and realization. IEEE transactions on geoscience and remote sensing, 42(11), 2397-2411.
83. Smith, E. K., & Weintraub, S. (1953). The constants in the equation for atmospheric refractive index at radio frequencies. Proceedings of the IRE, 41(8), 1035-1037.
84. Boudouris, G. (1963). On the index of refraction of air, the absorption and dispersion of centimeter waves by gasses. J. Res. Natl. Bur. Stand., Sect., 67, 631-684.
85. Thayer, G. D. (1974). An improved equation for the radio refractive index of air. Radio Science, 9(10), 803-807.
86. Goldstein, R. M., & Werner, C. L. (1998). Radar interferogram filtering for geophysical applications. Geophysical research letters, 25(21), 4035-4038.

87. Xu, J., Peng, Y., & Xia, X. G. (2004). Parametric autofocus of SAR imaging-inherent accuracy limitations and realization. IEEE transactions on geoscience and remote sensing, 42(11), 2397-2411.
88. Brcic, R., Parizzi, A., Eineder, M., Bamler, R., & Meyer, F. (2011, July). Ionospheric effects in SAR interferometry: An analysis and comparison of methods for their estimation. In 2011 IEEE International Geoscience and Remote Sensing Symposium (pp. 1497-1500). IEEE.
89. Ding, X. L., Li, Z. W., Zhu, J. J., Feng, G. C., & Long, J. P. (2008). Atmospheric effects on InSAR measurements and their mitigation. Sensors, 8(9), 5426-5448.
90. Rommen, Bjorn, Agnes Mika, Leslie Gale, Hein Zelle, Ramon Hanssen, Shizhuo Liu, Christian Matzler et al. "The ESA METAWAVE project: Correcting for atmospheric water vapour effects in InSAR products." In 2009 3rd European Conference on Antennas and Propagation, pp. 3428-3432. IEEE, 2009.
91. Yu, C., Li, Z., Penna, N., & Crippa, P. (2018, April). Generic Atmospheric Correction Online Service for InSAR (GACOS). In EGU General Assembly Conference Abstracts (p. 11007).
92. Gao, X., Liu, Y., Li, T., & Wu, D. (2017). High precision DEM generation algorithm based on InSAR multi-look iteration. Remote Sensing, 9(7), 741
93. Goldstein, R. M., & Werner, C. L. (1998). Radar interferogram filtering for geophysical applications. Geophysical research letters, 25(21), 4035-4038.
94. Rocca, F., Ferretti, A., Monti-Guarnieri, A. V., Prati, C. M., & Massonnet, D. (2007). InSAR processing: a Mathematical Approach.
95. Olea, P., Monserrat, O., Sierralta, C., Barra, A., Bono, L., Fuentes, F., Zhiwei, Q. and Crippa, B., 2020, March. Mapping and monitoring ground instabilities with Sentinel-l data: the experience of Sernageomin. In 2020 IEEE Latin American GRSS & ISPRS Remote Sensing Conference (LAGIRS) (pp. 421-427). IEEE.
96. Raucoules, D., De Michele, M., Malet, J.P. and Ulrich, P., 2013. Time-variable 3D ground displacements from high-resolution synthetic aperture radar (SAR). Application to La Valette landslide (South French Alps). Remote Sensing of Environment, 139, pp.198-204.
97. Li, Y., & Zhang, Y. (2011, June). The research on deformation monitoring using Multi-Temporal InSAR. In 2011 International Conference on Remote Sensing, Environment and Transportation Engineering (pp. 3701-3704). IEEE.

98. Blanco, P., F. Pérez, Concha, A., J. Marturià, and V. Palà. 2012.. “Operational PS-DInSAR Deformation Monitoring Project at a Regional Scale in Catalonia (Spain).” IEEE International Geoscience and Remote Sensing Symposium, Australia, pp1178–1181.
99. Béjar-Pizarro, M., Herrera, G., Sarro, R., Mateos, R.M., Barra, A., González-Alonso, E. Fernández, A., Ligüerzana, S., Garcia-Cañada, L., Navarro, J., 2019. VEW validation report. Project U-Geohaz, Grant Agreement No. 783169.
100. Lanari, R., Bonano, M., Casu, F., Luca, C. D., Manunta, M., Manzo, M., ... & Zinno, I. (2020). Automatic Generation of Sentinel-1 Continental Scale DInSAR Deformation Time Series through an Extended P-SBAS Processing Pipeline in a Cloud Computing Environment. Remote Sensing, 12(18), 2961.
101. Costantini, M. (1998). A novel phase unwrapping method based on network programming. IEEE Transactions on geoscience and remote sensing, 36(3), 813-821.